

**PURDUE UNIVERSITY  
GRADUATE SCHOOL  
Thesis/Dissertation Acceptance**

This is to certify that the thesis/dissertation prepared

By \_\_\_\_\_

Entitled

For the degree of \_\_\_\_\_

Is approved by the final examining committee:

_____	_____
Chair	
_____	_____
_____	_____
_____	_____

To the best of my knowledge and as understood by the student in the *Research Integrity and Copyright Disclaimer (Graduate School Form 20)*, this thesis/dissertation adheres to the provisions of Purdue University's "Policy on Integrity in Research" and the use of copyrighted material.

Approved by Major Professor(s): \_\_\_\_\_  
\_\_\_\_\_

Approved by: \_\_\_\_\_  
Head of the Graduate Program Date

**PURDUE UNIVERSITY  
GRADUATE SCHOOL**

**Research Integrity and Copyright Disclaimer**

Title of Thesis/Dissertation:

For the degree of \_\_\_\_\_

I certify that in the preparation of this thesis, I have observed the provisions of *Purdue University Executive Memorandum No. C-22, September 6, 1991, Policy on Integrity in Research*.\*

Further, I certify that this work is free of plagiarism and all materials appearing in this thesis/dissertation have been properly quoted and attributed.

I certify that all copyrighted material incorporated into this thesis/dissertation is in compliance with the United States' copyright law and that I have received written permission from the copyright owners for my use of their work, which is beyond the scope of the law. I agree to indemnify and save harmless Purdue University from any and all claims that may be asserted or that may arise from any copyright violation.

\_\_\_\_\_  
Signature of Candidate

\_\_\_\_\_  
Date

\*Located at [http://www.purdue.edu/policies/pages/teach\\_res\\_outreach/c\\_22.html](http://www.purdue.edu/policies/pages/teach_res_outreach/c_22.html)

LAMINAR INSTABILITY AND TRANSITION ON THE X-51A

A Dissertation

Submitted to the Faculty

of

Purdue University

by

Matthew P. Borg

In Partial Fulfillment of the

Requirements for the Degree

of

Doctor of Philosophy

August 2009

Purdue University

West Lafayette, Indiana

## DISTRIBUTION STATEMENT

Approved for public release; distribution is unlimited. Case Number: 88ABW-  
2009-3283

## ACKNOWLEDGMENTS

This work was funded by the Air Force Office of Scientific Research and monitored by John D. Schmisser.

First and foremost, I thank my Lord and Savior, Jesus Christ. He daily bears my burdens and has given me strength to do the task He called me to do.

I am deeply indebted to my advisor, Steve Schneider, for advising me these last 6 years. His help, insight, and suggestions have been invaluable and have greatly impacted my development as an engineer. Thanks also to my advisory committee, Dave Kuntz, Kei Lau, Charles Merkle, and John Sullivan.

Many thanks to the machine shop at the ASL: Madeline Chadwell, Jim Younts, Robin Snodgrass, and Jerry Hahn. You have consistently been helpful and made high-quality parts to support my research.

I also profoundly thank my family for all their love and support throughout this process. I am so grateful for my wonderful wife, Nancy. Without her constant help, understanding, prayers, and encouragement, this effort would have been considerably more difficult. My parents, brothers, and sisters-in-law have also been a constant support. Even if you haven't understood everything I've done, thanks for taking the time and effort to try. I love you all.

Thanks also to my church family at Kossuth Street Baptist Church. The love, care, support, and biblical teaching have consistently spurred me on in faith and in my work. Thank you.

I'm also very grateful for my fellow grad students on Team Schneider. The discussions about course work and technical research matters has been of great help. You have also helped me have a lot of fun over the years with lunches, ultimate, 24, cook-outs, golfing, etc. Thanks to Shann Rufer, Craig Skoch, Erick Swanson, Tom

Juliano, Mikey Hannon, Katya Casper, Brad Wheaton, Dennis Berridge, Amanda Chou, Peter Gilbert, Laura Steen, and Chris Ward.

*Soli Deo Gloria!*

## TABLE OF CONTENTS

	Page
LIST OF TABLES . . . . .	vii
LIST OF FIGURES . . . . .	viii
NOMENCLATURE . . . . .	xii
ABSTRACT . . . . .	xiv
1 INTRODUCTION . . . . .	1
1.1 Hypersonic Boundary Layer Transition . . . . .	1
1.2 Instability Measurements . . . . .	5
1.3 Hypersonic Wind Tunnels . . . . .	7
2 FACILITY, MODEL, AND INSTRUMENTATION . . . . .	10
2.1 The BAM6QT . . . . .	10
2.2 Supersonic Jet . . . . .	15
2.3 X-51A Model . . . . .	15
3 INSTRUMENTATION . . . . .	20
3.1 Temperature Sensitive Paint . . . . .	20
3.1.1 History and Background . . . . .	20
3.1.2 Uses of TSP . . . . .	21
3.1.3 Photophysics of TSP . . . . .	21
3.1.4 Quantitative Data from TSP . . . . .	23
3.1.5 TSP Equipment . . . . .	27
3.2 Hot Wires . . . . .	27
3.3 PCB Pressure Sensors . . . . .	33
3.4 Oscilloscopes . . . . .	34
3.5 Freestream Reynolds Number Calculation . . . . .	34
4 WINDWARD MEASUREMENTS . . . . .	36
4.1 Motivation . . . . .	36
4.2 Effect of Tunnel Noise on Roughness-Induced Transition . . . . .	38
4.2.1 Smooth Insert . . . . .	42
4.2.2 Ramp Roughness Insert: 0.76-mm Maximum Height . . . . .	46
4.2.3 Ramp Roughness Insert: 0.38-mm Maximum Height . . . . .	58
4.2.4 Diamond Roughness Insert . . . . .	62
4.3 Streamwise Vortices . . . . .	69
5 LEEWARD MEASUREMENTS . . . . .	75

	Page
5.1 Temperature Sensitive Paint Measurements . . . . .	75
5.2 Hot-Wire Measurements . . . . .	79
5.2.1 Boundary Layer Profiles . . . . .	79
5.3 Natural Disturbances . . . . .	81
5.4 PCB Pressure Sensor Measurements . . . . .	83
5.4.1 Motivation . . . . .	83
5.4.2 Natural Disturbances . . . . .	84
5.5 Glow Perturber . . . . .	100
5.5.1 Glow Perturber Design . . . . .	101
5.5.2 Hot Wire Measurements with the Glow Perturber . . . . .	105
5.5.3 PCB Pressure Sensor Measurements with Glow Perturber . . . . .	112
5.5.4 Explanation of Glow Measurements from CFD . . . . .	114
5.6 Leading-Edge Roughness Effects . . . . .	123
5.6.1 Effect of Tunnel Noise on Leading-Edge Roughness . . . . .	124
6 CONCLUSIONS AND FUTURE WORK . . . . .	131
6.1 Conclusions . . . . .	131
6.2 Suggestions for Future Work . . . . .	132
LIST OF REFERENCES . . . . .	135
A RUN CONDITIONS . . . . .	141
B DRAWINGS . . . . .	145
VITA . . . . .	148



## LIST OF TABLES

Table	Page
4.1 Transition Reynolds numbers with smooth trip insert . . . . .	46
4.2 Boundary layer thickness . . . . .	54
4.3 Transition Reynolds numbers with $k_{max}=0.76$ mm (0.030 in.) ramp trips	58
4.4 Transition Reynolds numbers with $k_{max}=0.38$ mm (0.015 in.) ramp trips	61
4.5 Transition Reynolds numbers with $k_{max}=1.5$ mm (0.060 in.) diamond trips	68
5.1 Computed wall pressure and ratio of wall pressure to stagnation pressure for PCB pressure sensors . . . . .	85
5.2 Reynolds number for estimated transition onset for PCB and TSP data	94
5.3 Estimated time of arrival at each PCB pressure sensor for disturbances created at the glow perturber . . . . .	113
A.1 Freestream conditions for plots in Chapter 4 . . . . .	142
A.2 Freestream conditions for plots in Chapter 5: Part I . . . . .	143
A.3 Freestream conditions for plots in Chapter 5: Part II . . . . .	144

## LIST OF FIGURES

Figure	Page
2.1 The Boeing/AFOSR Mach-6 Quiet Tunnel . . . . .	11
2.2 Hot film voltage trace showing the tunnel becoming quiet and several turbulent bursts . . . . .	14
2.3 Full X-51A vehicle (from Ref. 45) . . . . .	16
2.4 Photographs of the X-51A model . . . . .	18
2.5 Side view of the X-51A model . . . . .	19
3.1 TSP calibration rig . . . . .	24
3.2 Typical TSP calibration . . . . .	25
3.3 Simplified CTA circuit . . . . .	29
3.4 Sample hot-wire calibration . . . . .	32
4.1 Trip inserts for model. Flow is top to bottom. . . . .	38
4.2 Centerline temperature for two runs at $Re=8.5\times 10^6/m$ ( $2.6\times 10^6/ft$ ), but different times during the runs due to different initial conditions . . . . .	40
4.3 Surface temperature (K) under quiet and noisy conditions with smooth trip insert . . . . .	42
4.4 Centerline temperature for smooth insert, quiet and noisy flow . . . . .	43
4.5 Hot-film spectra for smooth insert, quiet and noisy . . . . .	43
4.6 Surface temperature (K) distribution with $k_{max}=0.76$ mm ramp trips under quiet and noisy conditions . . . . .	47
4.7 Streamwise temperature for centerline and $y=-0.2$ cm ( $-0.08$ in.) for ramp trips, quiet and noisy flow . . . . .	48
4.8 Spanwise temperature at several streamwise locations for quiet flow . . . . .	48
4.9 Hot-film spectra for quiet and noisy flow, $k_{max}=0.76$ mm ramp trips . . . . .	49
4.10 Surface temperature for $Re=5.9\times 10^6/m$ ( $1.8\times 10^6/ft$ ), quiet flow, ramp trips . . . . .	51

Figure	Page
4.11 Centerline temperature for $Re=5.9 \times 10^6/m$ ( $1.8 \times 10^6/ft$ ), quiet flow, ramp trips . . . . .	51
4.12 Boundary layer profiles . . . . .	53
4.13 Hot wire spectra for ramp roughness . . . . .	55
4.14 Hot wire spectra for signals with 0 and 1 turbulent burst . . . . .	56
4.15 Surface temperature (K) distribution under quiet and noisy conditions, $k_{max}=0.38$ mm (0.015 in.) . . . . .	59
4.16 Streamwise temperature (K) under quiet and noisy conditions, $k_{max}=0.38$ mm (0.015 in.) . . . . .	60
4.17 Surface temperature (K) with diamond trips under quiet and noisy conditions . . . . .	63
4.18 Streamwise temperature for centerline and $y=-0.4$ cm (-0.16 in.) for diamond trips, quiet and noisy flow, $Re=6.7$ and $7.4 \times 10^6/m$ (2.1 and $2.3 \times 10^6/ft$ ) . . . . .	64
4.19 Spanwise temperature at various streamwise locations, diamond trips, quiet flow . . . . .	64
4.20 Spectra for noisy and quiet flow with diamond trips . . . . .	65
4.21 Surface temperature for $Re=5.8 \times 10^6/m$ ( $1.8 \times 10^6/ft$ ), quiet flow, diamond trips . . . . .	66
4.22 Centerline temperature for $Re=5.8 \times 10^6/m$ ( $1.8 \times 10^6/ft$ ), quiet flow, diamond trips . . . . .	66
4.23 Hot wire spectra for diamond roughness . . . . .	67
4.24 Spanwise temperature showing streamwise vortices for 3 trip configurations	70
4.25 Spanwise temperature showing streamwise vortices for $k_{max}=0.38$ mm ramp roughness at various Reynolds numbers . . . . .	71
4.26 Spanwise RMS temperature as a function of streamwise distance for ramp and diamond trips . . . . .	73
5.1 Reynolds number sweep of surface temperature distribution with conventional freestream noise . . . . .	76
5.2 Centerline temperatures for conventional and low freestream noise levels	77
5.3 Boundary layer profile. 620.5 kPa (90 psia), noisy flow . . . . .	80

Figure	Page
5.4 Spectra of CTA-bridge voltage at $x=16.8$ , $21.6$ , and $33.0$ cm (6.6, 8.5, and 13.0 in.), noisy . . . . .	82
5.5 Raw pre-run PCB and high-pass filtered signal . . . . .	86
5.6 Centerline temperature for noisy flow . . . . .	87
5.7 PCB spectra for $x=19.3$ cm . . . . .	88
5.8 PCB spectra for $x=25.7$ cm . . . . .	91
5.9 PCB spectra for $x=28.8$ cm . . . . .	92
5.10 PCB spectra for $x=31.9$ cm . . . . .	93
5.11 RMS disturbance amplitudes between 75 and 125 kHz for constant $x$ .	94
5.12 RMS disturbance amplitudes between 270 and 370 kHz for constant $x$ .	96
5.13 Disturbance amplitudes and spectra for quiet, $Re=10.5 \times 10^6/m$ , and noisy, $Re=11.5 \times 10^6/m$ , flow . . . . .	98
5.14 Glow perturber as installed . . . . .	102
5.15 Glow perturber signal . . . . .	104
5.16 Glow-discharge circuit (taken from Ref. [79]) . . . . .	105
5.17 Sample voltage traces of electrode gap and CTA bridge voltage . . . . .	107
5.18 Ensemble-averaged CTA bridge voltage traces and power spectra with glow perturber running at 30 kHz, noisy flow, $x=16.8$ cm (6.6 in.) . . .	109
5.19 Ensemble-averaged CTA bridge voltage traces and power spectra with glow perturber running at 30 kHz, noisy flow, $x=21.6$ cm (8.5 in.) . . .	111
5.20 Ensemble-averaged voltage traces for $x=16.8$ and $21.6$ cm (6.6 and 8.5 in.)	112
5.21 Averaged FFTs of PCB signals with and without glow perturber for various signal windows . . . . .	115
5.22 Averaged FFTs of PCB signals with and without glow perturber for various signal windows . . . . .	116
5.23 Computations for N-factors and most unstable frequencies (from [75]) .	118
5.24 Computed stability diagram for X-51A (from [75]) . . . . .	119
5.25 N factors vs. $x$ for frequencies between 140 and 180 kHz (from [75]) . .	120
5.26 Amplification rate for 30 kHz first-mode instability (from [75]) . . . . .	121
5.27 Experimental and computed boundary-layer profile . . . . .	122

Figure	Page
5.28 Surface temperature distribution and streamwise centerline temperatures under noisy conditions for $k=0.00, 0.05,$ and $0.10$ mm (0.000, 0.002, and 0.004 in.) . . . . .	127
5.29 Part 1: Surface temperature (K) distribution under quiet and noisy conditions with leading-edge roughness . . . . .	128
5.30 Part 2: Surface temperature (K) distribution under quiet and noisy conditions with leading-edge roughness . . . . .	129
5.31 Spanwise temperature distributions at $x=15.0$ cm, quiet and noisy flow for leading edge roughness . . . . .	130
B.1 Glow perturber design drawing . . . . .	146
B.2 Modifications to aluminum afterbody to allow installation of PCB sensors and glow perturber . . . . .	147

## NOMENCLATURE

$A$	Disturbance amplitude
$A_0$	Initial disturbance amplitude
$I$	Intensity
$I_{ref}$	Reference intensity
$M$	Freestream Mach number
$M_e$	Edge Mach number
$N$	N factor
$P$	Static pressure
$P_0$	Stagnation pressure
$P_{0,i}$	Initial stagnation pressure
$P_{RMS}$	Wall RMS static pressure
$P_{Wall}$	Mean wall static pressure
$R$	Gas constant for air
$Re$	Freestream unit Reynolds number
$R_{ref}$	Wire resistance at reference temperature
$Re_t$	Transition Reynolds number based on freestream conditions
$R_w$	Wire resistance
$Re_\theta$	Momentum thickness Reynolds number based on edge conditions
$T$	Static temperature
$T_0$	Stagnation temperature
$T_{0,i}$	Initial stagnation temperature
$T_e$	Wire recovery temperature
$T_{ref}$	Reference temperature
$T_w$	Wire temperature
$U$	Freestream velocity

$a$	Speed of sound
$d$	Electrode gap spacing
$e$	CTA bridge voltage
$k$	Roughness height
$t_a$	Time of arrival
$t_b$	Time glow is produced
$t_d$	Glow delay
$t_p$	Time between start of glow pulses
$t_w$	Wave period
$x$	Streamwise coordinate
$x_0$	Streamwise coordinate of initial instability onset
$x_t$	Streamwise transition location
$y$	Spanwise coordinate
$z$	Distance from model surface
$z'$	Leading edge arclength
$\alpha_i$	Disturbance amplification
$\alpha$	Temperature coefficient
$\gamma$	Ratio of specific heats for air
$\delta$	Boundary layer thickness
$\lambda$	Instability wavelength
$\nu$	Frequency of excitation light
$\nu_f$	Frequency of emitted radiation (fluorescence)
$\nu_p$	Frequency of emitted radiation (phosphorescence)
$\rho$	Static density
$\tau$	Hot wire overheat ratio
$\omega_f$	Disturbance frequency
$\omega_p$	Frequency of wave pulses

## ABSTRACT

Borg, Matthew P. Ph.D., Purdue University, August 2009. Laminar Instability and Transition On the X-51A. Major Professor: Steven P. Schneider.

A 20% scale model of the X-51A was tested in the Boeing/AFOSR Mach-6 Quiet tunnel. Freestream noise was found to have a major impact on transition on the windward and leeward vehicle surfaces. The effect of noise on transition was observed with a smooth wall and for roughness-induced transition on both surfaces.

Temperature sensitive paint (TSP) and hot wires were used to characterize transition onset on the windward surface. The transition Reynolds number ( $Re_t$ ) increased by a factor of at least 2.2 for a smooth wall, 2.4 with ramp roughnesses, and 1.7 for diamond roughnesses when the freestream noise was decreased.

Pressure sensors and TSP determined the presence of the second-mode instability on the lee side. Disturbances near 100 kHz were observed to grow in amplitude with both downstream distance and increasing freestream Reynolds number. At one condition, transition on the center line occurred when the the disturbance amplitude reached about 3%. Reducing noise levels increased  $Re_t$  by a factor of at least 2. Transition was not observed on the lee side at the maximum Reynolds number giving quiet flow. Computations predicted that the most unstable instability is the second-mode near 100 kHz, in good agreement with the experimental data.



# 1. INTRODUCTION

## 1.1 Hypersonic Boundary Layer Transition

An understanding of the stability and transition of boundary layers on hypersonic vehicles is often essential for optimal vehicle performance. The state of the boundary layer has first-order effects on heating, viscous drag, and control surface effectiveness. In order to optimize performance and ensure the survivability of such vehicles, accurate transition prediction techniques must be developed.

In low noise environments, the breakdown of a laminar boundary layer to turbulence generally happens in successive stages. Initially, disturbances that originate in the freestream or on the body couple with the laminar boundary layer via a “receptivity” process. Such disturbances excite instabilities in the laminar boundary layer. These initially small-amplitude instabilities propagate downstream through the boundary layer where they experience exponential growth or decay via predominantly linear processes. Once the instability waves grow to a sufficiently large amplitude, they enter a regime of nonlinear growth that can excite secondary instabilities. The growth and interaction between these instabilities leads to turbulent spots and eventually full breakdown to turbulence.

A number of imperfectly understood instability mechanisms can lead to transition of a hypersonic boundary layer. A concave wall can destabilize the boundary layer via the centrifugal Görtler instability. For three-dimensional geometries, crossflow can give rise to stationary or traveling co-rotating vortices due to inflections in the spanwise velocity profile which then break down to turbulence. For supersonic and hypersonic edge Mach numbers, the first and higher-mode instabilities may dominate the transition process.

First-mode waves are analogous to the incompressible and inviscid Tollmien-Schlichting (TS) instability waves found in low-speed flows. The first mode instability is a vorticity disturbance [1]. First mode waves always amplify most at oblique wave angles [2]. For higher edge Mach numbers, acoustical instability modes dominate [2, 3]. Mack [2] demonstrated that for edge Mach numbers  $M_e$  above one, a region of the boundary layer becomes supersonic relative to the phase velocity. Under these conditions, multiple solutions to the inviscid stability equations exist. These additional solutions have been termed the “Mack” modes, the first of which is the second mode. It is the most unstable of the Mack modes and is most unstable at normal, non-oblique wave angles. Second mode waves behave like trapped acoustic waves in the boundary layer and are characterized by wavelengths around twice the boundary layer thickness [3].

The linear growth of instabilities is fairly well understood. However, linear processes alone do not describe the complexities of instability growth and breakdown. Nonlinear wave interactions have also been shown to have a significant impact on the transition process. The physics of nonlinear growth and mode interactions are complex and not understood, particularly at high speed. Herbert [4] presents a review of low-speed nonlinear aspects of transition. His work focused mainly on the TS, Görtler, and crossflow instabilities. He also presents a brief theoretical overview of nonlinear breakdown of the primary instability modes. The role of nonlinear subharmonic secondary instabilities was investigated.

There is not a great deal of published work in the open literature addressing the role of secondary nonlinear instabilities in high-speed compressible flows. Stetson [5] comments on the spectral dispersion he observed prior to transition on a sharp,  $7^\circ$  cone at Mach 8. This spectral broadening is not predicted by linear stability theory. He attributes this and the appearance of suspected harmonics of the fundamental second-mode frequency to nonlinear effects and not independently excited modes. Shipliyuk et al. [6] examined natural and artificially-excited disturbances in the boundary layer of a  $7^\circ$  sharp cone at Mach 5.95. For frequency interactions to be nonlinear and not due to

an independently-excited mode, phase-locking between the two interacting frequencies is necessary. Analyzing hot-wire data using the bicoherence spectrum, they verified that a subharmonic resonance was attributable to nonlinear wave development. After the onset of nonlinear subharmonic waves, higher-harmonic wave generation was also noted. Additionally, nonlinear wave interaction was seen among the fundamental second mode, subharmonic, and harmonic frequencies. A weak nonlinear interaction between the first and second modes was also observed. These interactions led to a broadening of the spectra which preceded transition.

Empirical transition prediction methods, such as  $Re_\theta/M_e$ , are frequently employed in the design of hypersonic vehicles. This correlation assumes that transition occurs at some fixed value of  $Re_\theta/M_e$  where  $Re_\theta$  is the momentum-thickness Reynolds number at transition. Such correlations can be useful for some simple geometries and trajectories. They cannot, however, provide an accurate and reliable method for prediction of transition for arbitrary vehicle designs. Reshotko [7] comments that  $Re_\theta/M_e$  fails in that it does not represent physical processes by neglecting the important effects of pressure gradient, surface temperature, and roughness. This example underscores the fundamental lack of understanding regarding the physics of boundary-layer transition. Yet, vehicle designers appeal to these methods as their only recourse given the lack of affordable and reliable physics-based transition-prediction methods.

A useful, semi-empirical method for predicting transition is the  $e^N$  method. The basis for the method is the following relation:

$$N = \int_{x_0}^x \alpha_i dx = \ln \frac{A}{A_0}$$

where  $N$  is the integrated growth rate,  $\alpha_i$ , of a disturbance at some frequency,  $x_0$  is the location where the frequency of interest first becomes unstable, and  $x$  is the streamwise station of interest. The  $N$  factor is likewise equal to the ratio of the amplitude of a disturbance at some frequency,  $A$ , to the amplitude of that disturbance when it first becomes unstable and begins to grow in the boundary layer,  $A_0$ .

The  $e^N$  method is gaining popularity as the physical mechanisms leading to transition and their interactions are becoming more understood. Computations are also becoming more feasible, which makes  $e^N$  type calculations more accessible for experiments and vehicle design. For example, the stability and transition analysis for hypersonic Boundary Layers (STABL) software suite solves the linearized parabolized stability equations [8]. The solution to the eigenvalue problem describes the growth and decay of perturbation waves in the boundary layer. However, STABL does not account for wave growth once the disturbances become large enough that nonlinear effects become non-negligible. It cannot, therefore, predict transition. Instead, this theoretical approach can be coupled with empirical measurements in methods such as the  $e^N$  method. The  $N$  factors can be calculated and transition assumed for some experimentally-determined value of  $N$ . From empirical data, transition for a variety of geometries and freestream conditions has been found to be between 7 and 12 in low-noise facilities and flight [9–11]. For conventional-noise facilities, this value decreases to 4-5 [12–15]. When the computed  $N$ -factor reaches these values, transition is assumed to occur.

As interest in vehicles that spend significant time at hypersonic velocities increases, so too does an interest in hypersonic boundary-layer transition. It is well established that surface heating rates are significantly higher for a turbulent boundary layer than for a laminar one. For a given vehicle, if the transition Reynolds number ( $Re_t$ ) is underpredicted, superfluous thermal protection system (TPS) material may be used resulting in excess inert mass and decreased payload capability. Conversely, if  $Re_t$  is overpredicted, the TPS may not adequately handle the increased surface heat flux due to early transition. Additionally, due to increased shear stress from the turbulent boundary layer, the total vehicle drag would be larger than expected with an overpredicted  $Re_t$ . These unexpected changes could result in reduced performance or even the loss of the vehicle.

It is evident that better physics-based transition-prediction methods must be developed to optimize the design of hypersonic vehicles. However, due to the difficulty

and high cost, a fundamental understanding of transition physics is not likely to result from flight tests. A lower cost option is ground testing. Wind tunnel tests do not provide a full duplication of flight conditions, however. Limitations inherent in ground-test facilities make it difficult to uncouple facility effects from actual vehicle aerodynamics. Efforts must be made to simulate the flight environment as closely as possible in ground-test facilities in addition to developing accurate computational fluid dynamics (CFD) flow models. Such developments should inform each other and serve to enhance understanding of the physics of boundary-layer transition.

## 1.2 Instability Measurements

A number of experimental techniques have been successfully employed in the study of the instabilities and transition of high-speed boundary layers. Hot-wire anemometry has proven to be a very useful tool for measuring such instabilities. Refs. 16–19 all report early hot-wire measurements of instability waves at high speeds for various freestream conditions and models. Stetson [1] used hot-wire anemometry to measure the second mode instability at Mach 8 for cones and a cylinder. More recently, Rufer et al. measured second-mode instabilities on a cone at Mach 6 [20, 21]. Ref. 21 reports that the frequencies with the highest mass-flow fluctuation amplitudes were in reasonable agreement with computations. The computations were performed using the STABL code.

A new technique that has proven to be successful in the measurement of instability waves is the use of surface-mounted high frequency-response PCB pressure transducers. These fast sensors are able to measure pressure fluctuations due to second-mode boundary-layer instability waves. Fujii [22] pioneered the effort to use PCB Piezotronics fast pressure sensors to measure second-mode wave growth. He used three sensors at different streamwise stations on a  $5^\circ$  half-angle cone at Mach 7. He examined the effect of different wall waviness and tunnel stagnation conditions on second-mode wave growth. The sensors were able to show clear spatial growth of the waves. Es-

torf et al. [23] successfully employed this technique to measure amplification rates under both conventional and quiet freestream noise levels on a  $7^\circ$  half-angle sharp cone. Ref. 24 reports possible measurements of the second mode instability on a  $7^\circ$  half-angle cone at Mach 6.3-7.7. Ref. 25 discusses the use of several PCB sensors on a  $7^\circ$  half-angle cone at Mach 5, 6, and 8. Second-mode waves were detected with conventional noise levels at all three Mach numbers and also with low, flight-like noise levels at Mach 6. They were observed to spatially amplify and break down. For constant location and increasing Reynolds number, the waves also grew in amplitude and broke down.

Ref. 26 reports computations of a hypersonic boundary layer. Using linear stability theory, eigenfunctions for mass flux, pressure, and temperature fluctuations were calculated for a flow of interest. It was found that for the second mode instability, a strong peak in pressure fluctuations occurs at the wall. It should also be noted that this is in stark contrast to the first mode instability, which has much smaller pressure fluctuations that are nearly constant across the boundary layer. Thus, these data substantiate the effectiveness of the PCB sensors to detect the second mode instability when they are mounted flush with the model wall. It is less likely that they would detect the first mode unless the waves were of very large amplitude.

Most of the high-speed measurements mentioned above have been primarily concerned with naturally occurring instabilities. Some effort has been made to introduce artificial, controlled disturbances into the boundary layer to examine the impact on stability. Studying the stability of boundary layers with and without controlled disturbances can give insight into the mechanisms leading to transition and also the receptivity phenomena of particular flows. Refs. 16 and 17 report using an acoustic “siren” to excite waves of selected frequencies in the boundary layer. A more recent technique for introducing controlled disturbances into a laminar, high-speed boundary layer uses what is known as a glow discharge perturber. A glow perturber works by applying a large electric potential across the gap between two electrodes. Given the proper flow conditions, the fluid in the gap will break down in a glow discharge.

A normal glow discharge is characterized by relatively low electrode voltages and current. A normal glow exhibits very little increase in electrode voltage for up to an order of magnitude increase in current [27]. Ladoon et al. [28], [29] used a pair of electrodes separated by a dielectric on the surface of a cone at Mach 4 to successfully perturb the boundary layer. Maslov et al. [30] report the successful use of an electrical glow discharger perturber in a cavity to introduce disturbances into the boundary layer of a cone at Mach 5.9. Refs. 28 and 30 discuss the use of hot-wire anemometry to measure the excited instability waves.

### 1.3 Hypersonic Wind Tunnels

Conventional supersonic and hypersonic wind tunnels are characterized by high levels of freestream noise. This noise takes the form of eddy Mach wave acoustic energy radiated from the turbulent wall boundary layer. The noise level of a tunnel is often reported as the RMS pitot pressure fluctuations non-dimensionalized by the mean pitot pressure. This is typically on the order of 0.5-1.0%. Ref. 31 summarizes noise measurements from many supersonic and hypersonic wind tunnels for Mach numbers ranging from 2 to 24. Pressure fluctuations were measured using hot wires in the freestream and acoustical transducers mounted flush with the surface of a sharp cone or a flat plate. He reports pressure fluctuations ranging from about 0.5% to 11%. However, these measurements do not account for differences in the instrumentation nor how freestream noise couples with the boundary layer of the model in which the acoustical transducers were located. Flight noise levels, in contrast, can be an order of magnitude lower than those experienced in most hypersonic ground facilities [32, 33].

Noise levels of this magnitude have been shown to decrease the transition Reynolds number by up to an order of magnitude and even change or bypass the normal parametric trends in transition [10, 34]. Ref. 35 reports the effect of freestream noise on roughness-induced transition with very large boundary-layer trips for a scramjet inlet. Borg et al. [36] demonstrated the significant effect of tunnel noise on transition due

to boundary-layer-sized trips. Ref. 37 describes the large effect of freestream noise on natural and roughness-induced transition for a cone at Mach 6. Ref. 32 presents an extensive review of the effect of tunnel noise on transition. It is evident from the larger body of literature that tunnel noise has a non-negligible effect on transition and should not be ignored for instances when instability and transition are important.

Often, the spectra of the freestream disturbances in conventional tunnels show significant spectral contributions in the lower frequency bands. If those frequencies are near those of naturally occurring instabilities, Stetson [1] suggests that they may prematurely excite instability-wave growth. It is plausible that, via the receptivity process, such disturbances are introduced into the boundary layer at a much larger initial amplitude than would be experienced in flight or in a low-disturbance facility. With the exponential growth of disturbances, the larger initial disturbance amplitude could lead to earlier breakdown to turbulence. Thus, the high levels of noise in conventional tunnels renders transition data from those facilities unreliable predictors for transition on flight vehicles [38].

The development of quiet hypersonic wind tunnels that approach flight noise levels is essential in order to mitigate the problem of noise contamination endemic to conventional tunnels. Quiet facilities typically have noise levels less than 0.1%. Such exceptionally low noise levels are achieved by taking great care to ensure that the nozzle-wall boundary layer remains laminar to at least the acoustic origin for disturbances impinging on a model. Development and utilization of quiet facilities should help to divorce instability and transition measurements from the particular characteristics of a given wind tunnel and allow a more complete understanding of the underlying flow physics.

Measurements in quiet hypersonic facilities are good candidates to compare to state-of-the-art stability and transition-prediction techniques such as  $e^N$  and other physics-based methods. Quiet-tunnel experiments should be compared to computational results to validate and help refine the models. For example, experimental data from quiet facilities could help determine the extent of nonlinear effects. This would



assist in determining if linear stability solvers are sufficient for instability growth and transition prediction.

## 2. FACILITY, MODEL, AND INSTRUMENTATION

### 2.1 The BAM6QT

In order to study boundary layer transition while removing the high levels of freestream noise in most conventional hypersonic wind tunnels, a quiet hypersonic facility was constructed at Purdue University. The tunnel is designed to operate at Mach 6 and have laminar boundary layers up to a throat unit Reynolds number of  $10^8/\text{m}$  ( $31 \times 10^6/\text{ft}$ ), which corresponds to a stagnation pressure of approximately 1.03 MPa (150 psia) [39]. Quiet flow requires freestream RMS pressure fluctuations of less than about 0.1%.

The Purdue facility, shown in Figure 2.1, was designed as a Ludwieg tube. A Ludwieg tube consists of a long driver tube followed by a converging-diverging nozzle, second throat, diffuser, and large vacuum chamber. In the case of the Boeing/AFOSR Mach-6 Quiet-Tunnel (BAM6QT), the driver tube is 37.3 m (122.5 ft) long with an inner diameter of 44.5 cm (17.5 in.). It consists of 6 sections of 46 cm (18-in.) schedule-10, type 304 stainless steel pipe, with 6.35 mm (0.25 in.) thick walls. It is ASME U-stamped and certified for operations up to 2.07 MPa gauge (300 psig) at 473 K (853°R) [40]. A sting mount is positioned in the diffuser section to allow models to be placed in the tunnel.

Additionally, in order to avoid nitrogen liquefaction in the nozzle at Mach 6, the driver tube must be uniformly heated to about 160°C (320°F). To aid in this uniform heating, the driver tube is insulated with 7.6 cm (3 in.) fiberglass pipe insulation. The tube is heated by generating a 6 V electric potential drop across its length. This draws approximately 2000 amps through the driver tube, which is heated via Ohm's law. A thermocouple near the downstream end of the driver tube is typically used to control the temperature, although which thermocouple is the controlling thermocouple can

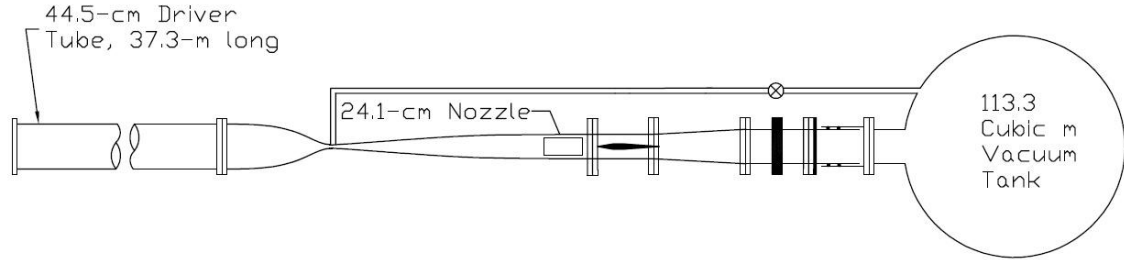


Figure 2.1: The Boeing/AFOSR Mach-6 Quiet Tunnel

be changed. Four Electronics Measurement Incorporated TCR10T750 power supplies provide the necessary current for heating. These power supplies each have a maximum output of 750 amps at 10 volts and are regulated by an Omega CN9000A controller. Starting from room temperature, it takes approximately 6 hours for the driver tube to reach the set temperature and another 18 hours to equilibrate [41].

In order to keep the contraction from being a large heat sink that reduces the temperature of the downstream end of the driver tube, three band heaters are used to heat the contraction. The two upstream heaters are Tempco 1500W, 240V heaters and the smaller downstream heater is a Tempco 3000W, 240V heater. Each heater is controlled by an Athena Controls, Inc., AIM15 controller. Surface thermocouples are affixed to the contraction by hose clamps and are used by the controllers to determine when each heater needs power in order to keep the temperature at the set point.

A HEAT 30kW circulation heater, set to  $165^{\circ}\text{C}$  ( $329^{\circ}\text{F}$ ), was used to heat the incoming air. The circulation heater was controlled by a Watlow 988A-10KD-AAGR heater controller. By examining the readout of a K-type thermocouple located near the upstream end of the driver tube, it has been found that the actual temperature of the heater equilibrates to about  $5^{\circ}\text{C}$  lower than its set point.

Over the length of the driver tube, a significant boundary layer develops. In Ludwig tubes, this boundary layer on the driver-tube wall is often turbulent. Although passing through the contraction can relaminarize the boundary layer, it is

nevertheless to be removed from the flow just upstream of the throat in order to remove any residual disturbances and to begin with a fresh laminar wall boundary layer with a known starting location [40]. It is removed by removing it through a small axisymmetric bleed slot just upstream of the nozzle throat. The flow through the slot is accelerated to sonic conditions in order to prevent disturbances from feeding upstream and polluting the primary nozzle flow and/or causing the location of the bleed-lip stagnation point to oscillate.

The flow through the bleed slot is exhausted directly into the 113 m<sup>3</sup> (4000 ft<sup>3</sup>) vacuum tank. The bleed system requires a fast-opening valve to open. The valve is triggered by the oscilloscope and uses a compressed air supply to open. The bleed system takes about 0.1 s to start [42].

In December 2007, in the middle of the current work, a new sting support section and diffuser replaced the original tunnel hardware. It was hoped that the larger inner diameter would allow larger and more blunt models to correctly start in the tunnel. Unfortunately, this was not the effect. Instead, under quiet flow conditions, interactions between the shocks from the experimental models and the nozzle wall boundary layer often result in a large, unsteady separation that largely distorts the mean flow far upstream of the shock impingement point, yielding no useful data. This effect had deleterious consequences for the current work.

A series of diffuser inserts that modify the internal geometry are being designed and tested. It is hoped that these modifications of the new diffuser section will improve starting and mitigate separation of the nozzle wall boundary layer. Details of this work can be found in Ref. 43.

The nozzle of the BAM6QT was designed and fabricated to very tight tolerances. In an effort to keep wall roughness from being the dominant transition mechanism, it was necessary to ensure that the RMS wall roughness was as small as feasible. Although measurements have not been obtained in the throat, it has been estimated that the RMS in the throat is on the order of 13-25 nm (0.5-1.0  $\mu$ in.). In order to achieve such tight tolerances, it was necessary to make the first 4 sections of the nozzle

from one solid piece of electroformed nickel. The remaining 4 sections were machined and polished to low peak roughness levels, low contour errors, and low waviness [44].

Although care is taken to maintain a laminar boundary layer on the nozzle wall for as long as possible and to high Reynolds number, the boundary layer does not remain laminar for all tunnel conditions. For sufficiently high pressure, the boundary layer is turbulent, even when the contraction boundary layer is removed upstream of the nozzle throat. When the tunnel is operated below the maximum initial stagnation pressure giving low freestream noise levels, the maximum “quiet pressure,” the nozzle wall boundary layer typically does not remain completely laminar. Rather, bursts of turbulence convect downstream in an unsteady and unrepeatable manner, causing brief bursts of acoustic noise in the freestream. Usually, these bursts are observed on the instrumentation for only 1-2 ms per burst. There are almost always more turbulent bursts when the tunnel is operated near the maximum quiet pressure.

Figure 2.2 shows the raw voltage output of a constant temperature anemometer running a hot-film mounted on the nozzle wall. The tunnel startup lasts from approximately  $t = 0.0$  to  $t = 0.15$  s. For  $0.15 < t < 2.2$  s, the voltage trace is typical for a turbulent nozzle-wall boundary layer. For this time period, the tunnel has conventional or “noisy” freestream noise levels. At about  $t = 2.2$  s, the mean voltage drops and the RMS voltage decreases substantially. This is the point at which the stagnation pressure has reached the maximum quiet pressure. The nozzle-wall boundary layer here has become laminar, reducing freestream noise levels. A laminar boundary layer is maintained until about  $t = 6.5$  s when the tunnel shuts down. For  $2.2 < t < 6.5$  s, a number of spikes in the voltage trace are observed. These voltage spikes are due to the short-duration turbulent spots moving past the sensor.

The procedure for operating the tunnel is generally the same from run to run. The circulation heater is turned on about 30 seconds prior to pressurizing the tunnel. A solenoid on the upstream end of the driver tube is then opened via a remote switch. This allows air to be pumped into the driver tube. This is accomplished by applying a voltage to a pressure regulator. An incremental increase in this voltage gradually

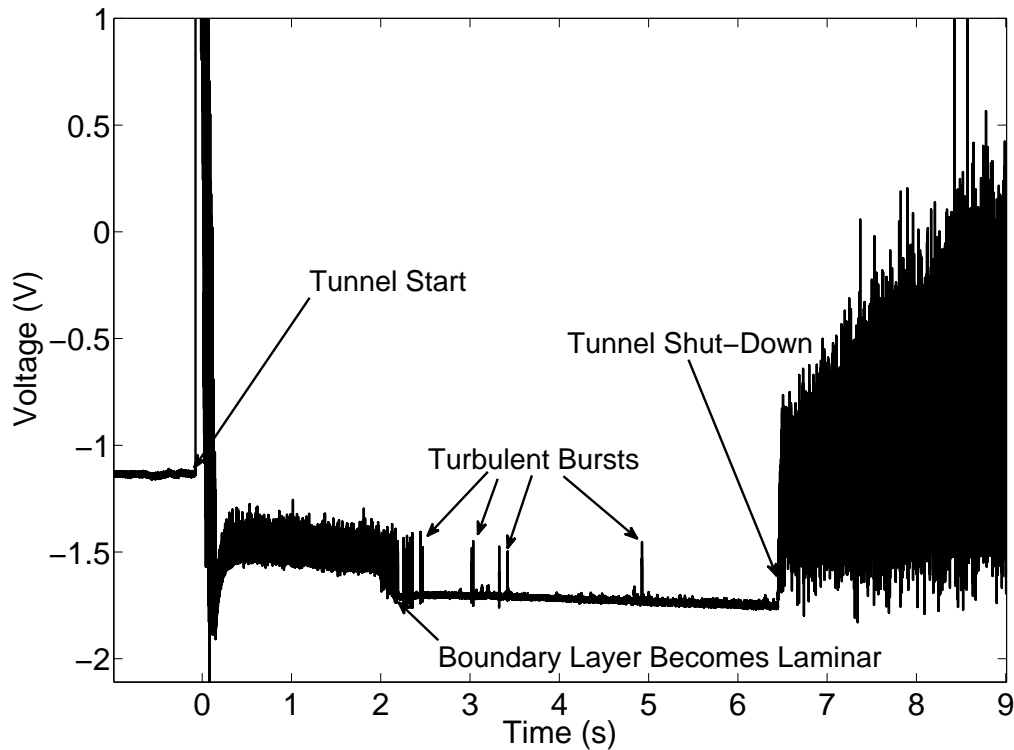


Figure 2.2: Hot film voltage trace showing the tunnel becoming quiet and several turbulent bursts

pressurizes the tunnel to the desired initial stagnation pressure. A Panametrics Moisture Target Series-5 dewpoint meter is used to periodically check the dewpoint of the air in the tunnel. This was usually found to be around  $-20^{\circ}\text{C}$  ( $-4^{\circ}\text{F}$ ), although this value was somewhat higher during the humid summer months.

A pair of burst diaphragms is used to initiate a tunnel run. The gap between the two diaphragms is generally kept at half of the upstream pressure while the tunnel conditions equilibrate. In order to start a run, the gap is exposed to a vacuum. When the gap pressure drops far enough, the upstream diaphragm bursts, followed by the downstream diaphragm.

At this point, a shock wave travels downstream into the vacuum tank while an expansion wave travels upstream. The expansion wave traverses the length of the driver tube, in approximately 0.1 s, reflecting from the upstream end and then the contraction. Although the nominal tunnel run ends when the expansion wave returns to the contraction, the tunnel has been demonstrated to remain quiet through many expansion-wave reflection cycles. Throughout these cycles, the pressure in the driver tube drops quasi-statically. Given a sufficiently low back pressure, hypersonic flow continues for approximately 6 seconds.

## **2.2 Supersonic Jet**

The Supersonic Jet (SSJ) facility was used to calibrate the hot wires used in the BAM6QT. The SSJ consists of a Chromalax heater, plenum, 2.5-cm- (1.0 in.) diameter nozzle, exhaust chamber, diffuser, and vacuum tank. The nozzle was designed for Mach 4, but has been shown to operate at about  $M=3.9$ . Both the stagnation temperature and pressure can be independently varied. The static pressure in the plenum, equivalent to the stagnation pressure for the flow, is measured by an Ashcroft test gauge with a range of 0-689 kPa gauge (0-100 psig) and an accuracy of 0.25%.

## **2.3 X-51A Model**

The Boeing Company is currently working on a scramjet-powered vehicle known as the X-51A. This vehicle will be the first flight-weight, hydrocarbon-fueled scramjet. Boundary-layer transition on all of the vehicle's surfaces is important. If the boundary layer entering the scramjet is laminar, it is likely that shock/boundary layer interactions in the isolator will lead to separation and unstart of the engine. This could lead to a loss of the vehicle. It is desired that all other vehicle surfaces maintain laminar boundary layers for as long as possible, with the possible exception of control surfaces. This will reduce viscous drag and heating, improving vehicle performance by providing more net thrust and reducing the necessary thermal protection.

In order to support analysis of boundary layer transition on the X-51A, experiments on a 20% scale model were designed and conducted. The model includes the forebody up to the engine inlet cowl.

The experiments reported here were all for an inviscid Mach number of 6.0 with an initial stagnation temperature of  $T_0=433$  K (780°R) at 4.0° angle of attack. A sketch of the full flight vehicle is shown in Figure 2.3. The portion that corresponds to the Purdue model is circled.

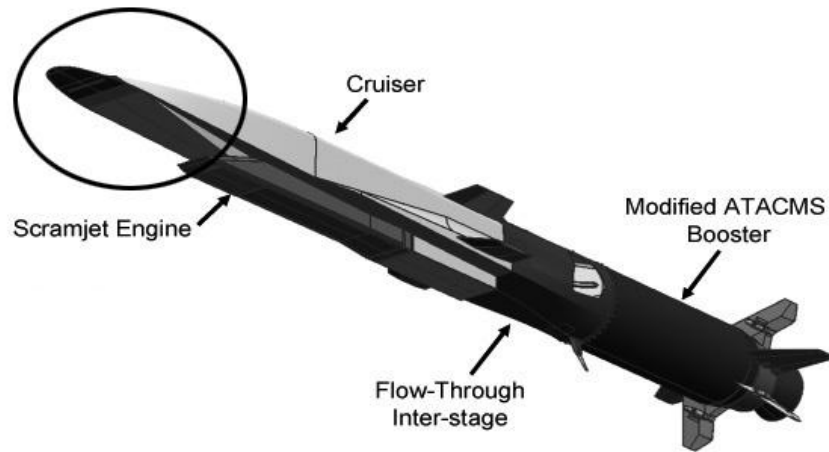


Figure 2.3: Full X-51A vehicle (from Ref. 45)

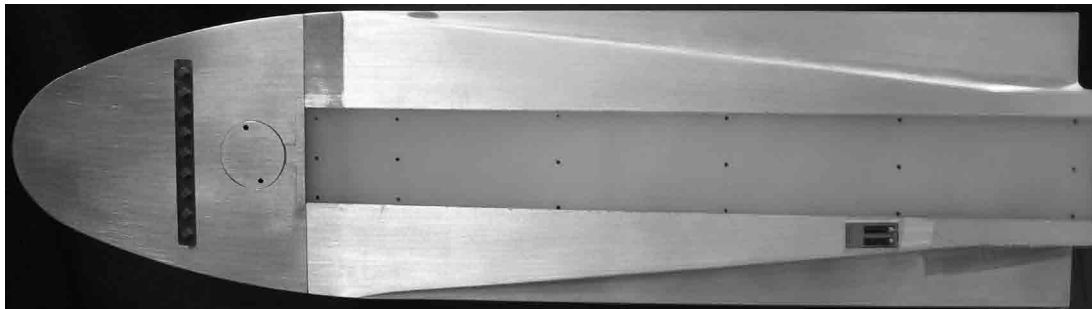
The model consists of a stainless-steel nose section and one of two afterbodies. One is made from solid aluminum. The other has an aluminum strongback but also includes nylon 6/6 inserts on both the windward and leeward sides. The nylon inserts were included to act as a thermal insulator layer for temperature sensitive paint (TSP). The assembled model is 34.42 cm (13.55 in.) long. The windward nylon insert is approximately 23.9 cm (9.4 in.) long and 3.0 cm (1.2 in.) wide. The insert is comprised of a 1.02 cm (0.4-in.)-long flat surface followed by a compression corner. The remainder of the insert maintains a constant angle to the flow and a constant width. The leeward nylon insert is about 6.1 cm (2.4 in.) wide and 17.0 cm (6.7 in.) long. The insert is nearly flat in the streamwise direction, but has significant spanwise



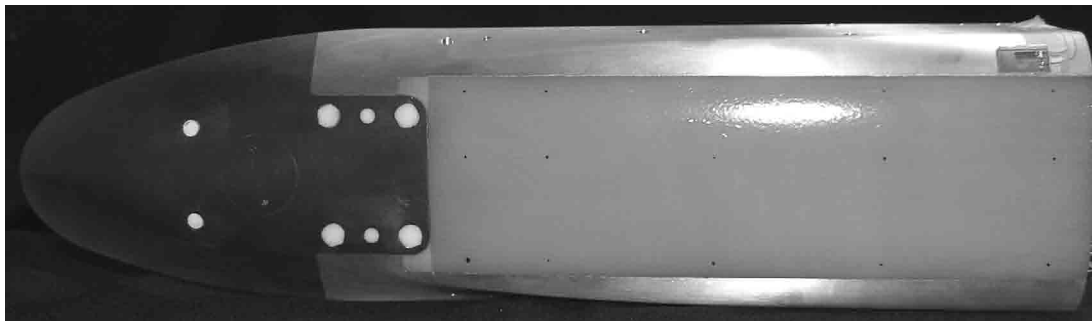
variation. This afterbody was also designed with a hollow channel through its center. This channel allowed a high-voltage wire to be run to a glow perturber that was later installed in the model nose.

The solid-aluminum afterbody was originally used for oil flow visualization and TSP measurements. About one year after receiving the model, experience suggested that better TSP data, possibly more quantitative in heat transfer, could be made with a nylon model instead of an aluminum one. That is why the afterbody with nylon inserts was fabricated. The original aluminum afterbody was later modified to allow PCB pressure sensors to be mounted flush with the model surface. The sensors were placed along the leeward surface centerline and were spaced 3.2 cm (1.25 in.) apart. The most downstream sensor was located 2.4 cm (0.95 in.) upstream of the model's downstream edge. Additionally, two holes were made to allow the installation of fast thermocouples or heat transfer gauges. These were located 1.9 cm (0.75 in.) downstream of the first and fourth PCB sensors. Unfortunately, the sensors did not arrive in time to be used. The holes were instead plugged with dowel pins and secured in the holes with nail polish. Additionally, a streamwise channel was drilled through the model to allow the glow perturber wire to pass through the model.

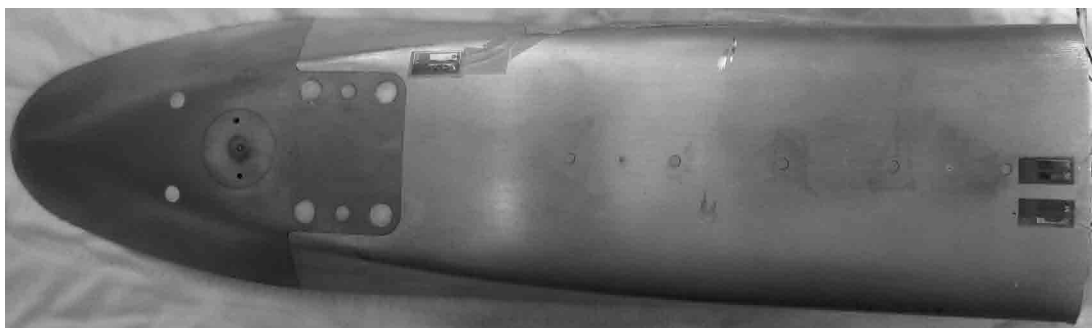
A photograph of the steel nose, windward model surface, and both of the leeward model surfaces is provided in Figure 2.4. Figure 2.5 shows a side view of the model.



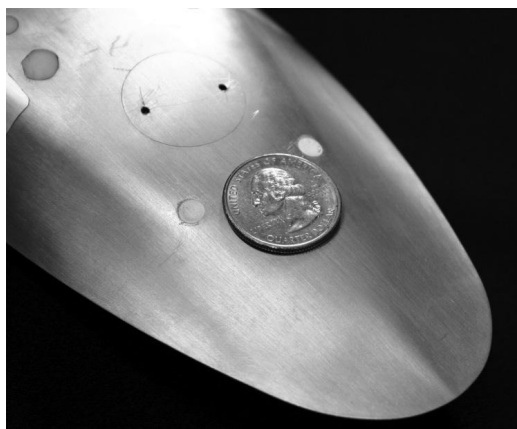
(a) Windward side of model with nylon insert



(b) Leeward side of model with nylon insert



(c) Leeward side of aluminum model



(d) Stainless steel nose with glow perturber insert

Figure 2.4: Photographs of the X-51A model

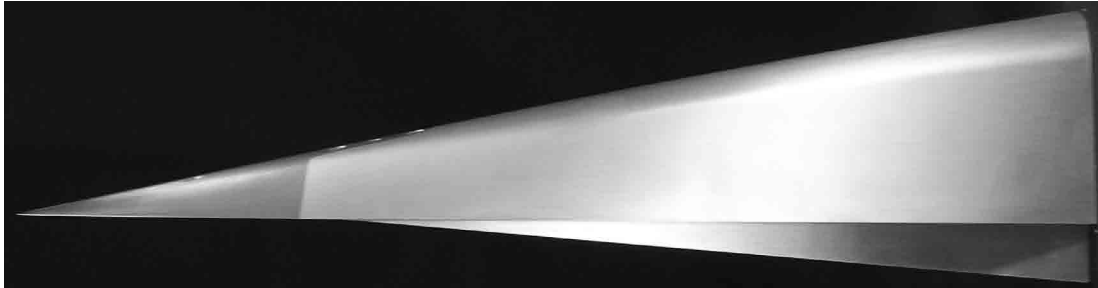


Figure 2.5: Side view of the X-51A model

## 3. INSTRUMENTATION

### 3.1 Temperature Sensitive Paint

#### 3.1.1 History and Background

Temperature sensitive paint has become a valuable and non-invasive experimental aerodynamic measurement tool. The paint is composed of an immobilized luminescent molecule in a polymer-based paint. Due to the process of thermal quenching (described in greater detail in section 3.1.3), the intensity of the luminescence decreases with increased temperature. TSP is capable of providing excellent spatial resolution (usually limited by the image acquisition system) as well as good temperature resolution, on the order of 0.2-0.8°C [46]. However, the error is largely dependent upon the particular experimental setup [47]. Using the known values of material properties, the acquired temperature data can be used to quantify the heat transfer.

Although TSP is a fairly recent innovation dating back only about 20 years, TSP's predecessors, thermographic phosphors and thermochromic liquid crystals, have been in use in aerodynamic applications since the 1950's. A family of thermographic phosphors can provide useful measurements across a temperature range from about 290 K up to 1600 K [46]. Unlike TSP, thermographic phosphors are typically applied to a model surface in powder or crystal form instead of being applied in a polymer paint [48]. TSP also has the benefit of being useful at cryogenic temperatures from about 100 K up to about 423 K [49]. A family of TSP's, used in supersonic and hypersonic experimentation, as well as in cryogenic applications, was developed at Purdue University [46].

### 3.1.2 Uses of TSP

TSP has been used in a wide range of aerodynamic conditions with varying degrees of effectiveness. The paints have been used in low-speed applications [50]. The TSP technique has also been used in Purdue’s Mach-6 tunnel. One inherent limitation of TSP as used in the Mach-6 tunnel is the low stagnation temperature. The corresponding low heat transfer means the signal-to-noise ratio is not as high as would be seen in higher enthalpy facilities. However, Matsumura [51] successfully employed the TSP technique on a generic scramjet forebody in the BAM6QT. He was able to detect streamwise vortices and also transition. He was unable to successfully reduce the temperature data to heat transfer, however. Swanson [52] also used TSP extensively in the Mach-6 tunnel. He observed crossflow vortices breaking down to turbulence on a cone. The methodology used in the present experiments is very similar to that used by Matsumura and Swanson.

Recently, Watkins et al. [53] utilized TSP to successfully quantify heat transfer and augmented heating from reaction control thrusters on Apollo and Orion-like reentry capsules at Mach 9.6 with a stagnation temperature  $T_0=1000$  K. Ref. [54] reports the development and use of TSP for use on Orion at Mach 10 in the Arnold Engineering Development Center’s hypervelocity Tunnel 9. Overcoming significant facility issues associated with the high Reynolds number and high enthalpy, quantitative heat transfer data have been extracted from the TSP.

### 3.1.3 Photophysics of TSP

TSP is based on the reversible process known as thermal quenching. When a molecule of the luminophore in a TSP absorbs a photon of radiation, it causes the molecule to transition from its ground-energy state,  $S_0$ , to an excited electronic state (e.g.  $S_1$ ,  $S_2$ ,  $T_1$ ), where the singlet state is denoted by  $S$  and the triplet state is denoted as  $T$  [46]. The singlet state maintains spin-pairing between the excited and ground state electrons while in the triplet state, the spins of the two electrons

become unpaired [48]. The first excited triplet state,  $T_1$ , is of lower energy than the first excited singlet state,  $S_1$ . The absorption and promotion to the first singlet state is described symbolically as  $S_0 + \hbar\nu \rightarrow S_1$  where  $\hbar$  is Plank's constant and  $\nu$  is the frequency of the excitation light.

Since lower energy states are preferred, the excited electron returns to the ground state through a combination of radiationless and radiative processes. The luminescent phenomenon known as fluorescence is the radiation transition from the first excited singlet state to the ground state:  $S_1 \rightarrow S_0 + \hbar\nu_f$  where  $\nu_f$  is the frequency of the emitted radiation. The transition from an excited triplet state to the ground singlet state is the luminescent process known as phosphorescence:  $T_1 \rightarrow S_0 + \hbar\nu_p$  where  $\nu_p$  is the frequency of the emitted radiation. Phosphorescence typically lasts longer than fluorescence.

The molecule can reach an excited triplet state through two mechanisms. It can be directly excited to the triplet state from the ground singlet. However, this process is much less probable than excitation to a singlet state [48]. An excited singlet state can undergo radiationless vibrational relaxation to the lower-energy triplet state. This is one form of radiationless deactivation. Additionally, excited singlet states can transition back to the ground state in a radiationless deactivation where the excess energy is released as heat:  $S_1 \rightarrow S_0 + \Delta$  where  $\Delta$  denotes the heat released [46].

If radiative transitions dominate the return to the ground state, then the emission intensity of the luminophore is high. If, however, radiationless transitions dominate, the emission intensity will be low. It has been shown that the dominance of one of these de-excitation pathways over the other (radiative vs. radiationless) is temperature dependent for some luminophores. Thermal quenching refers to the process of higher temperatures causing radiationless transitions to dominate de-excitation. Thus the emission intensity of the TSP can be used to determine the luminophore's temperature [55].

### 3.1.4 Quantitative Data from TSP

Since the emission intensity of certain luminophores is temperature dependent, there are two common methods used to collect quantitative temperature data from TSP. In both methods, the TSP is illuminated with a light source of the correct frequency to excite the luminophore.

For the technique used in the current research, the temperature cannot be determined directly from the local emission intensity due to non-uniform lighting and non-uniform TSP-layer thickness. Instead, the emission intensity is recorded for a nominally uniform model temperature just prior to running the tunnel. This is referred to as the “wind off” image. The model temperature is likely not completely uniform. After pressurizing the tunnel, the model temperature was allowed to equilibrate for no less than 30 minutes before running the tunnel. Under the conditions of interest, the emission intensity is recorded again. These images are the “wind on” images. A third image is recorded with the illumination source turned off and the ambient light reduced as much as possible. This image is subtracted from both of the images with illumination, on a pixel-by-pixel basis. Since they are subtracted off, this procedure removes the effect of both ambient light and dark current in the camera. A ratio of the two images then mostly removes the effects of non-uniform illumination. The signal-to-noise ratio from pixel to pixel then varies, but this effect is assumed to be negligible over most of the area of interest. The local TSP temperature can then be determined from a simple intensity-ratio calibration performed at known conditions.

In the TSP calibration, the emission intensity of a small coupon coated with TSP is recorded for a number of known temperatures. Choosing one of these temperatures as a reference condition, a ratio of the intensities corresponding to other temperatures to the intensity at the reference condition is calculated. The reference temperature should be equal to the nominally uniform temperature of the model prior to a run. These data then form a discrete set of intensity ratio and temperature combinations. A curve fit can be found for these points.

Figure 3.1 shows the TSP calibration rig. The TSP-coated coupon is attached to the end of a long metal post using Omega Omegatherm 201 thermal conductive paste. T-type thermocouple leads are secured between the post and the back side of the coupon. The thermocouple output is connected to an Omega Model 650 Type T Thermocouple Thermometer. The back side of the post is exposed to heat transfer fluid. The fluid's temperature is precisely controlled by a PolyScience digital temperature controller. The coupon and post are contained in a sealed vessel. There is thus some radiative heat transfer and free convective heat transfer from the post to the air, but convection should be minimized. It may be better to calibrate at vacuum to reduce the effects of convection, but the effect of convection was assumed to be small and the calibration was done at one atmosphere.



(a) Thermal fluid heater

(b) Calibration chamber

Figure 3.1: TSP calibration rig

A typical calibration curve is shown in Figure 3.2. Here, a reference temperature of 303 K was used, since that is the estimated model surface temperature. A fourth order least-squares fit of the temperature ratio and intensity ratio data yielded the following relation:

$$\frac{T}{T_{ref}} = -0.730\left(\frac{I}{I_{ref}}\right)^4 + 2.530\left(\frac{I}{I_{ref}}\right)^3 - 3.136\left(\frac{I}{I_{ref}}\right)^2 + 1.499\left(\frac{I}{I_{ref}}\right) + 0.837 \quad (3.1)$$



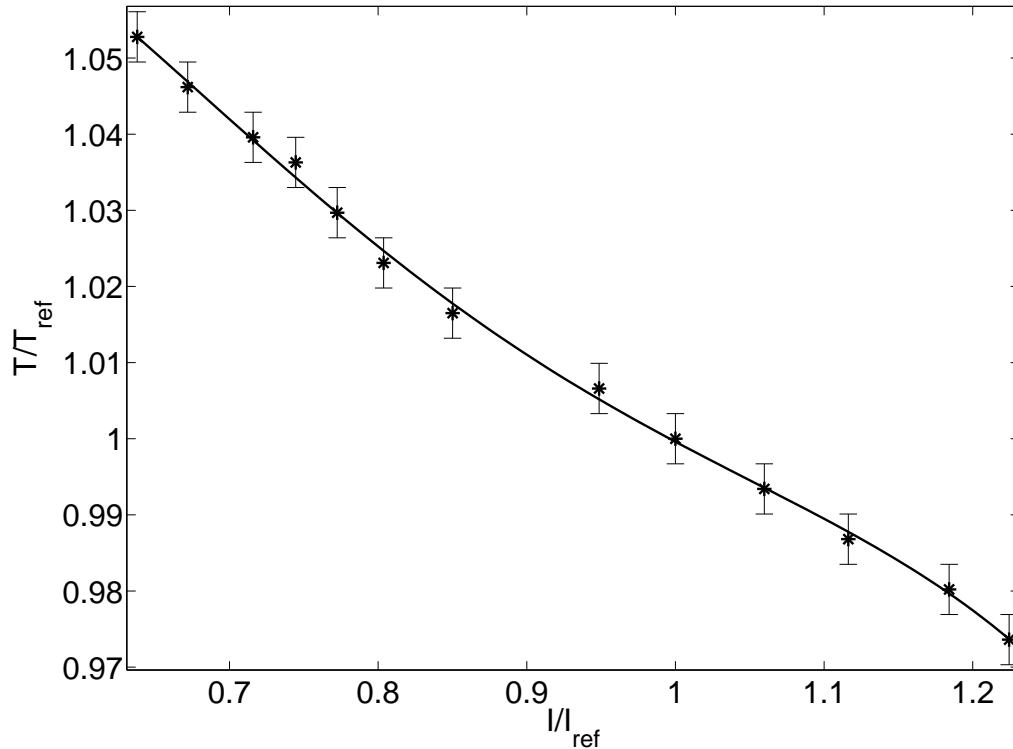


Figure 3.2: Typical TSP calibration

For the purposes of the present experiments, TSP is fairly quantitative in temperature. Efforts are underway to make it reliably quantitative in temperature and heat transfer. At present, the uncertainties associated with this method are too large for highly accurate quantitative results. However, this technique has demonstrated consistently that temperature scales monotonically with intensity. To reliably measure the location of transition, precise temperatures are not needed.

There are several uncertainties regarding this technique and its use in the BAM6QT. The effect of pressure on the luminescence of the paint is unknown. Matsumura et al. [56] did a preliminary investigation of this uncertainty using a different luminescent material that is known to be more sensitive to pressure. Additionally, the current calibration instrumentation only measures temperature to a precision of 1 K (1.8°R).

This introduces uncertainty into the calibration, as seen in the error bars in Figure 3.2. The effect of nonuniformities in the thickness of the paint layer is also unknown. The extent of lateral heat conduction, both in the paint layer and in the model substrate, is unknown. Finally, the effect of variations in the initial model-substrate temperature has not been thoroughly investigated.

The model generally moves during tunnel startup and during the tunnel run. This gives rise to some error when taking the ratio of the wind-on images to the wind-off image. Thus, an image registration and alignment technique was used to correct for model and tunnel movement. Registration marks were placed on the model in known locations. The model was held in place on a machining mill with a digital position readout. A marker was placed in the mill. Its position relative to the model was known to within about 1.5 mm (0.06 in.). Marks could then be placed on the model surface with their physical coordinates known. A commercial software package, OMS Lite, was used to align, subtract the background, and ratio the images. Pixel coordinates were then converted into physical coordinates by using the known locations of the registration marks to their corresponding pixel locations. An average pixel per length value was found by using the two most distant registration marks. This value was then used to find the physical locations of the registration marks relative to one another.

The window through which the model was imaged has a radius of curvature of about 12.1 cm (4.75 in.). This radius varies somewhat with streamwise distance. When the camera is mounted perpendicular to the window's centerline, curvature effects become increasingly significant for off-centerline locations. These effects were assumed to be negligible since the portions of the model that were imaged were nearly planar and only deviated from the centerline by about 1.5 cm (0.59 in.) for the windward surface and 3.1 cm (1.22 in.) for the leeward surface.

### 3.1.5 TSP Equipment

A Photometrics SenSysB scientific-grade charge-coupled device (CCD) camera was used to obtain all TSP images of the model's windward surface. Light at 464 nm was used to excite the paint. During each run, photographs were taken as fast as the hardware would allow, about one image every 0.6 s. When the oscilloscopes triggered at tunnel startup, the camera began taking pictures with a manually-set exposure length. The exposure was generally set to less than 200 ms. This camera had a resolution of 768 by 512 pixels.

All of the TSP images on the leeward side were taken with a PCO.1600 CCD digital camera. This camera had a pixel resolution of 1600 by 1200 pixels, substantially increasing the spatial resolution. No binning was ever used. Again, the manually set exposure length was typically less than 200 ms. In order to take the maximum number of images possible, an external triggering signal was necessary for each individual image. In this configuration, images could be captured at a maximum rate of about 3.3 Hz.

Both cameras output a signal when the shutter is open. This signal was recorded and used in subsequent data processing, along with stagnation pressure measurements, to calculate the Reynolds number for each image. The process for Reynolds number calculations is described in detail in Section 3.5.

## 3.2 Hot Wires

A hot wire was used to make measurements of mean flows and boundary-layer disturbances. A hot-wire probe consists of a length of very fine wire (on the order of 0.0002 inches in diameter) welded between two probe arms. The probe is then typically connected to a constant temperature anemometer (CTA), a constant current anemometer (CCA), or a constant voltage anemometer (CVA). The CTA and CCA are the most commonly used anemometers [57].

A hot wire acts as the fourth leg of a Wheatstone bridge electronic circuit. A CTA schematic can be seen in Figure 3.3. The CTA operates by holding the hot wire at a fixed temperature that is higher than the surrounding fluid. As the fluid flows past the wire, the amount of heat transfer from the wire to the fluid changes as the flow changes. The changing heat flux from the wire to the flow changes the wire temperature. This unbalances the Wheatstone bridge. The amplifier responds very rapidly by changing the electric potential across the wire. This restores the wire temperature, and thus its resistance, back to the original set value, effectively balancing the bridge. By recording this ‘bridge’ voltage and applying a calibration, it is possible to infer the mass flow or stagnation temperature of the fluid past the wire, depending on the wire overheat ratio,  $\tau$ . The overheat ratio is directly related to the wire temperature. In order to determine if the wire temperature is high enough to make the CTA most sensitive to mass-flux fluctuations,  $\tau$  must be calculated.  $\tau$  is defined as follows:

$$\tau \equiv \frac{T_w - T_e}{T_0} \quad (3.2)$$

where  $T_e$  is the recovery temperature of the wire, and  $T_0$  is the stagnation temperature in the flow.  $T_e$  is near, but not equal to  $T_0$  for supersonic flow. The wire does not fully recover the stagnation temperature due to viscous dissipation of energy. For continuum flow,  $T_e/T_0$  was found to be 0.95-0.97 for a wide range of supersonic Mach numbers. This is a result of the Mach-number independence principle [58]. For high overheat ratios, greater than about  $\tau=1$ , the hot wire becomes most sensitive to mass-flux fluctuations. For lower overheat ratios, the hot wire is most sensitive to temperature changes [58].

To accurately determine the temperature of the wire, a simple calibration must be performed. The wire must be held at a fixed and known temperature and its resistance recorded. The temperature is then adjusted to a number of values and the wire resistances recorded. They are then fit to the following relation, given in Ref. [59]:

$$R_w = R_{ref}(1 + \alpha(T_w - T_{ref})) \quad (3.3)$$

where  $R_w$  is the wire resistance,  $R_{ref}$  is the wire resistance at some reference temperature,  $T_w$  is the wire temperature, and  $T_{ref}$  is the reference temperature, and  $\alpha$  is the temperature coefficient of resistance and is determined from a least squares linear fit of the data. Thus, for a selected wire resistance, the wire temperature can be found from Eq. 3.3.

For the wires used in the present work,  $R_w/R_{ref}$  was generally set to about 1.8, with  $T_{ref}$  as room temperature, 294 K (529.2°R). The ratio  $T_e/T_0$  is assumed to be 0.96, and  $\alpha$  for one 0.0051 mm- (0.0002 in.) diameter wire was found to be 0.0012 K<sup>-1</sup> (0.00067°R<sup>-1</sup>). For  $R_w/R_{ref}$ ,  $T_w$  and  $\tau$  were found to be 961 K (1730°R) and 1.26, respectively. When  $R_w/R_{ref}$  was reduced to 1.7, this changed the values of  $T_w$  and  $\tau$  to 877 K (1579°R) and 1.07, respectively. In both instances,  $\tau$  is high enough to make the CTA be primarily sensitive to mass flux.

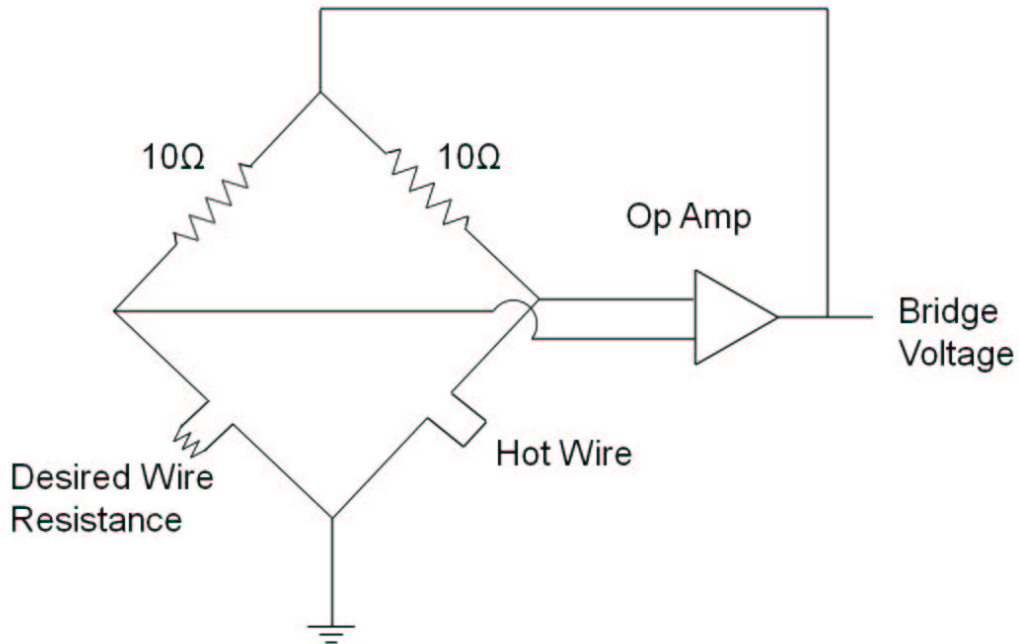


Figure 3.3: Simplified CTA circuit

Due to the short run times and the changing stagnation conditions in the BAM6QT, hot wires cannot be calibrated *in situ* as would be preferred. Instead, following Rufer's method [20], hot wires were calibrated in the SSJ. Although the stagnation temperature and pressure can be independently varied in this facility, the conditions in the BAM6QT cannot be replicated. At present, a Mach number of 4 is the highest that the jet can run. Nevertheless, reasonable calibrations that fall within the scatter of benchmark calibration data can be obtained.

In order to calibrate the wire, it was installed in the SSJ. Prior to starting the facility, the wire was tuned to the maximum possible frequency response and was positioned above the location of the jet. This keeps the wire from experiencing the large, unsteady forces of startup. After the jet was successfully running at the set stagnation pressure, the plenum heater temperature was increased and the jet was run until the stagnation temperature was near 160°C (320°F). The wire was then gently lowered into the flow. The stagnation pressure was varied from 138 to 276 kPa gauge (20 psig to 40 psig). Static temperature and pressure were measured in the plenum. These quantities are equal to the stagnation conditions in the jet due to isentropic expansion. The temperature was measured using a type J thermocouple and a Fluke 51 II digital thermometer. The pressure was monitored using an Ashcroft temperature-compensated test gauge with a range of 0-100 psig and an accuracy of 0.25%. Below 138 kPa gauge (20 psig), Rufer [20] reports large separations that change the mean flow characteristics. Unfortunately, the mass fluxes corresponding to those lower pressures ( $< 48 \text{ kg/m}^2\text{s}$ ,  $9.8 \text{ lb/ft}^2\text{s}$ ) are closer to the mass fluxes in the Mach-6 tunnel. For each of seven pressures, the plenum pressure and temperature were recorded and the output voltage from the CTA was recorded on a digital oscilloscope for one second.

The relationship between anemometer voltage and mass flux is of the following form [60]:

$$e^2 = Af(\tau) + Bg(\tau)(\rho U)^n \quad (3.4)$$

where  $e$  is the anemometer voltage,  $\rho U$  is the mass flux,  $A$  and  $B$  are empirical constants,  $n$  is a function of flow and wire parameters, and  $f$  and  $g$  are functions of the overheat ratio. In the jet, the stagnation temperature, and thus the wire overheat ratio, were held as close to constant as possible. The stagnation temperature actually varied from 150.7 to 156.6°C. With the assumption of constant  $\tau$ ,  $f$  and  $g$  in Eq. 3.4 are also constant and assumed to be unity. Following Rufer's method,  $n$  was taken to be 0.7.  $A$  and  $B$  can then be found by relating the bridge voltage for known mass flux at constant stagnation temperature.

The mass fluxes for the various conditions in the SSJ were found in the following manner. Mass flux, by making use of the ideal gas law, can be expressed as

$$\rho U = \frac{P}{RT} Ma = \frac{P}{RT} M \sqrt{\gamma RT} = PM \sqrt{\frac{\gamma}{RT}} \quad (3.5)$$

where  $P$  is static pressure,  $T$  is static temperature,  $R$  is the gas constant for air,  $M$  is the Mach number, and  $\gamma$  is 1.4, the ratio of specific heats for air. Assuming an isentropic expansion through the nozzle, mass flux can be expressed in terms of stagnation conditions as follows:

$$\rho U = P_0 M \sqrt{\frac{\gamma}{RT_0} \left(1 + \frac{\gamma - 1}{2} M^2\right)^{\frac{-\gamma - 1}{\gamma - 1}}} \quad (3.6)$$

Quantities with a subscript 0 are stagnation conditions. Rufer found the Mach number in the jet to be a nearly constant 3.9 over the calibration pressure range. This value was used for mass flux calculations. In this manner, the recorded bridge voltages corresponded to known mass fluxes. A least-squares linear curve fit was found relating  $(\rho U)^{0.7}$  to  $e^2$ , effectively solving for  $A$  and  $B$  in Eq. 3.4. A sample calibration is shown in Figure 3.4. The Mach-6 tunnel provides freestream mass fluxes up to about 90 kg/(m<sup>2</sup>s). This corresponds to  $(\rho U)^{0.7}$  of 24 (kg/(m<sup>2</sup>s))<sup>0.7</sup>. However, the tunnel was not operated at these conditions. The calibrated hot wire was used for freestream  $\rho U \approx 30$  kg/(m<sup>2</sup>s). The corresponding  $(\rho U)^{0.7}$  is only 11 (kg/(m<sup>2</sup>s))<sup>0.7</sup>. Measurements in the model boundary layer are even lower than this. Thus, the calibration must be extrapolated in order to quantify measurements in the boundary

layer. The calibration should still hold in the supersonic portion of the boundary layer due to the Mach-number independence principle.

Thus, for a given anemometer voltage at the same stagnation temperature as was used in the calibration, mass flux can be easily calculated. If the Mach-6 tunnel is run at the same stagnation temperature as was used in the calibration, 433 K, the calibration should be valid in the Mach-6 tunnel.

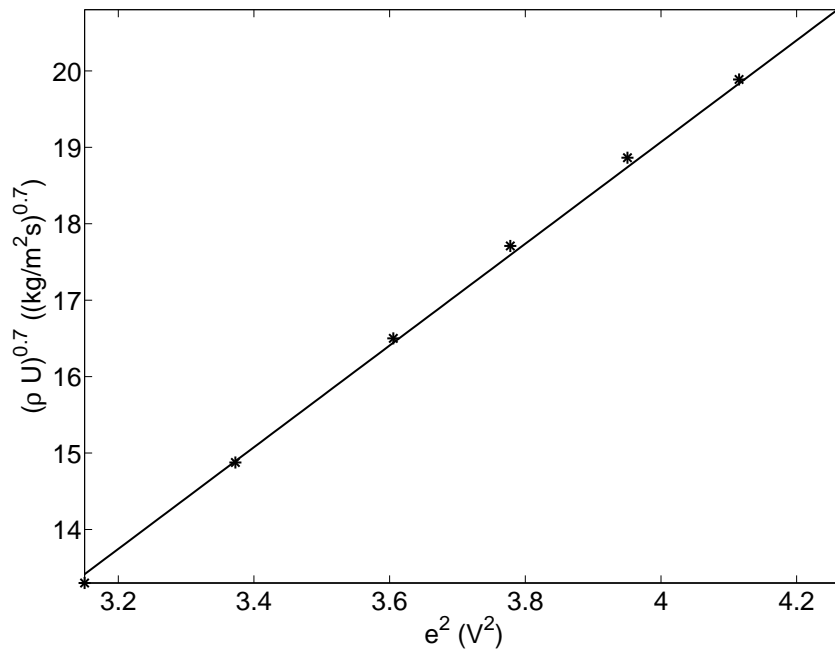


Figure 3.4: Sample hot-wire calibration

For all hot-wire data presented, the CTA was a TSI IFA100 anemometer. The 1:1 bridge was always used. The electronics for the 1:1 bridge were custom modified to allow high frequency responses to be obtained. Using the 1:1 bridge, a static resistor equal to the desired hot-wire resistance is used in the arm of the Wheatstone bridge opposite the hot wire.

An Infinity Model K2 long-distance microscope was used to determine the distance a hot-wire probe was from the model. The microscope was fitted with corrective optics



used to mitigate the effect of the curvature of the tunnel window. The microscope was placed as close to the window and the location at which it would be used as possible. When looking through the eyepiece, enumerated hash marks are visible. The hot wire was aligned with one of the hash marks and moved a known distance using a computer-controlled traverse. The number of marks that the probe moved as viewed through the eyepiece was counted, and a mark per mm (0.04 in.) value was obtained. Typically, there were 8-9 marks per mm (0.04 in.). The number of marks between the wire and model could then be converted into a distance. Often, it was difficult to determine a precise location for the model surface and the hot wire. Even with the corrective optics, the microscope could not focus perfectly on the wire.

### 3.3 PCB Pressure Sensors

Five PCB 132A31 piezoelectric fast pressure transducers were surface-mounted in the model and used to make measurements of disturbances in the boundary layer. The sensors have a diameter of 3.18 mm (0.125-in.). They cannot measure mean pressures. Rather, these sensors are designed to sense high-frequency fluctuations. They are commonly used to measure the arrival time of shock waves. Although not designed specifically to measure second-mode instabilities in hypersonic boundary layers, they have, to date, been very successful at this task. Amplitudes of measured pressure fluctuations were found by applying the manufacturer-supplied voltage/pressure sensitivity.

Holes for the sensor were drilled for a slip fit around the sensor. The sensors were held in the model by coating both the inside of the holes and also the outside of the sensors with nail polish. This should allow them to be removed with relative ease without damaging them.

### 3.4 Oscilloscopes

With the exception of TSP images, all data were recorded using Tektronix digital oscilloscopes. Two model DPO7054 oscilloscopes were available, as well as one model TDS7104. All three oscilloscopes were always operated in “Hi-Res” mode whereby data were sampled at more than the set sampling frequency and then averaged real-time into memory at the set sampling rate. This allowed an increase in signal resolution.

### 3.5 Freestream Reynolds Number Calculation

For Reynolds number calculations, the stagnation pressure was measured using a Kulite model XTEL-190-200A pressure transducer that is surface mounted in the entrance to the contraction. The Mach number there is very low. Thus, the static pressure at this location is essentially equal to the stagnation pressure in the nozzle. Static pressure in the nozzle was found by assuming isentropic expansion through the nozzle and using the isentropic pressure relation. The Mach number was taken to be 6.0 for quiet runs and 5.8 for noisy runs.

As per Ref. 61, the stagnation temperature was found by the following relationship:

$$\frac{T_0}{T_{0,i}} = \frac{P_0}{P_{0,i}}^{\frac{\gamma+1}{\gamma-1}} \quad (3.7)$$

where  $T_0$  and  $P_0$  are the stagnation temperature and pressure, respectively,  $T_{0,i}$  and  $P_{0,i}$  are the stagnation temperature and pressure at the beginning of a tunnel run, respectively, and  $\gamma$  is the ratio of specific heats for air, 1.4. Here,  $T_{0,i}$  was assumed to be 433 K (779 °R), the set temperature of both the driver tube and the air entering it. The static temperature in the nozzle was found using the isentropic temperature relation. Sutherland’s law was used to find viscosity at the calculated static temperature. The velocity in the nozzle was found by using the assumed Mach number and the calculated static temperature in the nozzle. Finally, the static density was found by assuming a perfect gas and using the perfect gas law. Thus, by measuring

the pressure in the contraction entrance, the freestream Reynolds number could be calculated for any time during a tunnel run.

## 4. WINDWARD MEASUREMENTS

### 4.1 Motivation

It is important that the boundary layer entering the scramjet inlet on the windward surface of the model be turbulent. A turbulent boundary layer is less susceptible to separation resulting from a shock/boundary layer interaction. The shock train in the isolator of a scramjet engine could potentially separate a laminar boundary layer there. A separated boundary layer in the engine may cause it to unstart and not produce any thrust. This could end in a loss of the vehicle.

In order to ensure a turbulent boundary layer entering the inlet, an array of discrete roughness elements is to be used as boundary layer trips on the X-51A upstream of the compression corner on the vehicle's windward surface. The sizing of the boundary layer trips is a balance between two competing effects. The trips must be large enough to cause transition. If the trips are too large, however, they could cause excessive momentum loss, possibly invalidating propulsion measurements [62]. Oversized trips will also add unnecessary drag to the vehicle, adversely impacting performance.

Freestream noise is known to induce early boundary-layer transition for some transition mechanisms. If this were also true for roughness-induced transition, such as that on the windward surface of the X-51A, a potential sizing problem arises. If the trips were sized based on experiments in facilities with conventional noise levels, the trips may be effective in a high-noise environment. However, with the low freestream noise levels of flight, those trips could prove to be ineffective if freestream noise affects roughness-induced transition. Thus, a study of the effectiveness of several boundary layer trip geometries with conventional-tunnel and low flight-like noise levels was performed.

A smooth strip and three trip strips with different roughnesses were used in the model at a streamwise location of  $x=6.30$  cm (2.48 in.). Two of the trip strips are composed of ramp-shaped roughness elements while the other has diamond-shaped trips. The roughnesses have the same geometry as those used by Berry et al. [63] on the Hyper-X model. Berry's trips were designed to generate a series of counter-rotating vortex pairs that were somewhat smaller than the boundary layer height. The diamond-shaped trips had been found to be successful for experiments at NASA Langley involving the Space Shuttle Orbiter, X-38, NASP, Hyflite, and HySTP programs. The particular trip geometries were of interest to the Boeing Company and were supplied to the author.

A photograph of the three types of strips used in the Purdue model can be seen in Figure 4.1. Here, the flow is from top to bottom. The upstream edges of the ramp roughnesses are at the same height as the model surface. Moving downstream, they rise up above the model surface and also become increasingly narrow. At the downstream edge, the ramps of one trip strip have a maximum height of 0.076 cm (0.030 in.). The maximum ramp height on the other strip is 0.038 cm (0.015 in.). Due to difficulties in getting the larger roughness strip to fit in the model, a 0.013 cm (0.005 in.) shim was placed under the insert. This caused small forward-facing steps at both the upstream and downstream edges of the strip. A skilled machinist measured the step heights along the centerline and found them to be about 0.013 cm (0.005 in.) for the upstream step and 0.008 cm (0.003 in.) for the downstream step. The diamond-roughness strip has diamond-shaped roughness elements that are 0.305 cm (0.120 in.)-wide across the diagonal and 0.152 cm (0.060 in.) high. The diamond strip was flush with the model surface. For the ramp strip, the model centerline runs between two roughness elements. For the diamond case, the centerline runs directly through a roughness element.

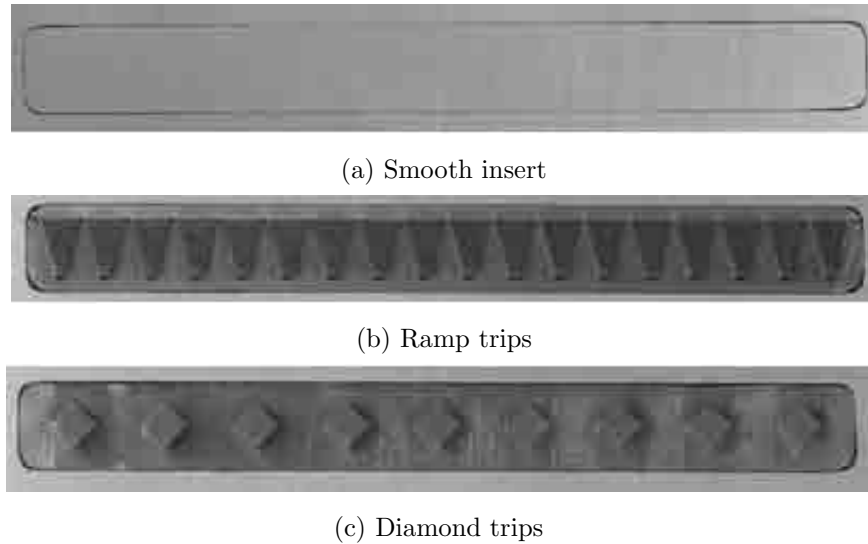


Figure 4.1: Trip inserts for model. Flow is top to bottom.

## 4.2 Effect of Tunnel Noise on Roughness-Induced Transition

Separate runs were made with an initial stagnation pressure of 655 kPa (95 psia) with each insert in the model. The tunnel was run under noisy and quiet conditions to assess the effects of noise on natural and roughness-influenced transition. This pressure was selected because, at the time, it was the highest stagnation pressure for which the tunnel gave low freestream noise levels.

When the tunnel is run noisy (with the throat bleed suction turned off), the total mass flux out of the driver tube decreases by about 27.5% from the bleeds-open case [64], the nozzle-wall boundary layer becomes turbulent, the flow becomes noisy, and the mean Mach number decreases from about 6.0 to about 5.8 due to the difference in the displacement thicknesses between the laminar and turbulent boundary layers. This, in turn, means that the freestream Reynolds-number drop with time is less with the bleeds closed than with the bleeds open. When comparing data taken under noisy and quiet conditions, a choice needed to be made regarding whether to compare data at the same freestream Reynolds number or to compare data taken at the same time after the start of the run. The problem with comparing data at the same Reynolds

number is that these data were taken at significantly different times during the run. It has been observed that over the course of a run, the mean temperature of the nylon increases. This affects the TSP data.

This effect can be clearly seen in Figure 4.2. Shown here are streamwise temperatures for two different runs with low noise, initial stagnation pressures of 804 and 939 kPa (116.6 and 136.2 psia), and equal initial stagnation temperatures of 433 K (779°R). The runs will be referred to as Run A and Run B, respectively. The gaps in the data are due to the registration marks along the model centerline. The dashed line denotes the location of the compression corner. These data were collected when the freestream Reynolds numbers were matched at  $8.5 \times 10^6/\text{m}$  ( $2.6 \times 10^6/\text{ft}$ ). This condition was met at time  $t=0.7$  s for Run A and  $t=5.3$  s for Run B. For Run A, the stagnation pressure had decreased 2.4% and the stagnation temperature had decreased by 1.4%. For Run B, these values were 28.2% and 9.4%, respectively. Even though the freestream Reynolds numbers are matched for these streamwise plots, the mean streamwise temperature of Run B at  $t=5.3$  s is 4.7 K (8.3°R) higher than the mean streamwise temperature of Run A at  $t=0.7$  s. This is a significant difference considering that the maximum temperature change along the centerline for the data from Run A is only 5.5 K (9.9°R). Additionally, the streamwise location of the highest temperature does not match for the two cases; for Run B, it is 1.4 cm (0.6 in.) downstream of the peak shown for Run A.

Thus, images taken at different times during the run are not readily compared in terms of temperature or heat transfer. It was therefore decided to compare data taken at similar times into a run. This leads to a small variation in Reynolds numbers when comparing these data. The difference in the Mach number between quiet and noisy tunnel runs also leads to a difference in Reynolds number for equal stagnation conditions.

In addition to the TSP data, an uncalibrated polyimide-substrate hot film was glued on 26.7 cm (10.5 in.) downstream of the leading edge and about 3.18 cm (1.25 in.) off the centerline, as shown in Figure 2.4b. The manufacturer-supplied tem-

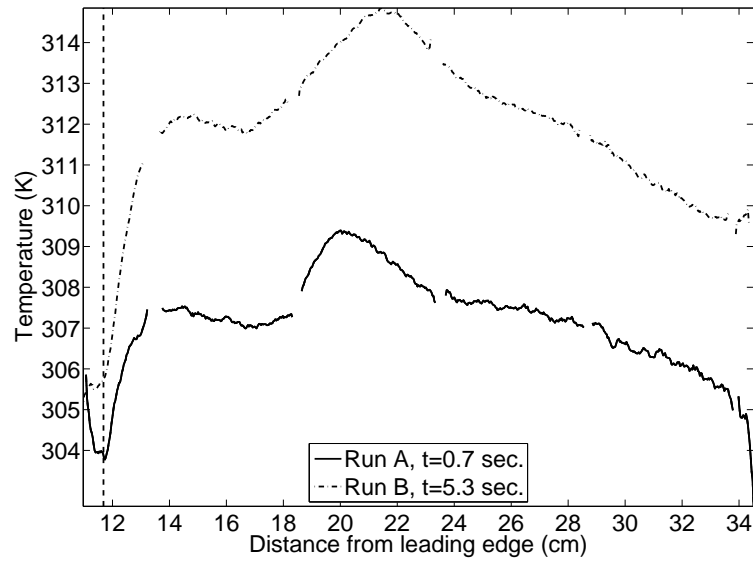


Figure 4.2: Centerline temperature for two runs at  $Re=8.5\times 10^6/m$  ( $2.6\times 10^6/ft$ ), but different times during the runs due to different initial conditions

perature coefficient was  $0.34\%/^{\circ}C$ . It was always operated with an in-house constant temperature anemometer (CTA) at an overheat ratio of 1.31, based on resistances, giving the film a temperature of 389 K ( $700^{\circ}R$ ). This hot film was used to determine if the boundary layer was laminar or turbulent. Schmisser et al. [65] used a similar technique in Purdue’s Mach-4 quiet tunnel.

The hot-film temperature, 389 K ( $700^{\circ}R$ ), is significantly less than the 433 K ( $779^{\circ}R$ ) stagnation temperature in the tunnel. This is also likely less than the recovery temperature. The manufacturer-supplied information stated that the hot-film temperature should not be above 423 K ( $762^{\circ}R$ ). It is questionable how the film could work properly since it was probably not hot compared to the local flow. The model was at a much lower temperature, only about 300 K ( $540^{\circ}R$ ). A simple Taylor-Maccoll code was run for a 4-degree half-angle cone at Mach 6.1 and a stagnation temperature of 433 K ( $779^{\circ}R$ ) in order to find a very rough estimate of the edge temperature. For the cone case, the edge temperature was 56 K ( $101^{\circ}R$ ). This gives a very rough idea of the model edge temperature. However, the model geometry is distinctly different



from that of a cone. The hot-film signal is uncalibrated and thus only useful for qualitative analysis.

The data were recorded on the Textronix DPO7054 oscilloscope at a sampling rate of 2 million samples per second. The oscilloscope was operated in ‘Hi-Res’ mode whereby the 8-bit data were sampled at a higher frequency and then averaged real-time into memory to obtain 11-12 bits at the set sampling frequency.

TSP and hot-film data will first be presented for the smooth-insert case. TSP and hot-film data will then be shown for the ramp trips and also for the diamond trips. At present, the TSP technique is not able to provide reliable quantitative heat-transfer rates. In order to verify what was suspected from the TSP data, a hot wire boundary-layer probe was used to determine the state of the windward boundary layer at different streamwise locations for the quiet runs with trip strips. The hot-wire data will be shown for a slightly lower freestream Reynolds number than the TSP data. When the hot-wire data were collected, the maximum quiet pressure in the BAM6QT had dropped from 655 kPa (95 psia) to around 552 kPa (80 psia). This meant that hot wires could not be used at the same conditions as those in the previous measurements. It was thought that the 11% drop in initial Reynolds number would not make much difference in the results. Nevertheless, for completeness, new TSP images at the reduced quiet flow conditions were obtained for the ramp and diamond roughness inserts. Additionally, at this reduced pressure, the nozzle-wall boundary layer tended to separate for about one second some time between 1.0 and 1.5 seconds into the run. Thus, images shown for the reduced quiet pressure runs were always the second image captured, instead of the fourth as for the higher-pressure runs. This was generally about 0.7 s into the run, as opposed to 1.7 s for the higher pressure runs.

### 4.2.1 Smooth Insert

Figure 4.3 shows the surface temperature distributions with the smooth insert under quiet and noisy conditions, at freestream Reynolds numbers of  $6.59$  and  $7.4 \times 10^6/\text{m}$  ( $2.0$  and  $2.3 \times 10^6/\text{ft}$ ), respectively. The stagnation temperatures ( $T_0$ ) and pressures ( $P_0$ ) were  $T_0=418$  K ( $752^\circ\text{R}$ ) and  $P_0=586$  kPa ( $85$  psia) with the tunnel running quietly. With the noisy tunnel,  $T_0=424$  K ( $763^\circ\text{R}$ ) and  $P_0=621$  kPa ( $90$  psia). The dashed red line indicates the compression corner. Figure 4.4 shows the streamwise temperature distribution on the centerline. The gaps in the data are due to the registration marks on the model surface. The compression corner is marked by the dashed black line.

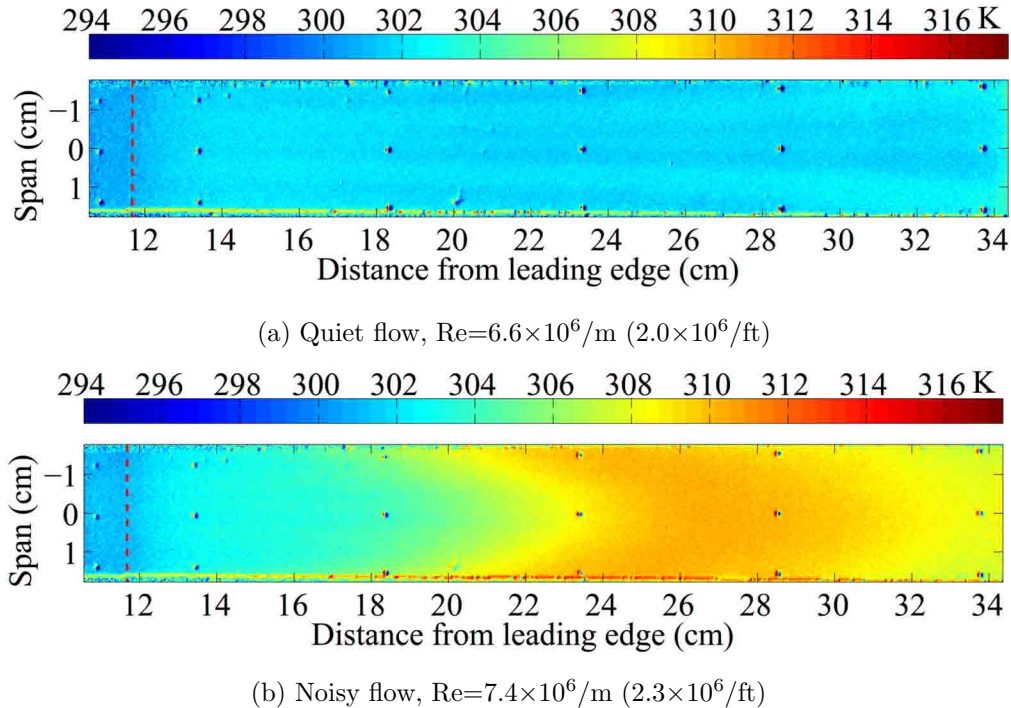


Figure 4.3: Surface temperature (K) under quiet and noisy conditions with smooth trip insert

Under quiet conditions, both the TSP image and the centerline temperature distribution show that the temperature increases downstream of the compression corner

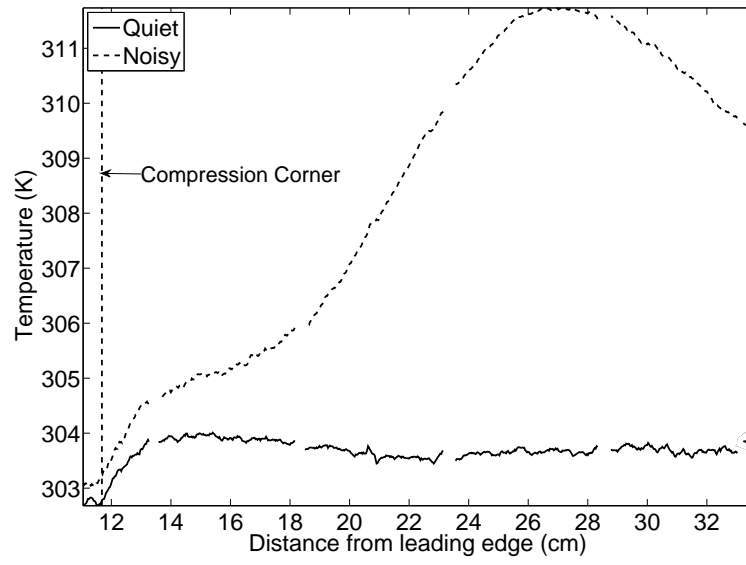


Figure 4.4: Centerline temperature for smooth insert, quiet and noisy flow

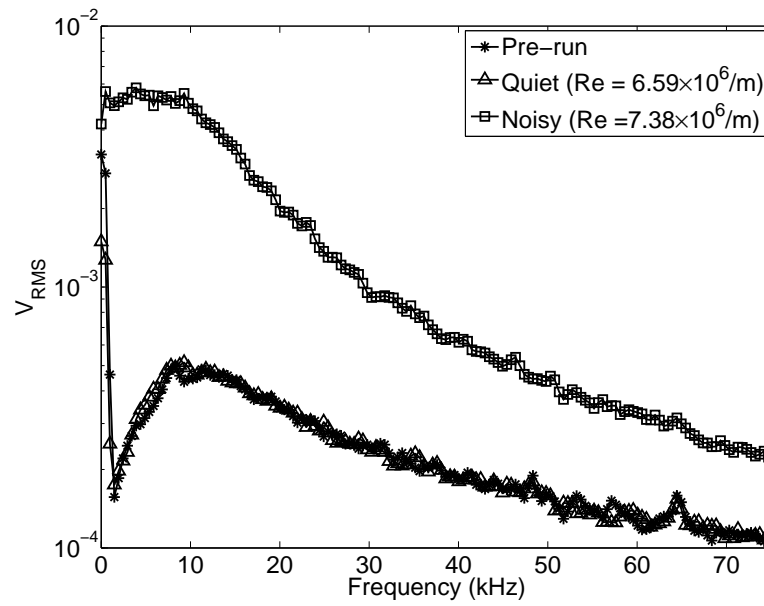


Figure 4.5: Hot-film spectra for smooth insert, quiet and noisy

followed by a nearly monotonic decrease for the rest of the extent of image. This strongly suggests a laminar boundary layer over the entire length of the nylon insert. Faint streaks are also visible in the TSP image. They are most likely due to the presence of streamwise vortices near the model surface. Refs. 66 and 67 both report seeing similar “striations” in hypersonic flow downstream of a compression corner. In both cases, they are attributed to the formation of Görtler vortices over the concave flow curvature near the reattachment region downstream of the corner. It seems likely that the streaks here are likewise due to Görtler vortices.

Figure 4.5 shows hot-film spectra for pre-run, quiet, and noisy data that also suggest that the boundary layer is laminar toward the aft end of the model since the quiet-tunnel spectrum falls nearly on top of the pre-run spectrum. The low power of the low frequencies, especially when compared to the noisy tunnel data, are indicative of a laminar boundary layer. A turbulent boundary layer is expected to have much higher power, especially for low frequencies.

The results for the noisy tunnel case are very different and clearly discernible in Figures 4.3-4.5. For the noisy case, after the expected rise at the corner, the temperature rises at an increased rate starting at about  $x=17.8$  cm (7.0 in.), peaks at about  $x=26.8$  cm (10.6 in.), and then decreases to the end of the model. This sudden rise in surface temperature is a strong indicator of transition onset. The much higher power in the hot-film spectrum also strongly suggest transition under noisy tunnel conditions. From Figure 4.4, it is reasonable to assume that centerline transition onset takes place at around  $x=14.0$  cm (5.5 in.). This is where the centerline surface temperature under noisy conditions significantly departs from that under quiet conditions. Although no hot-wire measurements were made to confirm TSP results with the smooth-wall case, hot-wire measurements with transition induced by roughness strips do support these conclusions.

A better method of transition-onset determination would be to compare experimental heat transfer rates to computed laminar heating rates. Transition onset is taken to be the location where the measured heat transfer departs from the com-

puted laminar value. This technique has been used successfully by NASA. See, for instance, Refs. 68–70. However, for the present work, laminar heating rates are not available and the TSP does not provide accurate heat transfer. Thus, assuming transition when the surface temperature departs from the nominally laminar case is the transition onset criterion used for these experiments.

It is difficult to know whether the distance from the leading edge, distance from the strip, or distance from the compression corner is the appropriate length parameter for transition. The presence of the compression corner likely has a destabilizing effect on the the boundary layer [71]. However, it may be that the distance from the trips is the most important length factor. For the smooth-walled case, however, the distance from the nose is taken to be the most important length. Transition Reynolds numbers based on freestream conditions and all three lengths will be reported. It would be better to calculate the Reynolds number based on edge conditions. Obtaining edge conditions is beyond the scope of the current effort.

Reducing freestream noise levels from conventional to quiet levels caused the transition Reynolds number based on distance from the nose to increase by a factor of at least 2.2 from  $1.0 \times 10^6$  to greater than  $2.3 \times 10^6$ . The actual increase cannot be determined since the flow is laminar past the end of the model under quiet conditions at the maximum quiet Reynolds number. The transition Reynolds number based on distance from the strip increases by a factor of at least 3.2 from  $0.6 \times 10^6$  to at least  $1.9 \times 10^6$ . Based on distance from the corner, the transition Reynolds number increases by a factor of at least 8.9 from  $0.2 \times 10^6$  to  $1.5 \times 10^6$ . The results are summarized in Table 4.1.

The vortices observed under quiet flow suggest that the dominant natural, untripped transition mechanism may not be only due to the amplification and breakdown of first or second mode waves. Spanwise spreading of the streamwise vortices indicates outward directed cross flow. Natural transition may be dominated by the breakdown of vortices generated by the three-dimensional leading-edge, three-dimensional cross-flow, or the Görtler instability near the reattachment region. Transition may also be

Table 4.1: Transition Reynolds numbers with smooth trip insert

$Re_L$	Noisy	Quiet	Increase
Nose	$1.0 \times 10^6$	$>2.3 \times 10^6$	$>2.2$
Trips	$0.6 \times 10^6$	$>1.9 \times 10^6$	$>3.2$
Corner	$0.2 \times 10^6$	$>1.5 \times 10^6$	$>8.9$

due to some complex coupling of these modes with a shear layer instability above a separation bubble at the corner [71].

#### 4.2.2 Ramp Roughness Insert: 0.76-mm Maximum Height

Figure 4.6 shows the surface temperature distribution with the larger of the two ramp roughness strips under quiet and noisy conditions for  $Re=6.6$  and  $7.5 \times 10^6/m$  ( $2.0$  and  $2.3 \times 10^6/ft$ ), respectively. Here,  $k_{max}$  is the maximum height of the roughnesses and is  $0.76$  mm ( $0.030$  in.) for the larger ramps. For the quiet case,  $T_0=418$  K ( $752^\circ R$ ) and  $P_0=586$  kPa ( $85$  psia), while under noisy conditions  $T_0=424$  K ( $763^\circ R$ ) and  $P_0=627$  kPa ( $91$  psia). There are clearly significant temperature differences in both the streamwise and spanwise directions. No single cut of temperature can completely capture these variations.

Figure 4.7 shows the streamwise centerline temperature as well as the streamwise temperature along the line  $y=-0.2$  cm ( $-0.08$  in.) for both noisy and quiet cases. The  $y=-0.2$  cm ( $-0.08$  in.) corresponds to a trough in the temperature. Here, each point along the centerline is the mean temperature of a  $9$  streamwise- by- $7$  spanwise-pixel rectangle while each point along  $y=-0.2$  cm ( $-0.08$  in.) is the mean temperature of a  $9$  streamwise- by  $3$  spanwise-pixel rectangle. The size of the averaging rectangles were different because of the large temperature gradients in the  $y$  direction and the relatively thin regions of lower temperature between the high-temperature streamwise

streaks. Figure 4.8 shows several spanwise temperature distributions under quiet flow. Figure 4.9 shows spectra of the surface hot film signal.

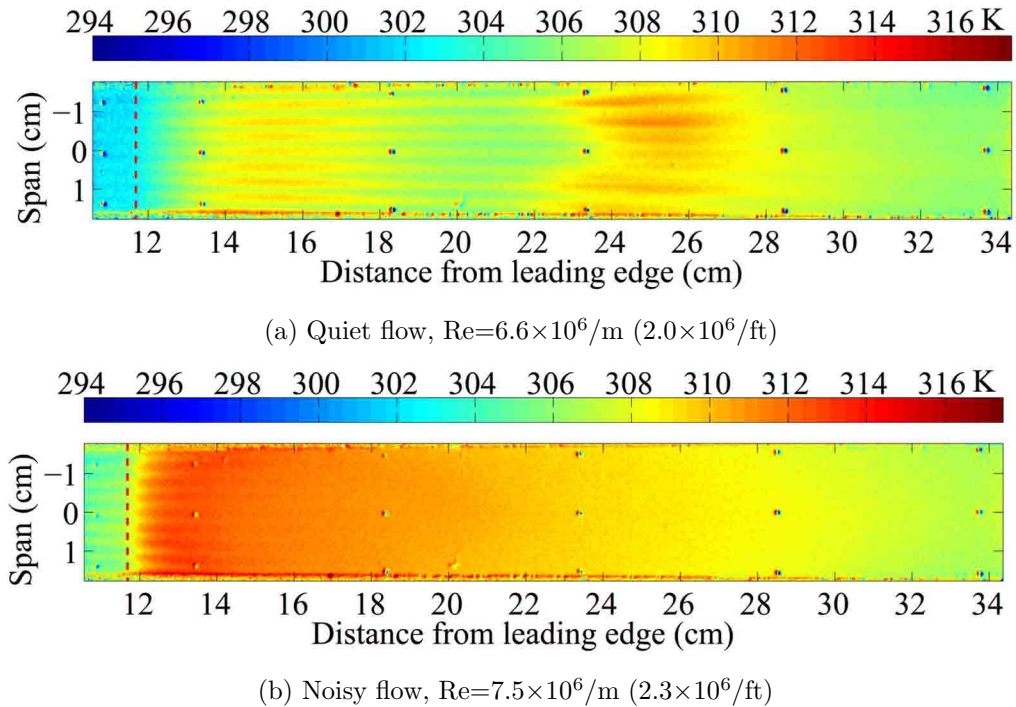


Figure 4.6: Surface temperature (K) distribution with  $k_{max}=0.76$  mm ramp trips under quiet and noisy conditions

The significant difference between quiet and noisy flow is immediately evident from the images. Along the centerline for the quiet case, the temperature increases by about 6 K ( $11^\circ R$ ) from the compression corner to  $x=15.2$  cm (6 in.). This is significantly higher heating than for the smooth insert case shown in Figure 4.4, which increased by only about 1 K ( $2^\circ R$ ) downstream of the corner. This region of high heating is followed by a decrease in temperature from  $x=15.5$  cm (6.1 in.) to  $x=21.6$  cm (8.5 in.). At this point, the temperature increases sharply to a second peak at  $x=25.7$  cm (10.1 in.) followed by a gradual decrease to the end of the model.

It seems likely that the first temperature rise is due to the combination of compression heating as well as heating due to the laminar vortices near the model surface that are shed from the trip elements. The streamwise vortices capture high-momentum

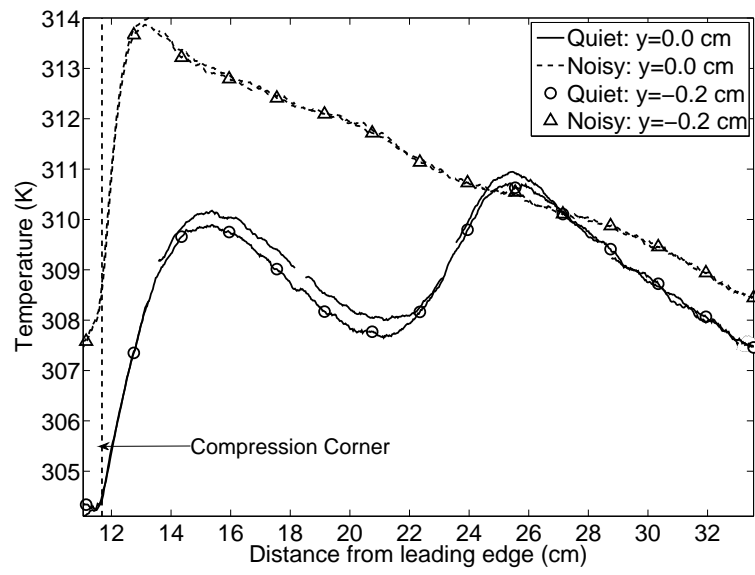


Figure 4.7: Streamwise temperature for centerline and  $y=-0.2$  cm (-0.08 in.) for ramp trips, quiet and noisy flow

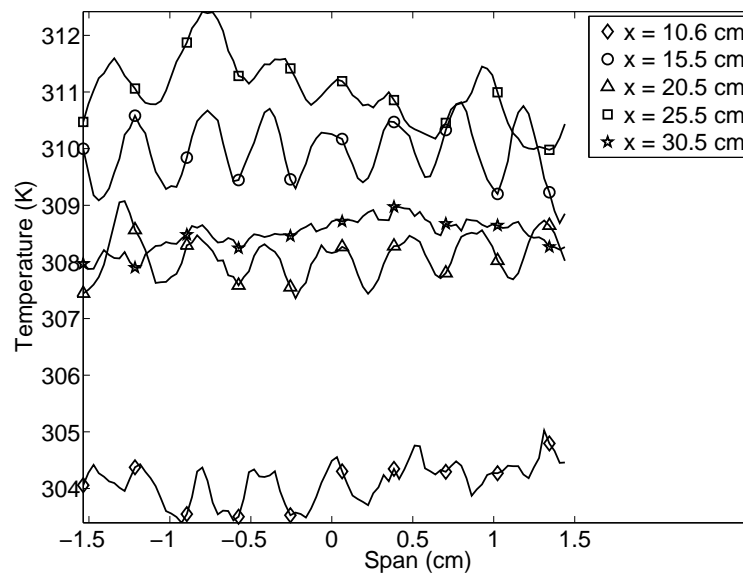


Figure 4.8: Spanwise temperature at several streamwise locations for quiet flow



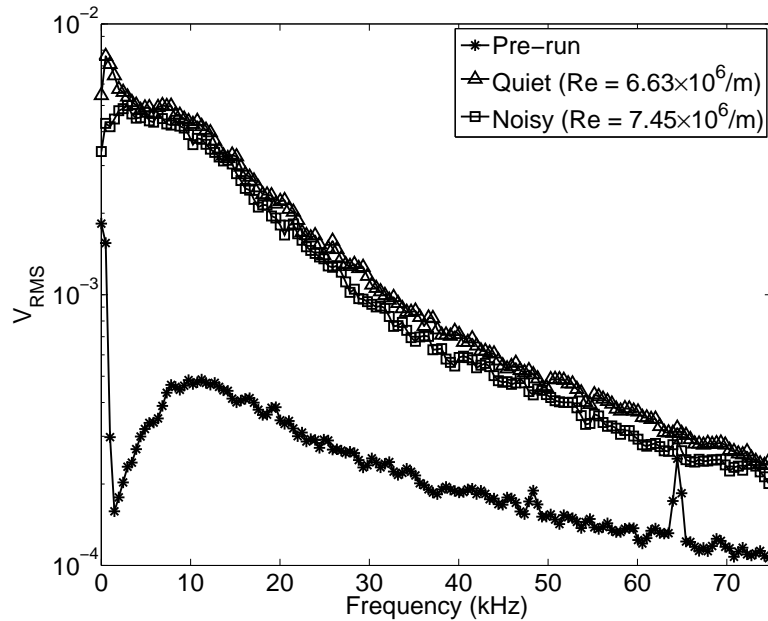


Figure 4.9: Hot-film spectra for quiet and noisy flow,  $k_{max}=0.76$  mm ramp trips

fluid from the freestream and cause it to impinge on the model surface, elevating the temperature there. The streamwise streaks in Figure 4.6a are most likely due to these vortices. In Figure 4.7, the centerline streamwise temperature is along a peak in spanwise temperature of Figure 4.8. The streamwise temperature along  $x=-0.2$  cm is along a trough in the spanwise distribution. The maximum difference between peak and trough temperatures is only about 1 K ( $2^{\circ}\text{R}$ ) under quiet conditions with almost no difference under conventional freestream noise levels.

The streamwise temperature decrease after the first peak is attributed to the thickening laminar boundary layer. The second temperature increase, starting at around  $x=21.6$  cm (8.5 in.), is thought to be due to the onset of transition. Schneider [71] states that the maximum surface temperature generally corresponds to the middle of transition. Thus, at  $x=26.7$  cm (10.5 in.), it seems that the boundary layer is well on its way to being fully turbulent with the subsequent temperature decrease due to the thickening turbulent boundary layer.

Under conventional noise levels, this type of behavior is not seen. Rather, there is a sharp rise in temperature at the corner,  $x=11.7$  cm, (4.6 in.) to  $x=14.0$  cm (5.5 in.). This high-temperature peak is then followed by a nearly monotonic decrease to the end of the model. The sudden rise in surface temperature and subsequent decrease suggests that the boundary layer transitions just downstream of the corner. The hot-film spectra in Figure 4.9 support the contention that the windward boundary layer has transitioned at the hot film ( $x=26.7$  cm, 10.5 in.) under both quiet and noisy flow. The spectra lie almost on top of each other and show high power levels at the lower frequencies.

The spanwise temperatures at streamwise stations of  $x=10.6$ , 15.5, 20.5, 25.5, and 30.5 cm (4.1, 6.1 8.1, 10.0, 12.0 in.) in Figure 4.8 clearly reflect the temperature behavior shown in Figure 4.7. The oscillations seen at  $x=15.5$ , 20.5, and 25.5 cm (6.1, 8.1, and 10.0 in.) are no longer visible by  $x=30.5$  cm (12.0 in.). Over most of the ramp, there is little axial growth of the oscillations. Rather, they seem to saturate and then break down. This is further indication of a turbulent boundary layer on the aft portion of the model.

As previously discussed, in order to determine if the conclusions drawn from the TSP data were correct, a hot wire was to be placed in the boundary layer at several streamwise locations. At this time, the maximum stagnation pressure providing quiet flow had dropped from 655 kPa (95 psia) to 552 kPa (80 psia). Figure 4.10 shows the windward temperature distribution at  $Re=5.9\times 10^6/m$  ( $1.8\times 10^6/ft$ ) for the ramp-roughness trip at the reduced maximum quiet pressure used for the hot-wire measurements. Figure 4.11 shows the centerline temperature. Here,  $T_0=427$  K (769°R) and  $P_0=538$  kPa (78 psia). In Figures 4.10 and 4.11, the solid lines mark the streamwise locations of the hot wire measurements. The dashed lines show the corner location. Qualitatively, the temperature behaves very similarly to what was seen in Figures 4.6a and 4.7. There is an initial temperature rise downstream of the corner followed by a decrease, a sharp rise, and then a steady decrease to the end of the model. Because of the qualitative similarities, it was decided to proceed with

the hot wire measurements to determine the state of the boundary layer. The results were then extrapolated to the TSP images at the slightly higher Reynolds numbers used earlier.

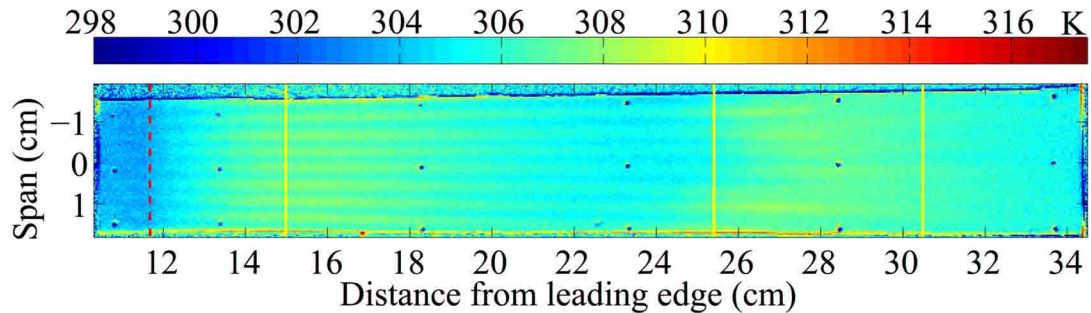


Figure 4.10: Surface temperature for  $Re=5.9 \times 10^6/m$  ( $1.8 \times 10^6/ft$ ), quiet flow, ramp trips

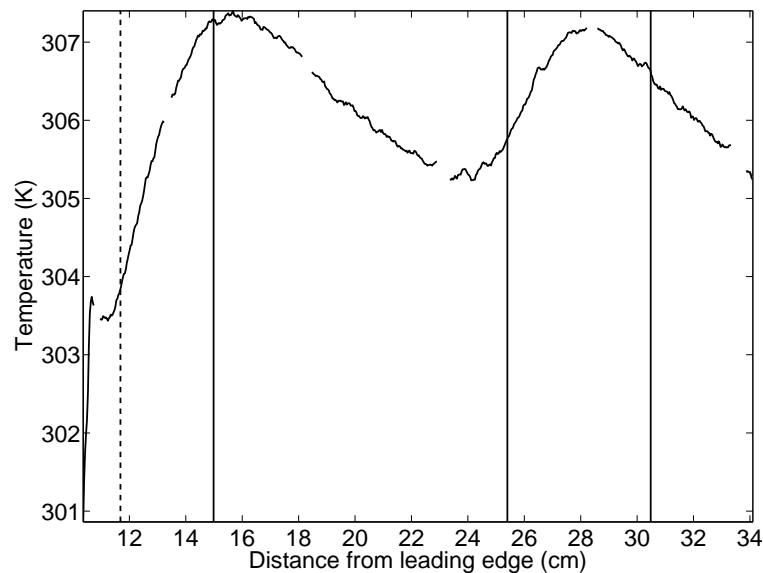


Figure 4.11: Centerline temperature for  $Re=5.9 \times 10^6/m$  ( $1.8 \times 10^6/ft$ ), quiet flow, ramp trips

In order to accurately determine the state of the boundary layer, runs with the hot wire positioned at  $x=15.0$ ,  $25.4$ , and  $30.5$  cm (5.9, 10.0, and 12.0 in.) were first made

with the hot wire traversing through the boundary layer in order to determine its thickness. The same uncalibrated hot wire was used for all three runs. It was hoped that after uncalibrated runs were made, the experiments could be repeated with calibrated wires. Facility and probe difficulties precluded calibrated experiments of the same type. The wire's typical square-wave frequency response was about 240 kHz. The overheat ratio based on resistances was about 1.8, making it most sensitive to mass-flux. The hot wire was a Platinum/10% Rhodium (Pt/Rh) wire with a diameter of 0.00038 cm (0.00015 in.) and a length/diameter ratio of about 107. The data were always sampled at 2 million samples per second.

Generally, the hot wire began the run at 0.7 or 0.9 mm (0.03 or 0.04 in.) from the model surface. Over the course of about 6 seconds, it moved away from the model in 0.1 mm (0.004 in.) increments, stopping at each location for 200 ms. The distance from the wall at each step was then plotted against the average CTA bridge voltage. From this plot, Figure 4.12, the approximate boundary layer thickness was deduced.

Over the course of a typical run, the Reynolds number dropped by about 35%. This means that by the end of the run, when the points furthest away from the model were recorded, the boundary layer was considerably thicker than at the beginning of the run. The hot-wire spectra were to be computed for data at around  $t=0.6$  s, where  $t$  is time from tunnel startup. The boundary layer edge was not usually crossed until about  $t=4.5$  s. Thus, a scaling procedure was used to approximate the boundary layer thickness at  $t=0.6$  s given a measured thickness at  $t=4.5$  s. This scaling assumes that transition did not move over the streamwise station of interest while the probe was traversing the boundary layer. It also assumes that the thickness is proportional to the inverse square root of the Reynolds number. The approximate boundary layer thickness at  $t=0.6$  s can be determined from the thickness measured at  $t=4.5$  s through the following relation:

$$\frac{\delta(t = 0.6)}{\delta(t = 4.5)} \approx \sqrt{\frac{Re(t = 4.5)}{Re(t = 0.6)}} \approx \sqrt{\frac{p(t = 4.5)}{p(t = 0.6)}}$$

where  $\delta$  is the boundary layer thickness and  $p$  is the stagnation pressure. The value of this ratio is generally around 0.85. A location about 15% less than the experimentally measured edge was usually chosen as the location to place the hot wire. This ensured that the hot wire was inside the boundary layer and near the edge at the time the spectra were computed. Also, it is expected and has been experimentally shown by Rufer [72] in the BAM6QT that the amplitude of second mode instability waves is greatest near the boundary layer edge. Thus, if second mode waves were present, it was thought that they would be visible in the hot-wire spectra.

Figure 4.12 shows the results of the boundary-layer profile runs for streamwise locations of  $x=11.4$ , 15.0, 25.4, and 30.5 cm (4.5, 5.9, 10.0, and 12.0 in.). The gaps in the boundary layer profiles are because of a lack of data due to nozzle-wall boundary layer separation. Ideally, boundary layer profiles would have been measured for these streamwise stations for both trip strips. However, due to probe difficulties, tunnel difficulties, and time constraints, profiles were measured for the ramp trips at only the three downstream locations and for the diamond trips for the  $x=11.4$  cm (4.5 in.) case.

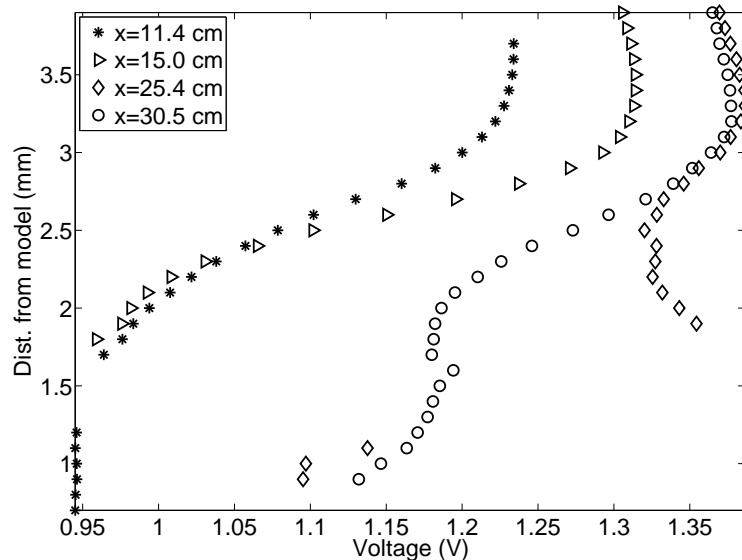


Figure 4.12: Boundary layer profiles

It is not a simple matter to obtain a value for the boundary layer edge location. As can be seen, the voltage gradually approaches a peak value and then generally decreases again. An approximate value for the edge location is all that could be obtained. The boundary-layer thickness measured with the ramp trips was used as an approximate value for the diamond roughness cases. Table 4.2 summarizes the approximate experimental boundary-layer thicknesses for the various streamwise locations. It was at first surprising to find that the boundary layer was thicker at upstream locations than for locations farther downstream. Given the unique nature of the flow, however, this is not too difficult to explain. The flow at these locations is downstream of large roughness elements. In addition, it seems likely that there is a separation bubble at the compression corner. The effects and extent of such a separation, upstream and downstream, are not fully understood. Boundary layer separations in hypersonic flow have been shown to extend up to 100 boundary layer thicknesses upstream of the initial cause of the separation [73]. It may also be that downstream of the reattachment point it takes a considerable distance for the boundary layer to fully process the effects of the separation. Also, it is clear from the vortices in the TSP images that there is some outward-directed crossflow. This thins the centerline boundary layer.

Table 4.2: Boundary layer thickness

$x$ (cm)	Trip	$\delta$ (mm)
11.4	Diamonds	3.5
15.0	Ramps	3.4
25.4	Ramps	3.3
30.5	Ramps	3.3

Figure 4.13 shows the power spectra at  $Re \approx 5.9 \times 10^6/m$  ( $1.8 \times 10^6/ft$ ) for stream-wise hot wire locations of  $x=15.0$ , 25.4, and 30.5 cm (5.9, 10.0, and 12.0 in.) as well as spectra computed for the  $x=25.4$  cm (10.0 in.) pre-run signal. Hot wire locations

were chosen to be near the boundary layer edge, where disturbances were expected to have the largest amplitudes. Thus, the corresponding distances above the model surface for the hot wire were 2.7, 3.0, and 3.0 mm (0.11, 0.12, and 0.12 in.), respectively. The spectra were computed over a 200 ms interval that included no turbulent bursts in the nozzle wall boundary layer. Each spectrum was computed from a 200 ms signal and is the average of 100 fast Fourier transforms (FFTs), with each FFT computed from 4000 data points. Welch’s averaged, modified periodogram method with a Hamming window was used.

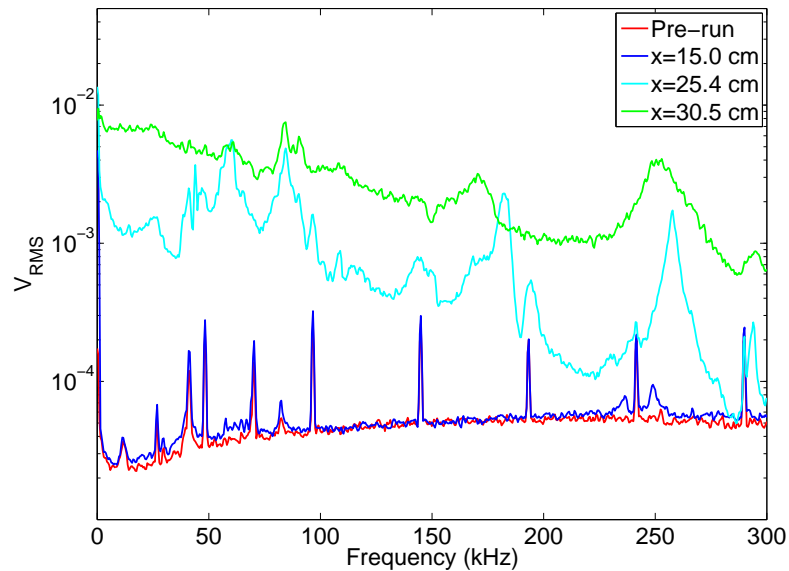


Figure 4.13: Hot wire spectra for ramp roughness

If the spectra were taken over a time period that included a turbulent burst, particularly when the model boundary layer was fully laminar, there was a huge effect in the spectrum. The power levels were much more erratic and higher in magnitude. This effect is demonstrated in Figure 4.14. Here, spectra of the hot wire signal at  $x=15.0$  cm (5.9 in.) were calculated for slightly different portions of the signal. For  $6.69 < t < 6.89$  s, there were no turbulent bursts in the nozzle-wall boundary layer. For  $6.68 < t < 6.88$  s, a shift of only 10 ms, there was one turbulent burst. As can be

seen, for  $6.69 < t < 6.89$  s, the spectrum falls nearly on top of the pre-run signal. For  $6.68 < t < 6.88$  s, when there was one turbulent burst, the spectrum is more erratic and has higher power. In order to compute the spectra for no turbulent bursts in the nozzle-wall boundary layer, the spectra when the hot wire was located at  $x=25.4$  cm (10.0 in.) was only taken for a signal 136 ms long.

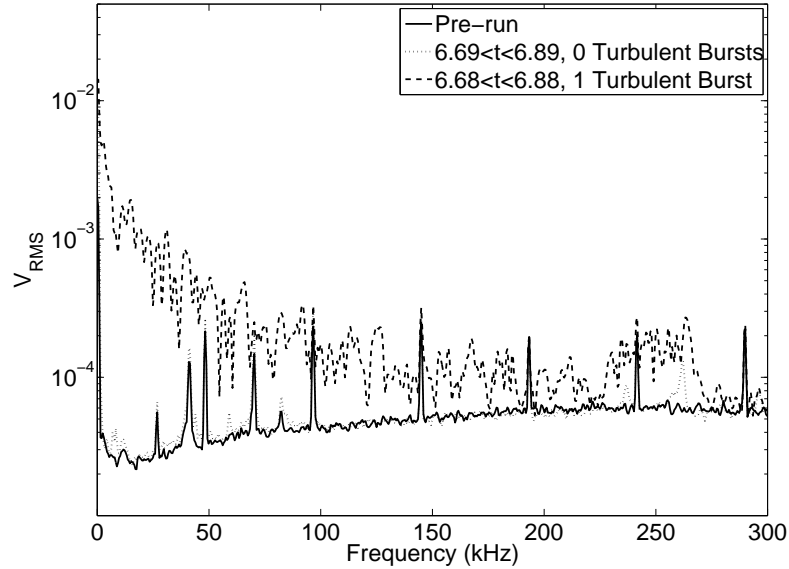


Figure 4.14: Hot wire spectra for signals with 0 and 1 turbulent burst

As can be seen in Figure 4.13, the spectrum when the hot wire was located very near the first local peak in the centerline temperature, at  $x=15.0$  cm (5.9 in.), falls nearly on top of the pre-run spectrum. This indicates that there are very few disturbances in the boundary layer at that location and that it is laminar, as was previously suspected from the TSP data. The spectrum for  $x=25.4$  cm (10.0 in.) is very different from that at  $x=15.0$  cm (5.9 in.). The location  $x=25.4$  cm (10.0 in.) is just downstream of where the centerline temperature began to increase for the second time. It was suspected that this location was near the midpoint of transition. The spectrum supports this notion. The power levels, especially for the lower frequencies, are orders of magnitude higher than the pre-run and  $x=15.0$  cm (5.9 in.) spectra.



It appears that the boundary layer at  $x=25.4$  cm (10.0 in.) may not be completely turbulent, but there are significant disturbances present at that location. The spectrum at  $x=30.5$  cm (12.0 in.), where it was suspected that the boundary layer had become fully turbulent, shows power levels generally at least a factor of two greater than for the  $x=25.4$  cm (10.0 in.) case. These high levels of broadband noise are due to a turbulent boundary layer at  $x=30.5$  cm (12.0 in.).

Because the hot wire and TSP data agree about the state of the boundary layer at the reduced quiet pressure, conclusions can be drawn from the TSP images at higher pressure even though there are no supporting hot-wire measurements. From Figure 4.7, transition onset is taken to be at about  $x=21.0$  cm (8.25 in.) under quiet conditions at  $P_0=586$  kPa (85 psia). This is where the streamwise temperature ceases its nearly monotonic decrease and begins to increase again. There should be no other mechanisms that would cause the surface temperature there to increase. Transition occurs immediately downstream of the compression corner under noisy conditions. Reducing freestream noise levels from conventional to quiet levels caused the transition Reynolds number based on distance from the nose to increase by a factor of 1.6 from  $0.9 \times 10^6$  to  $1.4 \times 10^6$ . The transition Reynolds number based on distance from the strip increases by a factor of 2.4 from  $0.4 \times 10^6$  to  $1.0 \times 10^6$ . Based on distance from the corner, the transition Reynolds number increases from 0 to  $0.7 \times 10^6$ . Under the reduced quiet pressure conditions, transition was taken to be at  $x=24.1$  cm (9.5 in.). For the three different length parameters, this gave transition Reynolds numbers 1.4, 1.1, and  $0.8 \times 10^6$ , respectively. The results are summarized in Table 4.3.

This large effect of freestream noise levels on transition is not altogether surprising. The wake behind large roughness elements is often unstable. When freestream noise levels are elevated, increased disturbance levels can be introduced into the unstable wake via a receptivity process. The growth of wake instabilities thus starts at a higher level which can then lead to earlier breakdown and transition of the boundary layer [74].

Table 4.3: Transition Reynolds numbers with  $k_{max}=0.76$  mm (0.030 in.) ramp trips

Length Parameter	Re <sub>t</sub>		Increase
	Noisy	Quiet	
Nose	$0.9 \times 10^6$	$1.4 \times 10^6$	1.6
Trips	$0.4 \times 10^6$	$1.0 \times 10^6$	2.4
Corner	$0.0 \times 10^6$	$0.7 \times 10^6$	–

### 4.2.3 Ramp Roughness Insert: 0.38-mm Maximum Height

As previously mentioned, the sizing of boundary layer trips is a tradeoff. The trips must be as small as possible to reduce drag, but large enough to ensure a fully turbulent boundary layer at the engine inlet under the low freestream noise levels of flight. In addition to the  $k_{max}=0.76$  mm (0.030 in.), ramp trips with  $k_{max}=0.38$  mm (0.015 in.) were also tested. Since the hot-wire measurements for the larger trips supported the TSP data, hot wire measurements were not made with the smaller trips. Instead, in order to further characterize the effect of freestream noise on transition induced by the trips, a Reynolds number sweep with both quiet and conventional noise levels was conducted and surface temperatures were measured. Experiments were conducted at freestream Reynolds numbers of 7.6, 9.0, 10.1, and  $11.3 \times 10^6/\text{m}$  (2.3, 2.7, 3.1, and  $3.5 \times 10^6/\text{ft}$ ) with conventional freestream noise levels and 7.0, 8.2, 9.3, and  $10.3 \times 10^6/\text{m}$  (2.1, 2.5, 2.8, and  $3.1 \times 10^6/\text{ft}$ ) with low noise levels. Figure 4.15 shows the surface temperatures from these measurements. Figure 4.16 shows the centerline streamwise temperature distributions for all these cases.

The effect of Reynolds number is immediately apparent. Under noisy conditions, a clear transition front is seen to move upstream as Reynolds number increases. However, under low freestream noise levels, no transition front is seen for  $\text{Re}=7.0 \times 10^6/\text{m}$  ( $2.1 \times 10^6/\text{ft}$ ). Likewise, no transition front is seen for  $\text{Re}=8.2 \times 10^6/\text{m}$  ( $2.5 \times 10^6/\text{ft}$ ). As the Reynolds number is further increased to  $9.3 \times 10^6/\text{m}$  ( $2.8 \times 10^6/\text{ft}$ ), the quali-

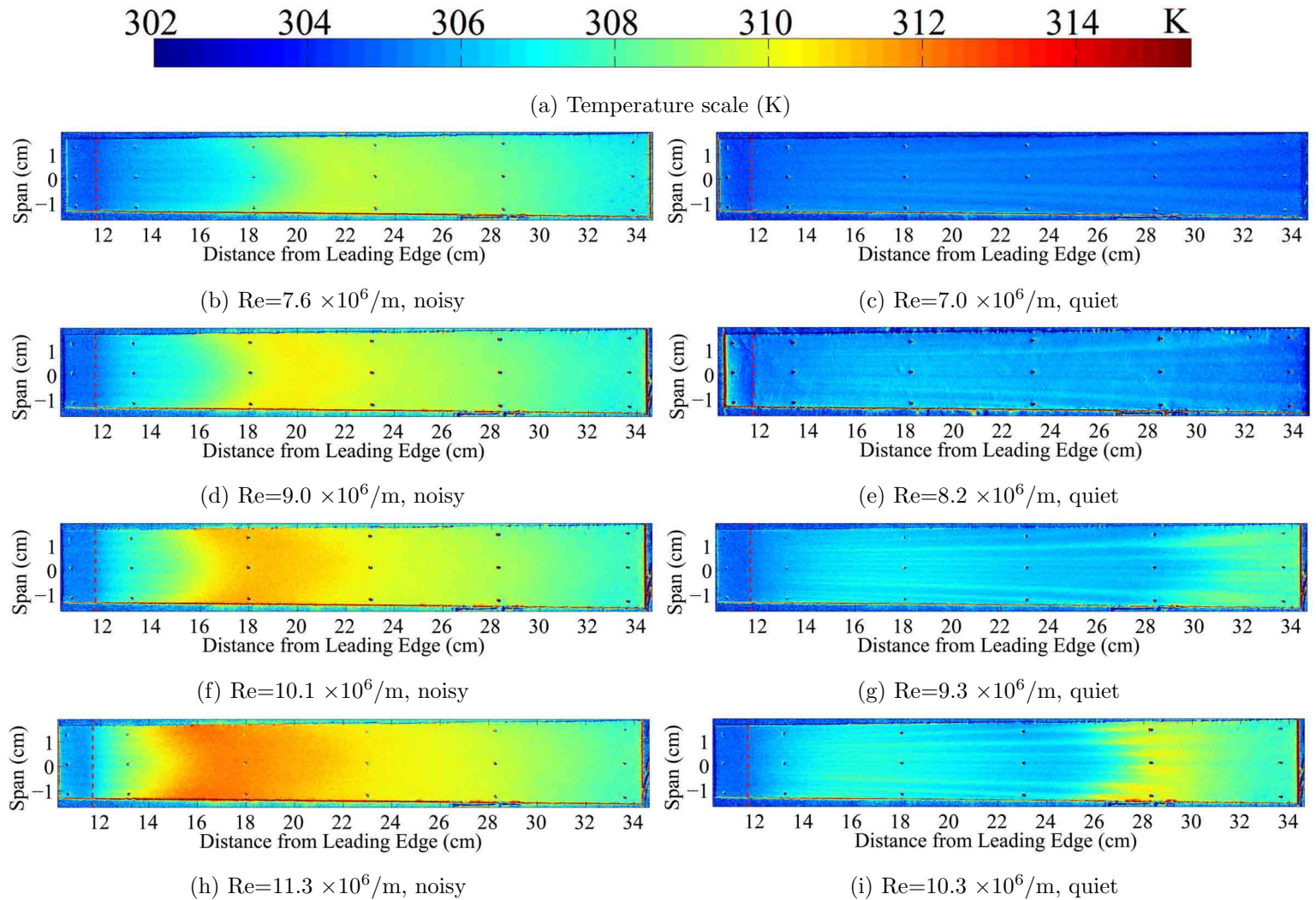


Figure 4.15: Surface temperature (K) distribution under quiet and noisy conditions,  $k_{max}=0.38$  mm (0.015 in.)

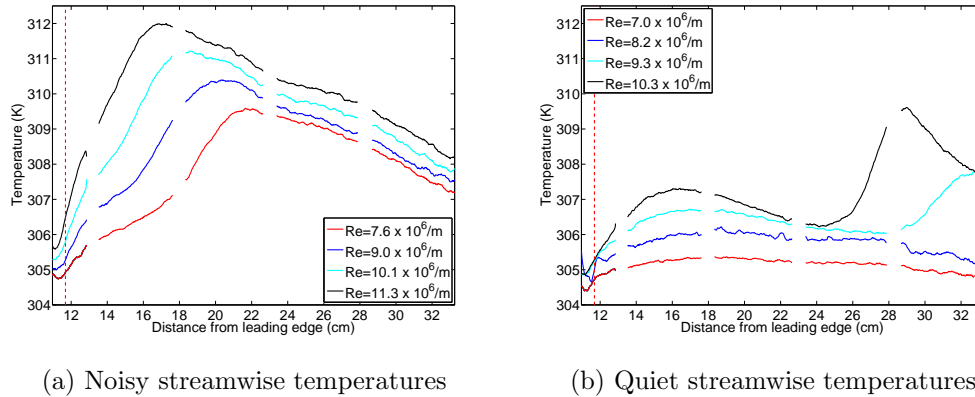


Figure 4.16: Streamwise temperature (K) under quiet and noisy conditions,  $k_{max}=0.38$  mm (0.015 in.)

tative nature of the surface temperature becomes similar to that observed with the larger,  $k_{max}=0.76$  mm (0.030 in.) ramp trips. Downstream of the compression corner, there is a higher temperature region caused by laminar vortex heating. Downstream of this, the temperature drops due to a thickening laminar boundary layer. Between  $x = 28$  and 30 cm (11 and 12 in.), a transition front is seen. For  $Re=10.3 \times 10^6/m$  ( $3.1 \times 10^6/ft$ ), the laminar vortex temperature increase is greater and the transition front moves upstream compared to the  $Re=9.3 \times 10^6/m$  ( $2.8 \times 10^6/ft$ ). Figure 4.16 also shows these trends.

Again, the effect of freestream noise on roughness induced transition is apparent. Reducing freestream noise levels from conventional to quiet levels significantly increased the transition Reynolds number. These results are summarized in Table 4.4. Here,  $Re_t$  is defined using freestream conditions and length from the trip strip. At the highest freestream Reynolds number that was tested, reducing the freestream noise levels increased  $Re_t$  by a factor of 3.1.

There were only two sets of tunnel conditions that were the same for both the  $k_{max}=0.76$  mm (0.030 in.) and  $k_{max}=0.38$  mm (0.015-in.) ramp trips. They were for a freestream Reynolds number of about  $7.6 \times 10^6/m$  ( $2.3 \times 10^6/ft$ ) noisy and about  $7.0 \times 10^6/m$  ( $2.1 \times 10^6/ft$ ) quiet. At these freestream conditions for the  $k_{max}=0.38$  mm

Table 4.4: Transition Reynolds numbers with  $k_{max}=0.38$  mm (0.015 in.) ramp trips

Re (million/m)		$X_t$ (cm) from Trips		Re <sub>t</sub> (million)		Increase
Noisy	Quiet	Noisy	Quiet	Noisy	Quiet	
7.6	7.0	10.7	>28.2	0.8	>2.0	>2.4
9.0	8.2	9.1	>28.2	0.8	>2.3	>2.8
10.10	9.3	8.1	21.6	0.8	2.0	2.5
11.32	10.3	5.3	18.3	0.6	1.9	3.1

(0.015-in.) ramps, transition was delayed by a factor of  $>2.4$  when freestream noise was reduced from conventional to low levels. Since transition was beyond the back of the model at this Reynolds number, it is not possible to quantify the actual factor of transition delay. For the  $k_{max}=0.76$  mm (0.030 in.) ramps, transition was delayed by a factor of 2.4 when freestream noise levels were reduced. With the  $k_{max}=0.38$  mm (0.015 in.) ramps and low noise levels, transition was not observed on the model until the freestream Reynolds number was increased by about 30%. Thus, it can be inferred that for the  $k_{max}=0.38$  mm (0.015 in.) ramp trips, Re<sub>t</sub> was increased by a factor significantly greater than 2.4 when freestream noise was reduced from conventional to quiet levels. Additionally, even at the highest achievable quiet freestream Reynolds number,  $10.3 \times 10^6/\text{m}$  ( $3.1 \times 10^6/\text{ft}$ ), transition with the  $k_{max}=0.38$  mm (0.015 in.) ramps was still 3.6 cm (1.4 in.) downstream of where it occurred for the  $k_{max}=0.76$  mm (0.030 in.) ramps at a 35% lower freestream Reynolds number. Thus, as expected, the larger ramp trips were more effective at tripping the boundary layer, even under low freestream noise levels.

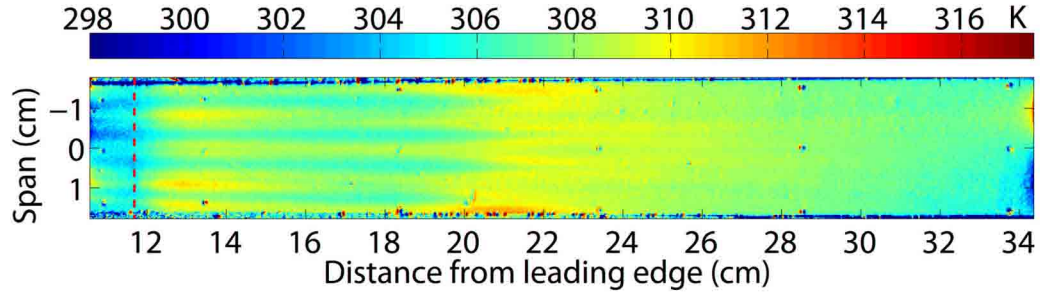
These results underscore the necessity for measurements in quiet facilities. If, for instance, the boundary layer trips were sized based on the measurements made with conventional noise levels at  $\text{Re}=7.6 \times 10^6/\text{m}$  ( $2.3 \times 10^6/\text{ft}$ ), one might reasonably conclude that the  $k_{max}=0.38$  mm (0.015 in.) ramps are sufficient to ensure transition on the windward surface. However, when run with flight-like noise levels, these trips

proved to be ineffective at inducing transition anywhere upstream of the engine inlet. Thus, the trips that were sized based on experiments with conventional noise levels might not actually trip the boundary layer. Of course, if the flight Reynolds number were significantly higher than that tested in the quiet tunnel, even the smaller trips could prove to be fully effective. A method for reliably scaling and translating quiet and conventional tunnel measurements into flight conditions should be developed. This could help remove the ambiguity of boundary layer trip sizing.

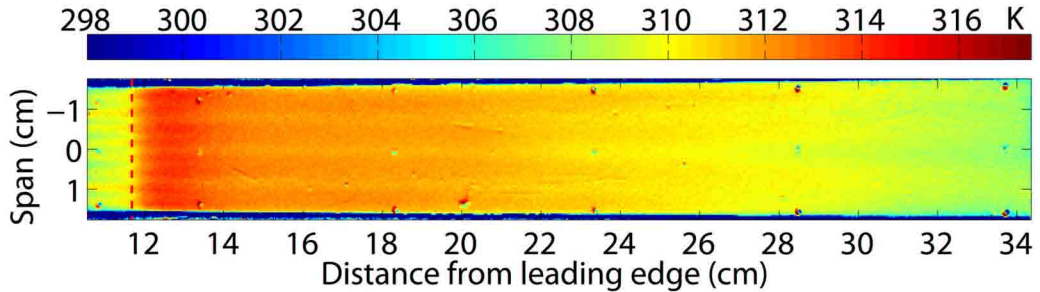
#### 4.2.4 Diamond Roughness Insert

A similar set of experiments was carried out with the diamond trips in the model. Figure 4.17 shows the surface temperature distribution with the diamond roughness strip under quiet and noisy conditions for  $6.73$  and  $7.35 \times 10^6/\text{m}$  ( $2.05$  and  $2.24 \times 10^6/\text{ft}$ ), respectively. For the quiet case,  $T_0=422$  K ( $760^\circ\text{R}$ ) and  $P_0=607$  kPa ( $88$  psia). For the noisy case,  $T_0=424$  K ( $763^\circ\text{R}$ ) and  $P_0=614$  kPa ( $89$  psia). Figure 4.18 shows the streamwise centerline temperature for both cases as well as the streamwise temperature along  $y=-0.4$  cm ( $-0.16$  in.), a trough in the spanwise temperature. Figure 4.19 shows spanwise temperatures at several streamwise stations under quiet flow. Figure 4.20 shows the spectra of the surface hot-film signal.

As the figures show, the surface temperature behaves qualitatively very similarly to the ramp roughness case. Under quiet conditions, just downstream of the compression corner, there is an initial temperature rise. This is followed by a decrease, another sharp rise, and then a gradual reduction of the surface temperature. Additionally, high-temperature streaks are visible from upstream of the corner to the second temperature rise. The locations of the temperature peaks are upstream of the ramp roughness case, however, occurring at  $x=13.7$  and  $21.3$  cm ( $5.4$  and  $8.4$  inches) instead of  $x=15.5$  and  $25.7$  cm ( $6.1$  and  $10.1$  inches), respectively, indicating that the diamond roughnesses are more effective at tripping the boundary layer.



(a) Surface temperature for diamond trips, quiet flow,  $Re=6.7 \times 10^6/m$  ( $2.1 \times 10^6/ft$ )



(b) Surface temperature for diamond trips, noisy flow,  $Re=7.4 \times 10^6/m$  ( $2.2 \times 10^6/ft$ )

Figure 4.17: Surface temperature (K) with diamond trips under quiet and noisy conditions

The spanwise temperatures at streamwise stations of  $x=10.6$ ,  $15.5$ ,  $20.5$ ,  $25.5$ , and  $30.5$  cm ( $4.1$ ,  $6.1$ ,  $8.1$ ,  $10.0$ ,  $12.0$  in.) in Figure 4.19 clearly reflect the temperature behavior shown in Figures 4.18 and 4.17a. The mean temperature of the spanwise plots increases and decreases in a similar fashion to what is seen along the model centerline. Additionally, the spanwise oscillations are easily discernable for streamwise locations of  $x=10.6$ ,  $15.5$ , and  $20.5$  cm ( $4.1$ ,  $6.1$ , and  $8.1$  in.). At  $x=25.5$  and  $30.5$  cm ( $10.0$  and  $12.0$  in.), the oscillations are gone and the curve is much smoother. This behavior is present in Figure 4.17a as the streamwise streaks fade toward the aft end of the model.

Due to the qualitative similarities to the ramp roughness case, it was thought that the first temperature rise was again due to compression heating at the corner and the presence of laminar vortices near the model surface. The second peak was again believed to be due to transition. The hot-film spectra support this theory for

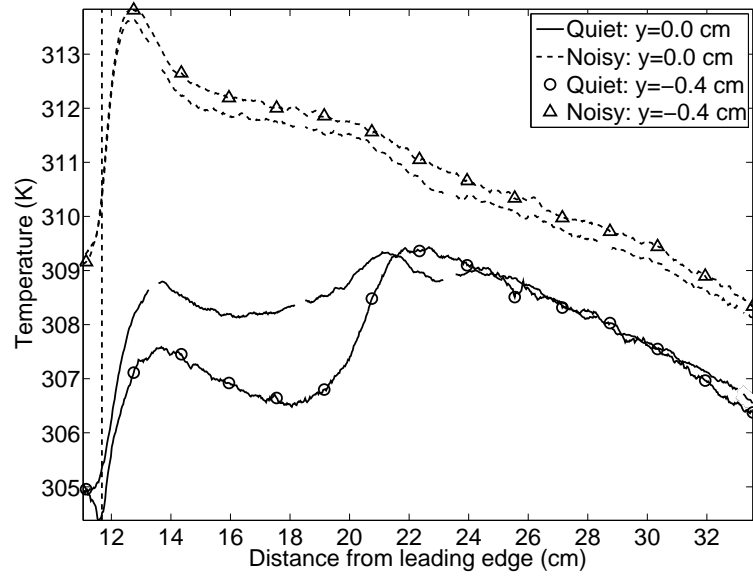


Figure 4.18: Streamwise temperature for centerline and  $y=-0.4$  cm (-0.16 in.) for diamond trips, quiet and noisy flow,  $Re=6.7$  and  $7.4 \times 10^6/m$  ( $2.1$  and  $2.3 \times 10^6/ft$ )

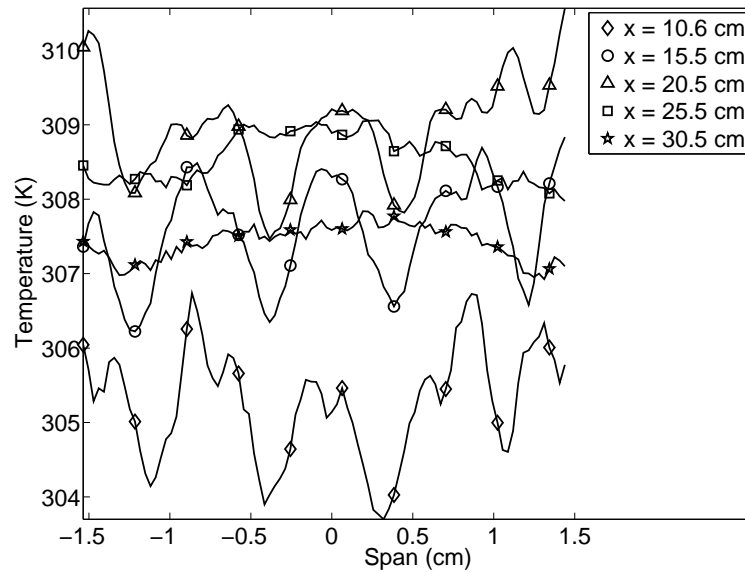


Figure 4.19: Spanwise temperature at various streamwise locations, diamond trips, quiet flow



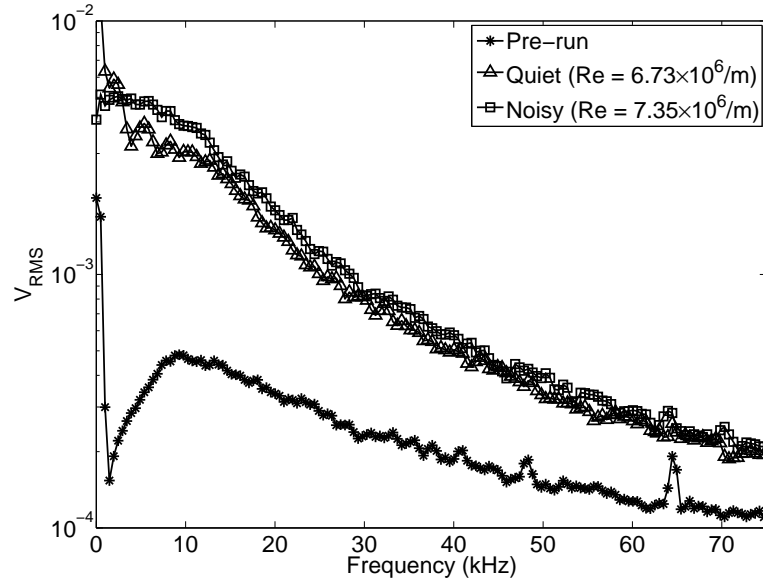


Figure 4.20: Spectra for noisy and quiet flow with diamond trips

the runs at 655 kPa (95 psia) initial stagnation pressure, showing high power levels in the low frequency band.

Again, due to the reduced maximum quiet pressure for the later hot-wire experiments in the BAM6QT, a TSP image was again taken under reduced pressure conditions before checking the boundary layer state with a hot wire. Here,  $Re=5.8 \times 10^6/m$  ( $1.8 \times 10^6/ft$ ),  $T_0=427K$  (769°R), and  $P_0=538$  kPa (78 psia). The surface temperature distribution can be seen in Figure 4.21. The centerline temperature is shown in Figure 4.22. The dashed lines mark the compression corner and the solid lines are the locations at which spectra were measured. A brief comparison shows very similar behavior to that of Figures 4.17a and 4.18, the surface and centerline temperature distributions for quiet flow at 655 kPa (95 psia). The locations of the temperature peaks are moved somewhat downstream from the similar peaks observed at  $Re=6.7 \times 10^6/m$  ( $2.1 \times 10^6/ft$ ), but the qualitative similarities are sufficient reason to believe that the boundary layer behaves in the same way as for the higher Reynolds number case.

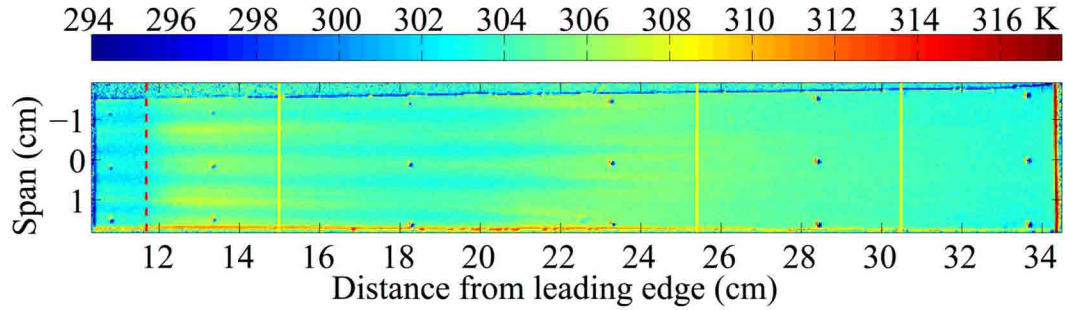


Figure 4.21: Surface temperature for  $Re=5.8 \times 10^6/m$  ( $1.8 \times 10^6/ft$ ), quiet flow, diamond trips

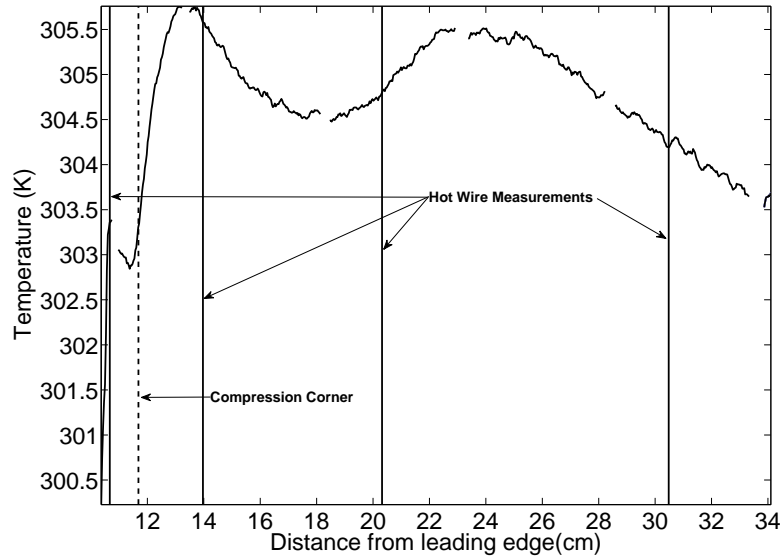


Figure 4.22: Centerline temperature for  $Re=5.8 \times 10^6/m$  ( $1.8 \times 10^6/ft$ ), quiet flow, diamond trips

Figure 4.23 shows hot wire spectra at  $x=10.7$ ,  $14.0$ ,  $20.3$ , and  $30.5$  cm (4.2, 5.5, 8.0, and 12.0 in.) for distances from the surface of 3.0, 2.7, 2.8, and 3.0 mm (0.12, 0.11, 0.11, and 0.12 in.), respectively. The first hot-wire location,  $x=10.7$  cm (4.2 in.), is 1.0 cm (0.4 in.) upstream of the compression corner. A power spectrum was also computed for 200 ms of pre-run data for comparison. Again, the spectra were computed over a 200 ms interval. As much as was possible, they were computed over

a portion of the signal for which the nozzle wall boundary-layer had no turbulent bursts. Each spectrum was the average of 100 fast Fourier transforms (FFTs), with each FFT computed from 4000 data points sampled at  $2 \times 10^6$  samples per second. Welch's averaged, modified periodogram method with a Hamming window was used.

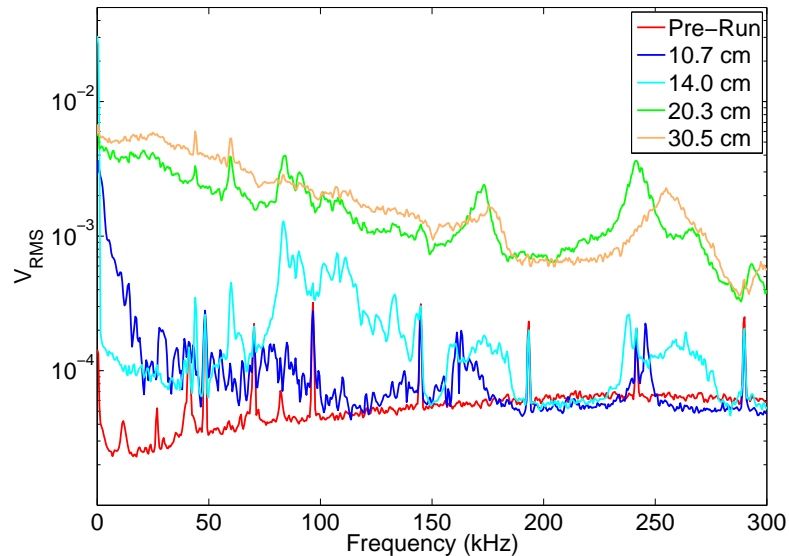


Figure 4.23: Hot wire spectra for diamond roughness

The hot-wire data in Figure 4.23 again support what the TSP images suggest. Due to lower power levels at  $x=10.7$  and  $14.0$  cm (4.2 and 5.5 in.) compared to locations further downstream, it is concluded that the boundary layer is laminar at those locations. However, the power levels are higher and much less smooth than for the ramp roughness insert. The diamond roughnesses have  $k_{max}=0.15$  cm (0.060 in.) high, while the ramps have  $k_{max}=0.76$  mm (0.030 in.). The larger roughness gives rise to greater disturbances in the boundary layer, evidenced by higher and more uneven power levels in the power spectra. The spectra at  $x=20.3$  and  $30.5$  cm (8.0 and 12.0 in.) suggest a turbulent boundary layer. This is somewhat surprising for the  $x=20.3$  cm (8.0 in.) location. From Figure 4.22, this location is just downstream of onset of the second temperature rise. It was thought that this second rise marked the

onset of transition. As such, generally higher power levels were expected, but not to the degree as those that were observed. It is possible that either the larger roughnesses and the resultant large disturbances cause the boundary layer to complete transition over a very short streamwise distance or that the boundary layer has not completely transitioned at  $x=20.3$  cm (8.0 in.). At  $x=20.3$  cm (8.0 in.), the power levels are lower than those at  $x=30.5$  cm (12.0 in.) for most frequencies, signifying that it may not yet be entirely turbulent.

Extrapolating trends back to the higher Reynolds number TSP results, transition onset is observed to occur in Figure 4.18 at  $x=16.6$  cm (6.5 in.) under quiet conditions. This is where the temperature departs from a monotonic decrease and begins to rise. Transition onset explains this change in temperature. Under noisy conditions, a fully turbulent boundary layer is seen just downstream of the corner. Reducing freestream noise levels from conventional to quiet levels caused the transition Reynolds number based on distance from the nose to increase by a factor of 1.3 from 0.86 million to 1.11 million. The transition Reynolds number based on distance from the strip increases by a factor of 1.7 from 0.40 million to 0.69 million. Based on distance from the corner, the transition Reynolds number increases from 0 to 0.39 million. These results are summarized in Table 4.5. Under the reduced quiet pressure conditions, transition was taken to be at  $x=18.3$  cm (7.2 in.). For the three different length parameters, this gave transition Reynolds numbers of 1.1, 0.7, and  $0.5 \times 10^6$ , respectively.

Table 4.5: Transition Reynolds numbers with  $k_{max}=1.5$  mm (0.060 in.) diamond trips

Length Parameter	$Re_t$		Increase
	Noisy	Quiet	
Nose	$0.9 \times 10^6$	$1.1 \times 10^6$	1.3
Trips	$0.4 \times 10^6$	$0.7 \times 10^6$	1.7
Corner	$0.0 \times 10^6$	$0.4 \times 10^6$	–

The increase in transition Reynolds number is not as substantial as that observed with the ramp trips. This result is not surprising, however, given the larger height of the diamond trips and the fact that both the ramp and diamond trips induced transition at the corner under noisy conditions. Thus, the diamond roughness introduces much larger disturbances into the boundary layer and causes earlier transition under quiet conditions.

### 4.3 Streamwise Vortices

Figure 4.3a evinces streamwise vortices along the model surface in the absence of any boundary-layer trips. It would be good to demonstrate that the streamwise vortices with the roughness elements are tied to the trips themselves. For the ramp roughnesses, 8 full roughness elements and 2 half-roughnesses are directly upstream of the nylon insert. Each ramp element is designed to generate a pair of counter-rotating vortices. Thus, with no outward-directed crossflow, 18 streamwise vortices would be expected on the nylon insert. However, there is evidence of outward-directed crossflow in Figure 4.6a. Thus, less than 18 streamwise vortices from the ramp roughness elements would be expected on the nylon insert. There were 5 roughness elements directly upstream of the nylon insert in the case of the diamond roughnesses.

Figure 4.24 shows spanwise temperature distributions for the smooth wall, ramp roughnesses with  $k_{max}=0.76$  mm , and the diamond roughness elements, all with low freestream noise levels. For the smooth wall, the spanwise temperature is shown at  $x=22.0$  cm. This location was chosen because the vortices are the most clear here. For the ramp and diamond roughnesses, the spanwise temperatures are shown at the streamwise location corresponding to the peak laminar temperature,  $x=15.2$  and  $13.7$  cm (6.0 and 5.4 in.) for the ramp and diamond roughnesses, respectively. Here, high-temperature streaks due to streamwise vortices for the smooth wall are somewhat ambiguous. There are, perhaps, three temperature peaks evident in the spanwise temperature. This indicates that there may be up to 6 vortices present on

the model's nylon strip for the smooth wall. These are likely Görtler vortices due to a separation bubble and subsequent reattachment near the corner, as discussed above. For the ramp roughness, 7 distinct spanwise temperature peaks are clear, with a possible eighth peak at  $y=1.5$  cm (0.6 in.). The peaks suggest the presence of up to 15 streamwise vortices, near the expected value if some outward-directed crossflow is taken into account. There are three clear spanwise peaks and possibly two more at the spanwise extrema for the diamond trips, suggesting up to 8 streamwise vortices there. Although it is hard to conclude a one-to-one correspondence between the number of roughness elements and the number of vortices, there is a clear trend; as the number of roughness elements increases, so too does the number of streamwise vortices.

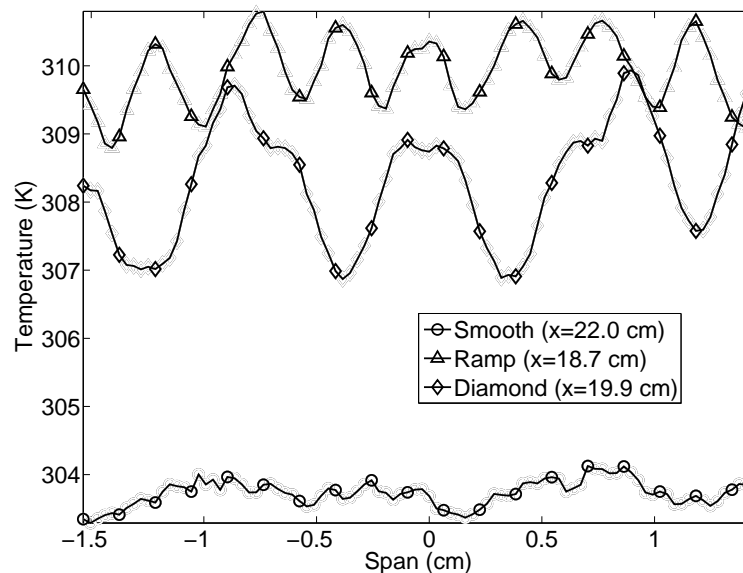


Figure 4.24: Spanwise temperature showing streamwise vortices for 3 trip configurations

It could also be instructive to examine the effect of freestream Reynolds number on the number of vortices. Figure 4.25 shows the spanwise temperature distributions for the  $k_{max}=0.38$  mm ramp roughnesses for freestream Reynolds numbers of 7.6, 9.0, 10.1, and  $11.3 \times 10^6/\text{m}$  ( $2.3$ ,  $2.7$ ,  $3.1$ , and  $3.5 \times 10^6/\text{ft}$ ). The same

streamwise station was used for each Reynolds number,  $x = 16.4$  cm (6.5 in.). For  $Re = 7.6 \times 10^6/m$  ( $2.3 \times 10^6/ft$ ), there are, perhaps, 6-7 discernible temperature peaks. For  $Re = 9.0 \times 10^6/m$  ( $2.7 \times 10^6/ft$ ), the number of discernible streaks increases to, perhaps 8-10. As  $Re$  is further increased to  $10.1 \times 10^6/m$  ( $3.1 \times 10^6/ft$ ), 13 temperature peaks are evident with possibly 2 additional peaks at the edges of the nylon. For  $Re = 11.3 \times 10^6/m$  ( $3.5 \times 10^6/ft$ ), 13 peaks are clear, again with possibly 2 additional peaks at the edges of the nylon.

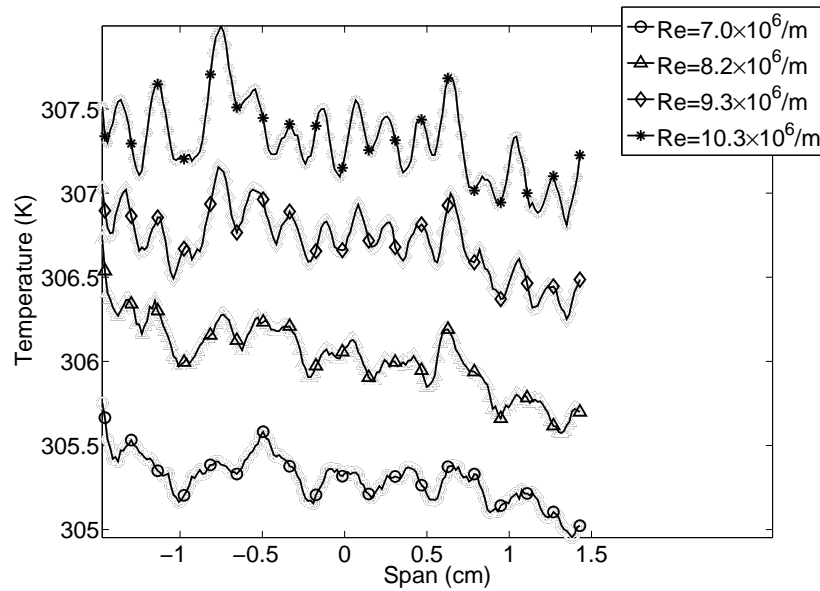


Figure 4.25: Spanwise temperature showing streamwise vortices for  $k_{max} = 0.38$  mm ramp roughness at various Reynolds numbers

It does not appear that the number of temperature peaks scales with Reynolds number. However, when  $Re$  is increased from 8.2 to  $9.3 \times 10^6/m$  ( $3.1$  and  $3.5 \times 10^6/ft$ ), the number of peaks approximately doubles. As Reynolds number increases from 7.6 to  $9.0 \times 10^6/m$  ( $2.3$  and  $2.7 \times 10^6/ft$ ), some of the peaks present at the lower Reynolds number begin to look like they are splitting. For still higher Reynolds number, two clear temperature peaks emerge from what had been one peak at the lowest Reynolds number. It is unclear whether additional vortices are actually being generated at

higher Reynolds number when the boundary layer is thinner, or if they were always there but their temperature signatures on the surface were coincident, disguising the actual number of vortices.

The streamwise vortices shed from upstream roughness elements are readily apparent in Figures 4.6a and 4.17a. The rate at which they grow with increasing streamwise distance is also of interest.

As shown in Figure 4.26, the spanwise root-mean-square (RMS) temperature can be a useful metric for determining the effect, growth, and breakdown of these streamwise vortices. Here, the rms for the column of spanwise pixels at each streamwise station was calculated. The data were then smoothed using an averaging scheme. The RMS temperature reported at each streamwise station is the average of the RMS computed at that station and the RMS values at the 4 adjacent streamwise stations both upstream and downstream of the target station. Streamwise stations that included registration marks were not included. The gaps in data in Figure 4.26 are due to the presence of registration marks at those stations. The vertical dashed line is again the location of the compression corner. The large spike in the ramp case at about  $x=20$  cm (7.9 in.) is not an actual spike in the spanwise RMS temperature. Rather, it is an abnormality in the temperature image, most likely due to an imperfection on the model surface. The imperfection can be seen in Figure 4.6a at  $x=20$  cm (7.9 in.),  $y=1.2$  cm (0.5 in.).

For both the ramp and diamond cases, the same qualitative pattern of spanwise RMS temperature is observed. There is an initial rise in the spanwise RMS temperature immediately downstream of the compression corner. This is followed by a substantial decrease, a sharp rise, and then a sharp drop. This behavior can, perhaps, be best understood by the growth, decay, and breakdown of streamwise vortices in the flow. The incoming vortices are likely amplified by the compression corner, especially if there is a separated region there. The vortices then decay in the thickening laminar boundary layer for a few centimeters downstream of the corner. Then, from  $x=16-20$  cm (6.3-7.9 in.) for the diamond case and 20-25 cm (7.9-9.8 in.) for the ramp



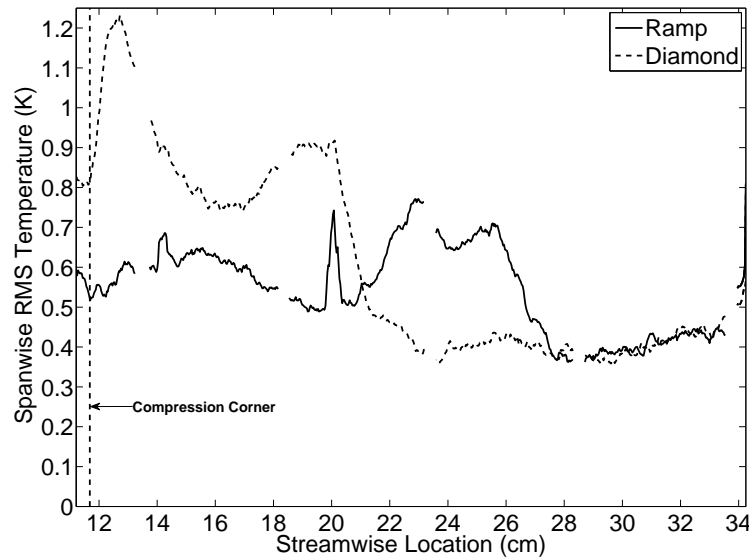


Figure 4.26: Spanwise RMS temperature as a function of streamwise distance for ramp and diamond trips

roughness case, the vortices amplify significantly, increasing the RMS temperature. The sharp drop in RMS temperature is then likely due to breakdown of the vortices into a fully turbulent boundary layer. From  $x=28.0$  to  $34.4$  cm (11.0 to 13.5 in.), the spanwise RMS temperature is nearly the same for both the ramp and diamond cases. This supports the idea that the streamwise vortices have broken down on the aft portion of the model for both cases.

It is also possible that it is only the temperature signature of the vortices at the wall that changes. This does not seem likely, however, since the location of transition changed dramatically from the smooth-wall case to one with trips and among the various trip cases. The trips introduced streamwise vortices into the flow. It is reasonable to assume that they are responsible for the observed changes in transition.

The effect of the larger trip elements is immediately evident in Figure 4.26. In the case of the diamond trips, the amplification at the corner seems to be significantly greater than with the ramp roughnesses, as evidenced by the much larger RMS temperature there. The increase in RMS temperature due to the amplification

of the streamwise vortices begins at  $x=17$  cm (6.7 in.). This is about 4 cm (1.6 in.) upstream of the ramp case, where the RMS begins increasing at about  $x=21$  cm (8.3 in.). The earlier amplification and breakdown of the streamwise vortices for the diamond trips seems to be due to the larger initial strength of the vortices shed from the larger diamond trips.

## 5. LEEWARD MEASUREMENTS

Whereas a turbulent boundary layer was desired on the windward surface of the X-51A, a laminar boundary layer is desired on the leeward side. A turbulent boundary layer there would mean higher viscous drag and surface heating with no benefits. This would necessitate superfluous thermal protection system material, reducing the vehicle's available payload mass. In order to promote more laminar flow for the X-51A and other hypersonic vehicles like it, an understanding of the underlying instability mechanisms leading to transition is desired. A series of experiments were done to determine which instabilities were present on the leeward surface of the X-51A, and the effect of freestream noise on the growth and breakdown of those disturbances.

### 5.1 Temperature Sensitive Paint Measurements

TSP was again used to determine the state of the boundary layer. Figure 5.1 shows surface temperatures for several Reynolds numbers with conventional freestream noise levels. For  $Re=3.2 \times 10^6/m$  ( $1.0 \times 10^6/ft$ ), the surface temperature is nearly uniform. For the higher Reynolds numbers, however, several locations on the leeward nylon insert were found to have elevated temperatures. A region of elevated temperatures symmetric about the model streamwise centerline is observed to broaden and expand in upstream extent with increasing Reynolds number. This broadening and upstream movement is characteristic of a turbulent wedge. The upstream, outboard portions of the nylon also exhibited increased temperatures. An obvious trend with changing Reynolds number was not evident for the outboard regions of elevated temperature, however.

The centerline temperatures corresponding to the surface temperatures in Figure 5.1 are shown in Figure 5.2a. For comparison, the centerline temperatures with



Figure 5.1: Reynolds number sweep of surface temperature distribution with conventional freestream noise

the same freestream conditions but low freestream noise levels are shown in Figure 5.2b. A major difference due to freestream noise levels is immediately evident.

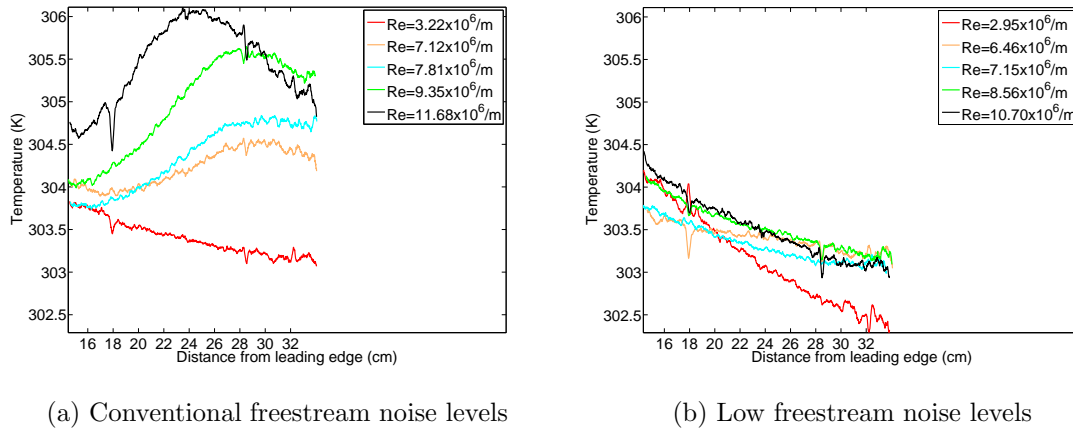


Figure 5.2: Centerline temperatures for conventional and low freestream noise levels

For all Reynolds numbers tested with low freestream noise levels, the model's temperature decreased nearly monotonically to the end of the model. Thus, no surface-temperature images are shown. As on the windward surface, this is evidence of a thickening boundary layer. The temperature decrease alone is not enough to demonstrate the state of the boundary layer. However, when compared to the temperatures with conventional noise levels, it becomes clear that the boundary layers with low noise levels were all laminar. With conventional noise levels, this same monotonic decrease in temperature is seen for  $Re=3.2 \times 10^6/m$  ( $1.0 \times 10^6/ft$ ). For higher Reynolds numbers, however, the temperatures deviate from this pattern. Instead of decreasing monotonically, the temperature increases sharply with downstream distance. With increasing Reynolds number, the maximum temperature increases and the location of maximum temperature moves upstream. Additionally, the location where the centerline temperature begins to increase also moves upstream with increasing Reynolds number, indicating that transition onset moves upstream with increasing Reynolds number. These trends are consistent with boundary layer transition occurring on the leeward nylon insert and moving upstream with increasing Reynolds number.

Preliminary computations using STABL predicted a second-mode  $N$  factor of only about 4.4 at the end of the model for a freestream Reynolds number of  $6.6 \times 10^6/\text{m}$  ( $2.0 \times 10^6/\text{ft}$ ) [75]. For conventional freestream noise levels, transition could possibly be expected at the end of the model. Even so,  $N=4.4$  is on the low side of what is usually expected at transition with conventional noise levels. However, transition was observed far upstream of the end of the model, at around 19 cm for  $\text{Re}=7.1 \times 10^6/\text{m}$  ( $2.2 \times 10^6/\text{ft}$ ), only 55% of the model length. The predicted  $N$  factor here is only about 2.6. Thus, transition under conventional freestream noise levels occurred significantly earlier than would have been normally been expected for transition caused by the growth and breakdown of second-mode waves. However, Horvath et al. [12] reports transition for lower  $N$  factor in quiet facilities run noisy than in tunnels with conventional noise levels. He even observed transition for  $N=2$  in one instance. He speculated that this early transition was due to the high levels of freestream noise possibly inducing nonlinear effects within the various instability modes or even between them. A more in-depth discussion of the computations is in Section 5.5.4.

With low freestream noise levels, transition was not observed, even at a 61% higher Reynolds number of  $10.7 \times 10^6/\text{m}$  ( $3.3 \times 10^6/\text{ft}$ ). This is not unexpected. As previously discussed, transition with low noise levels is typically assumed to occur for  $9 < N < 12$ . Although  $N$  factors have not been computed for  $\text{Re}=10.7 \times 10^6/\text{m}$  ( $3.3 \times 10^6/\text{ft}$ ), it seems unlikely that the maximum  $N$  factor would increase from 4.5 to 9 with a change in freestream Reynolds number of only 61%.

So, although the data with low freestream noise levels were expected, the results with conventional noise levels were surprising. With transition observed for a preliminary  $N$  factor of only 2.6, the assumption that transition was caused by the growth and breakdown of second-mode waves was called into question. In order to better characterize the mechanism/s responsible for early transition with conventional freestream noise levels, a series of experiments was designed and conducted.

## 5.2 Hot-Wire Measurements

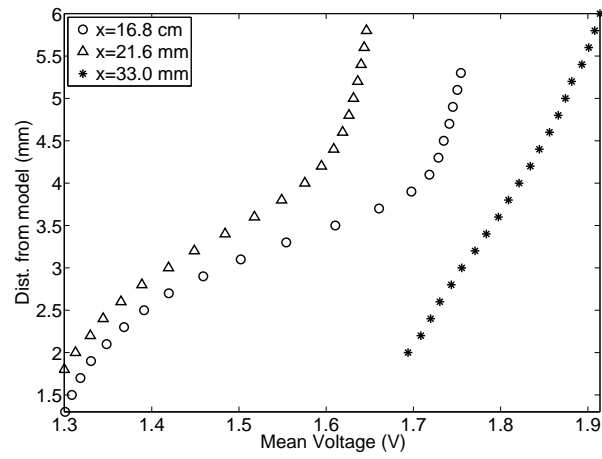
### 5.2.1 Boundary Layer Profiles

Uncalibrated hot-wire experiments were completed at an initial stagnation pressure of 620.5 kPa (90 psia). All data were recorded on the Tektronix DPO 7054 oscilloscopes at a sampling frequency of 5 MHz. The hot wires had an overheat ratio based on resistances very near 1.8, giving frequency responses on the order of 250 kHz. The wire diameters were all 0.005 mm (0.0002 in.) with a length/diameter ratio of about 80.

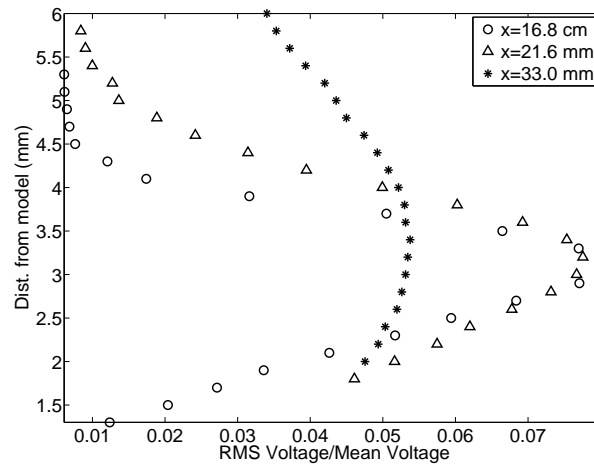
The hot wire was located at  $x=16.8$ , 21.6, and 33.0 cm (6.6, 8.5, and 13.0 in.). The wire was traversed through the boundary layer in 0.2 mm (0.008 in.) increments. After moving 0.2 mm (0.008 in.), the hot wire was held in position for 100 ms. It was then moved to the next station. In this way, the boundary layer was mapped and the approximate edge location measured. Figure 5.3a shows the boundary layer profiles at these three streamwise stations. Here, the mean voltage for each station above the model surface is plotted. Figure 5.3b shows the RMS voltage at each location.

The profiles for  $x=16.8$ , 21.6 cm (6.6 and 8.5 in.) behave as expected. As distance from the model increases, so does the voltage, until it begins to level out to the edge value. The edge was taken to be 4.1 and 4.3 mm (0.16 and 0.17 in.), respectively. The profile obtained at  $x=33.0$  cm (13.0 in.) is evidently not a full profile and should have been started farther from the model surface.

The peaks in RMS mass flux for  $x=16.8$ , 21.6, and 33.0 cm (6.6, 8.5, and 13.0 in.) occur at  $y=3.0$ , 4.8, and 4.6 mm (0.12, 0.13, and 0.18 in.), respectively. These values, when nondimensionalized by the boundary layer thickness, are 0.76 and 0.73 for  $x=6.6$  and 8.5 in.



(a) Mean voltage



(b) RMS voltage/Mean Voltage

Figure 5.3: Boundary layer profile. 620.5 kPa (90 psia), noisy flow



### 5.3 Natural Disturbances

In order to ascertain the state of the boundary layer at several streamwise stations as well as to make measurements of any naturally-occurring instability waves in noisy flow, a hot wire was stationed at  $x=16.8$ ,  $21.6$ , and  $33.0$  cm (6.6, 8.5, and 13.0 in.) at heights above the model surface of  $y=2.5$ ,  $2.8$ , and  $3.6$  mm (0.10, 0.11, and 0.14 in.), respectively. Nondimensionalizing by the measured boundary layer thickness gives wire positions of  $y/\delta= 0.63$ ,  $0.64$  at  $x=6.6$  and  $8.5$  in., respectively. Choosing these locations ensured that the wire would be in the boundary layer for the duration of the run, and near the location corresponding to the peak in rms voltage. This should have maximized the likelihood of measuring any natural second-mode disturbances in the boundary layer. Due to the frequent breakage of the wires, a different hot wire was used at each streamwise location.

Figure 5.4 shows the spectra of the uncalibrated bridge voltage. Welch's modified periodogram method with a Blackman window and 35% window overlap was used. Each spectrum is the average of 375 FFTs. The spectra shown in Figure 5.4 are over a 200 ms period from  $t=1.1$ - $1.3$  s after the start of the tunnel run. The average freestream Reynolds number during that time was  $6.9 \times 10^6/\text{m}$  ( $2.1 \times 10^6/\text{ft}$ ). The tunnel was run with conventional noise levels.

From the spectral data, it is not immediately clear whether the boundary layer at the streamwise stations is laminar or turbulent. It appears that the level of disturbances in the boundary layer increases significantly with increasing downstream distance. While it cannot be concluded that the boundary layer is turbulent at  $x=33.0$  cm (13.0 in.), it seems reasonable to assume that the boundary layer is at least transitional. This supports the TSP data of Figure 5.1b.

The most notable features of the spectra during the tunnel runs are the peaks around 200 kHz. These are somewhat surprising. Second-mode instability waves near this frequency have been measured in the BAM6QT previously [21]. Initially, this suggested that the disturbances may have been due to the second-mode instability.

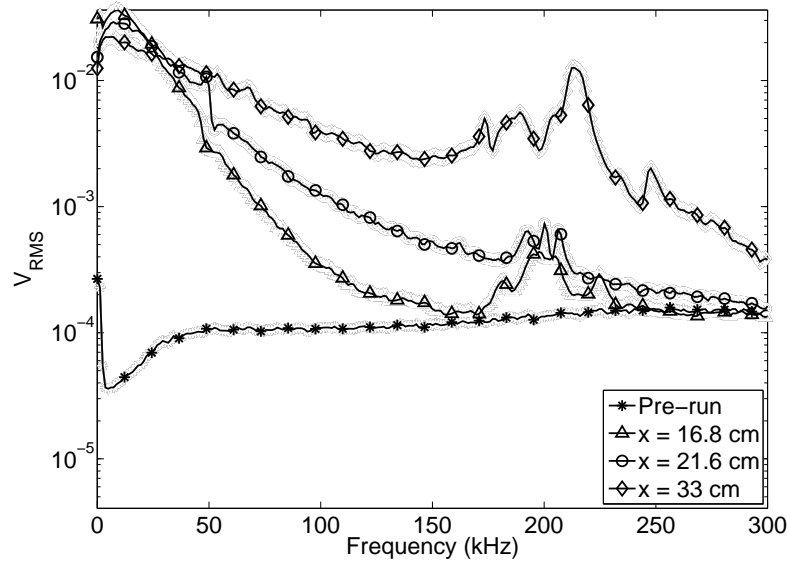


Figure 5.4: Spectra of CTA-bridge voltage at  $x=16.8$ , 21.6, and 33.0 cm (6.6, 8.5, and 13.0 in.), noisy

The fact that they are present at three streamwise stations with three different hot wires further supported this notion. However, the spectra at each location show fine structures within the larger peak, raising doubts about the nature of these peaks. The peaks of Ref. [21] were much more broad and smooth than those seen here. Also, STABL computations suggested that the most amplified second-mode frequency should have been around 100 kHz at all three locations. The spectra show no unique disturbances near that frequency. STABL does not currently model the crossflow instability. With the three-dimensional geometry of the X-51A, it is possible that considerable crossflow waves could be generated. Crossflow waves are one possible source of the 200 kHz peaks in the spectra. Additionally, 200 kHz is near the typical square-wave frequency response of the hot wires. Although the signal near 200 kHz appears to be quite large, its proximity to the wire frequency response could help explain the presence of the peaks in the spectra there.

It is possible that the hot wire was not positioned correctly in the boundary layer to measure the second mode. The cause of such large disturbances is unknown. Perhaps it is an abnormality with the wire and/or the anemometer. Another possible explanation is the length/diameter ( $l/d$ ) ratio of the wire. Traditionally, hot wires with a diameter of 0.004 mm (0.00015 in.) have been used on the probes. Due to frequent probe breakage, thicker wire with a diameter of 0.005 mm (0.0002 in.) was used for this test. Even though a thicker wire was used, the probe arms remained the same distance apart. This effectively reduced the  $l/d$  ratio, increasing the end-loss effects. Perhaps, in this case, the end-loss effects are large enough to preclude the detection of second-mode waves.

## 5.4 PCB Pressure Sensor Measurements

### 5.4.1 Motivation

Although hot wires can be and have proven to be very useful, they also suffer from some significant drawbacks. Since the wires are so fine, they are prone to regular breakage. However, when a new sting support and diffuser section were added to the tunnel, the frequency of probe breakage increased dramatically. In fact, most of the probes broke during their first time through the tunnel startup process. This suggests that startup with the new diffuser is likely more violent, causing the delicate wires to break due to significantly increased loading during startup. Additionally, the CTA used for these measurements was quite old. At times, it exhibited questionable behavior. It is possible that the CTA itself was outputting too much power and was responsible for the increase in probe failure. Whatever the cause, little data were collected with hot wires due to such frequent probe breakage during tunnel startup.

The new diffuser also decreased the tunnel run time and enhanced shock/boundary layer interaction problems. For quiet runs with the new diffuser, the nozzle wall boundary layer was observed to separate in an unsteady manner for nearly all quiet pressures. This separation often fed far upstream of the location where the model

shock impinged on the nozzle wall. This large, unsteady separation was observed in the TSP to trip an otherwise laminar model boundary layer to turbulent. In the past, such separations have also been observed to decrease the freestream Mach number to around 5 or less [76]. When run near the highest pressure providing quiet flow, about 1.03 MPa (150 psia), the nozzle-wall boundary layer usually stayed attached long enough to obtain some useful data. Thus, most runs with the PCB sensors were made with conventional noise levels.

In order to make measurements of instability waves and avoid these problems with hot wires, 5 PCB fast piezoelectric pressure transducers were installed flush with the model surface at streamwise stations of  $x = 19.3, 22.5, 25.7, 28.8,$  and  $31.9$  cm (7.5, 8.9, 10.0, 11.2, and 12.5 in.). As reported in section 3.3, these sensors have been used to measure second-mode instability waves for multiple models and wind tunnels. It was hoped that they could be successfully employed in the X-51A model to determine whether or not second mode waves were present in the leeward boundary layer and if they amplified with downstream distance.

#### 5.4.2 Natural Disturbances

Data will be shown for PCB sensors located at  $x = 19.3, 25.7, 28.8,$  and  $31.9$  cm (7.5, 10.0, 11.2, and 12.5 in.). There was an additional sensor at  $x = 22.4$  cm (8.8 in.), but it had a faulty connection for these runs and yielded no data. The data are reported in  $P_{RMS}/P_{Wall}$ , where  $P_{RMS}$  is the RMS pressure and  $P_{Wall}$  is the computed wall static pressure. This method gives quantitative amplitudes of the pressure fluctuations at the wall.

The experimental pressures were found by applying the manufacturer-supplied sensitivity to the measured voltages. Since the sensors are “time of arrival”, essentially AC-coupled, and nonlinear, obtaining a calibration is not a trivial task. The wall pressure was found by using computations provided by Chris Alba of the Air Force Research Laboratory [75]. However, the computations were for only one freestream

Reynolds number,  $6.6 \times 10^6/\text{m}$  ( $2.0 \times 10^6/\text{ft}$ ), which corresponds to a stagnation pressure of 620.5 kPa (90 psia). In order to report data for Reynolds numbers without computations, a simple assumption and calculations were made. It was assumed that the ratio of the wall static pressure to the freestream stagnation pressure was constant for each sensor location. Thus, when experiments were conducted for different Reynolds numbers, the measured stagnation pressure was multiplied by that ratio to obtain the wall static pressure. This pressure was used to non-dimensionalize the measured RMS pressure. Table 5.1 shows the computed wall pressure and ratio of wall pressure to stagnation pressure for each sensor location.

Table 5.1: Computed wall pressure and ratio of wall pressure to stagnation pressure for PCB pressure sensors

Sensor Location (cm)	$P_{Wall}$ (Pa)	$P_{Wall}/P_0$
19.3	692.5	0.001159
22.5	649.1	0.001046
25.7	606.2	0.000977
28.8	561.6	0.000905
31.9	502.9	0.000810

All PCB data were digitally high-pass filtered at 1 kHz with a five-pole butterworth filter. There was, evidently, a ground loop causing 60 Hz oscillations in the PCB output. A sample trace of the raw pre-run voltage is shown in Figure 5.5a. Figure 5.5b shows the same data after being filtered. This simple filtering effectively removed the 60 Hz oscillations from the signal.

Figures 5.7-5.9 show the RMS spectra of the calibrated PCB signals for conventional freestream noise and freestream Reynolds numbers of 3.3, 4.8, 5.8, 7.1, 7.7, 8.6, 10.1, and  $11.6 \times 10^6/\text{m}$  (1.0, 1.5, 1.8, 2.2, 2.4, 2.6, 3.1, and  $3.5 \times 10^6/\text{ft}$ ) at each of the four functional sensor locations,  $x=19.3$ , 25.7, 28.8, and 31.9 cm (7.6, 10.1, 11.3, 12.6 in.) on the model centerline. The spectrum of the pre-run signal is in-

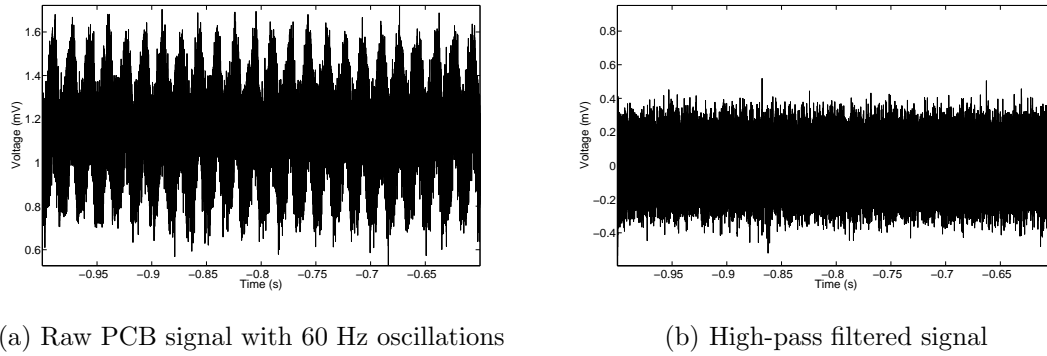


Figure 5.5: Raw pre-run PCB and high-pass filtered signal

cluded for comparison. The centerline streamwise temperatures are also shown in Figure 5.6. The corresponding sensor locations are marked by dashed lines. There are five Reynolds numbers for which both TSP and PCB data were collected. Additional Reynolds numbers were tested with the PCBs, and are also shown. Unfortunately, no TSP data were collected for freestream Reynolds numbers between  $3.2$  and  $7.1 \times 10^6/\text{m}$  ( $1.0$  and  $2.2 \times 10^6/\text{ft}$ ) because tunnel could not be reliably and repeatedly run at these conditions. No diaphragms exist that allow the tunnel to be operated in a standard manner for these conditions. The PCB data that are shown for  $3.2 \leq Re \leq 7.1 \times 10^6/\text{m}$  ( $1.0$  and  $2.2 \times 10^6/\text{ft}$ ) were collected by experimenting with the gap pressure and diaphragm setup in a trial-and-error manner. These conditions could not be easily replicated. In order to facilitate comparison of the data, some plots are shown in color. The Reynolds number of each colored spectral plot is very similar to the Reynolds number for the same-colored temperature plot. Additionally, for each sensor, disturbances around 100 kHz are shown in detail.

Each spectrum is computed for 100 ms of data, beginning at  $t = 1.1$  s. A Blackman window was used; its length was 1024 points. The sampling frequency was 5 MHz. The corresponding window time was 0.2048 ms. A 35% overlap between windows was used. Thus, each spectrum was the average of about 574 FFTs with a frequency resolution of 4.9 kHz.

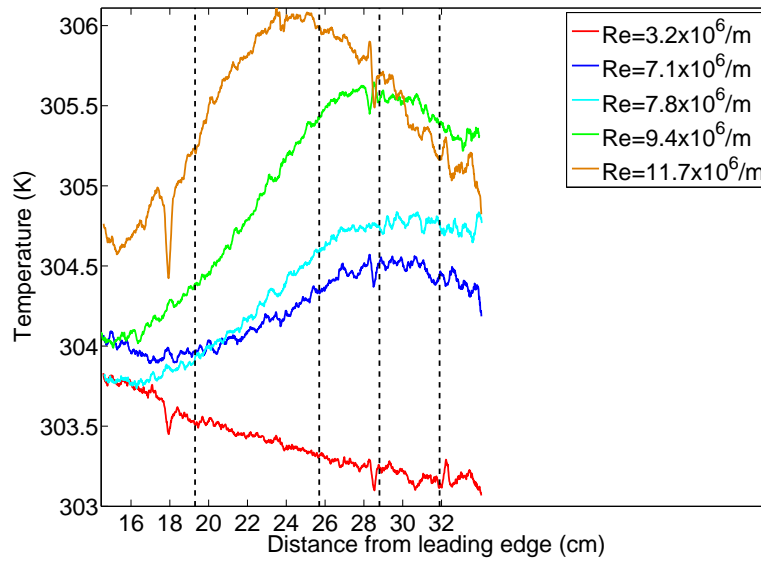
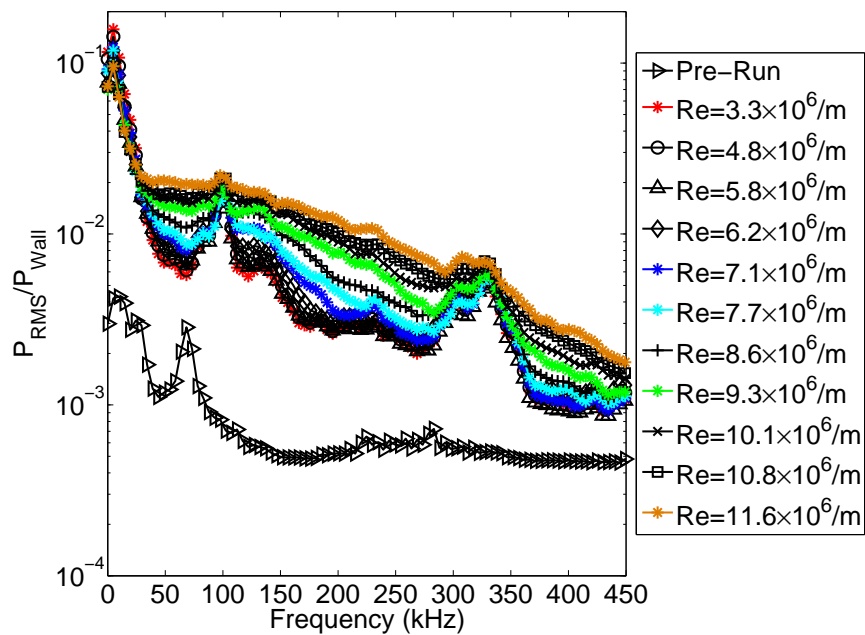
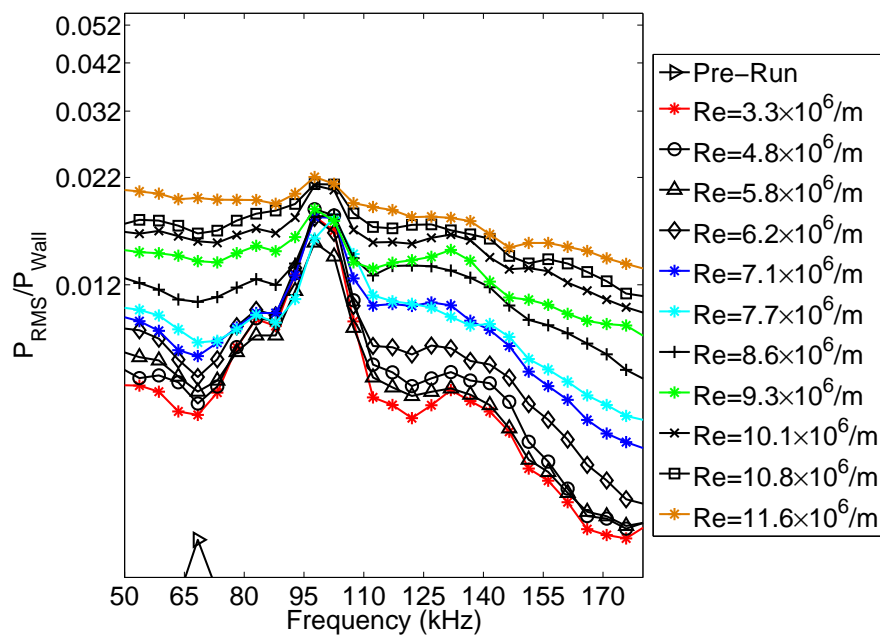


Figure 5.6: Centerline temperature for noisy flow

The spectra of Figure 5.7a show distinct peaks centered around 100 kHz and 320 kHz for  $Re$  up to  $9.3 \times 10^6/m$ . Figure 5.7b shows a detailed plot of the disturbances near 100 kHz. These peaks are not present in the pre-run spectra, suggesting they are due to physical processes in the boundary layer. They are somewhat evident at higher  $Re$ , but are of significantly lower relative amplitude compared to neighboring frequencies. As  $Re$  increases, increased spectral broadening is observed and the broadband noise approaches the peaks of the disturbance envelopes.

The centerline temperatures at  $x=19.3$  cm (7.6 in.) in Figure 5.6 suggest that the boundary layer there remains laminar for  $Re=3.2$  and possibly to  $7.1 \times 10^6/m$  ( $1.0$  and  $2.2 \times 10^6/ft$ ). For  $Re=7.8$ ,  $9.4$  and  $11.7 \times 10^6/m$  ( $2.4$ ,  $2.9$  and  $3.6 \times 10^6/ft$ ), transition onset has begun, as evidenced by increasing temperatures. Furthermore, since the middle of transition is typically at the peak in temperature, the temperature data suggest that even for  $Re=11.6 \times 10^6/m$  ( $3.6 \times 10^6/ft$ ), transition is not yet complete.

There is not a well-defined method of inferring transition onset from the PCB sensors. Casper [25] typically assumed transition onset when second-mode disturbance

(a) Spectra,  $x=19.3$  cm

(b) Detail view of PCB spectra near 100 kHz

Figure 5.7: PCB spectra for  $x=19.3$  cm



amplitudes stopped increasing and began to decrease with either increasing arclength or increasing freestream Reynolds number. However, her model was much longer than the X-51A model, the sensors were farther apart, and she saw large changes in wave amplitude for both increasing arclength and increasing freestream Reynolds number. Such significant changes in amplitude were not observed on the X-51A model, making Casper's transition-onset criterion implausible for the current experiments. Rather, transition onset as determined from the PCBs was taken to be the conditions at which the spectra began to depart from the laminar spectra at the lowest freestream Reynolds number. This causes some difficulty at the downstream sensors because even at the lowest freestream Reynolds number, the boundary layer may have begun the transition process, even though the TSP data suggest it remained fully laminar to the end of the model at the lowest Reynolds number tested. Nevertheless, this is the best criterion for transition onset that could be used.

The boundary layer behavior suggested by the TSP data is also seen in the PCB spectra of Figure 5.7. Here, the broadband spectra fall nearly on top of each other for  $3.3 \leq \text{Re} \leq 5.8 \times 10^6/\text{m}$  ( $1.0$  and  $1.8 \times 10^6/\text{ft}$ ). Above this value, noise rapidly increases with Reynolds number and the peaks near 100 and 320 kHz broaden. This suggests that the boundary layer remains laminar for Re up to  $5.8 \times 10^6/\text{m}$  ( $1.8 \times 10^6/\text{ft}$ ). Transition onset appears to occur between  $\text{Re}=5.8$  and  $6.2 \times 10^6/\text{m}$  ( $1.8$  and  $1.9 \times 10^6/\text{ft}$ ). For larger Re, the spectra do not fall on top of each other. Furthermore, even for  $\text{Re}=11.6 \times 10^6/\text{m}$  ( $3.5 \times 10^6/\text{ft}$ ), small peaks around 100 and 320 kHz are still evident in the spectra. These behaviors suggest that at  $x=19.3$  cm (7.6 in.), the transition process was not completed for the test conditions. For  $x=19.3$  cm (7.6 in.), the PCB and TSP data are in agreement.

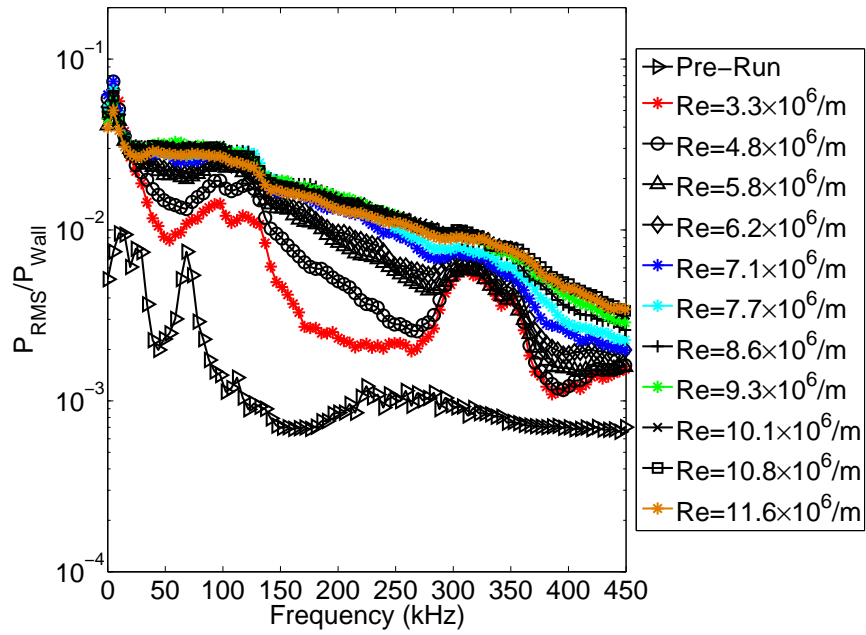
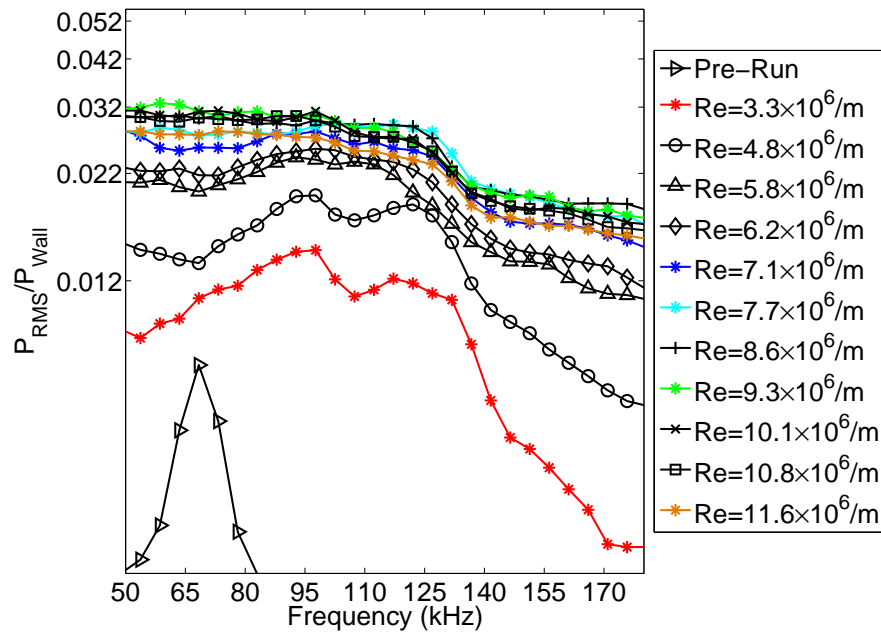
Figure 5.8 shows the PCB spectra at  $x=25.7$  cm (10.1 in.). There are many similar features to the data at  $x=19.3$  cm (7.6 in.). The peaks around 100 and 320 kHz are observed again for some Reynolds numbers. Here, however, the peaks are only clear up to  $\text{Re}=6.2 \times 10^6/\text{m}$  ( $1.9 \times 10^6/\text{ft}$ ). For larger Re, the peaks are not as clear, and the broadband noise has increased significantly. This suggests that transition onset occurs

by about  $Re=4.8 \times 10^6/m$  ( $1.5 \times 10^6/ft$ ). Additionally, for the higher Reynolds numbers, the spectra begin to fall nearly on top of each other, suggesting that transition is complete or nearly complete at  $x=25.7$  cm (10.1 in.) for  $Re > 7.1 \times 10^6/m$  ( $2.2 \times 10^6/ft$ ). Also, the amplitudes of the disturbance envelopes appear to have grown. Discussion of quantifying this growth will follow. The TSP data show that transition onset has occurred for  $3.2 < Re < 7.1 \times 10^6/m$  ( $1.0$  and  $2.2 \times 10^6/ft$ ). Again, the TSP and PCB data agree.

Figure 5.9 shows the PCB spectra at  $x=28.8$  cm (11.3 in.). Here, disturbance envelopes are seen for  $Re=3.3 \times 10^6/m$  ( $1.0 \times 10^6/ft$ ). For all higher Reynolds numbers tested, the disturbances around 100 kHz are mostly lost in the broadband noise. The disturbances around 320 kHz are evident to about  $Re=4.8 \times 10^6/m$  ( $1.5 \times 10^6/ft$ ), but are also washed out for higher  $Re$ . This suggests that transition onset likely occurs by  $Re=4.8 \times 10^6/m$  ( $1.5 \times 10^6/ft$ ). For  $Re \geq 5.8 \times 10^6/m$  ( $1.8 \times 10^6/ft$ ), the spectra fall nearly on top of each other. This indicates that the boundary layer at  $x=28.8$  cm (11.3 in.) is fully turbulent or nearly fully turbulent for  $Re \geq 5.8 \times 10^6/m$  ( $1.8 \times 10^6/ft$ ). The TSP data of Figure 5.6 again support the PCB measurements. At  $x=28.8$  cm (11.3 in.), the TSP shows that the boundary layer is well into the transition process for  $Re \geq 7.1 \times 10^6/m$  ( $2.2 \times 10^6/ft$ ).

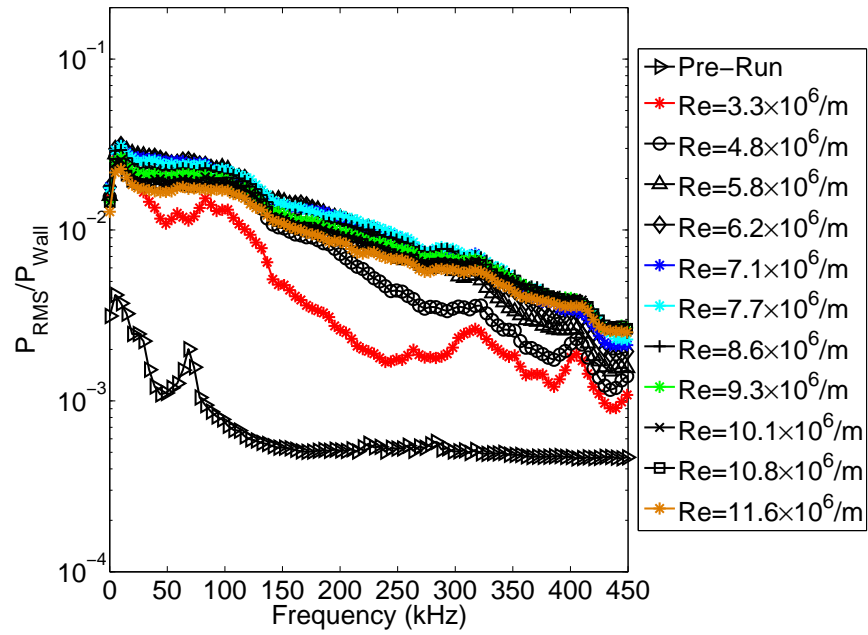
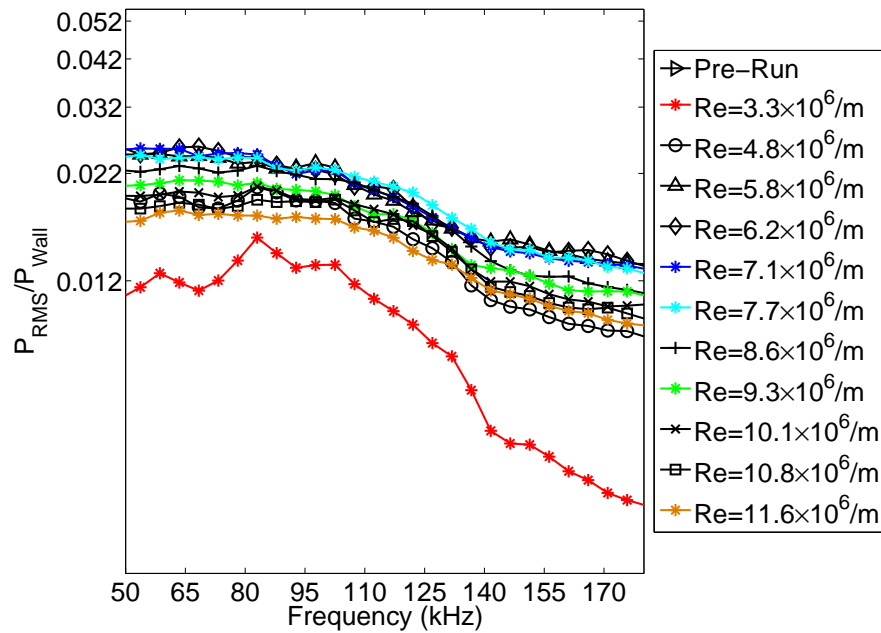
Figure 5.10a shows the PCB spectra at  $x=31.9$  cm (12.6 in.). Disturbances are noted around 100 and 320 kHz for  $Re$  up to  $4.8 \times 10^6/m$  ( $1.5 \times 10^6/ft$ ). Above this Reynolds number, the peaks are lost in the broadband noise. The spectra for higher Reynolds numbers lie nearly on top of each other again. These data suggest that at  $x=31.9$  cm (12.6 in.), transition onset occurs by  $Re=5.8 \times 10^6/m$  ( $1.8 \times 10^6/ft$ ). The TSP data support this conclusion. From the TSP, transition has occurred or is nearly complete at  $x=31.9$  cm (12.6 in.) for all but the  $Re=3.2 \times 10^6/m$  ( $1.0 \times 10^6/ft$ ) case. Table 5.2 summarizes the freestream Reynolds number at the estimated transition onset for both PCB and TSP data.

In addition to the RMS spectra, the power spectral density (PSD) of the PCB signals was computed. This function was then integrated over the disturbance fre-

(a) Spectra,  $x=25.7$  cm

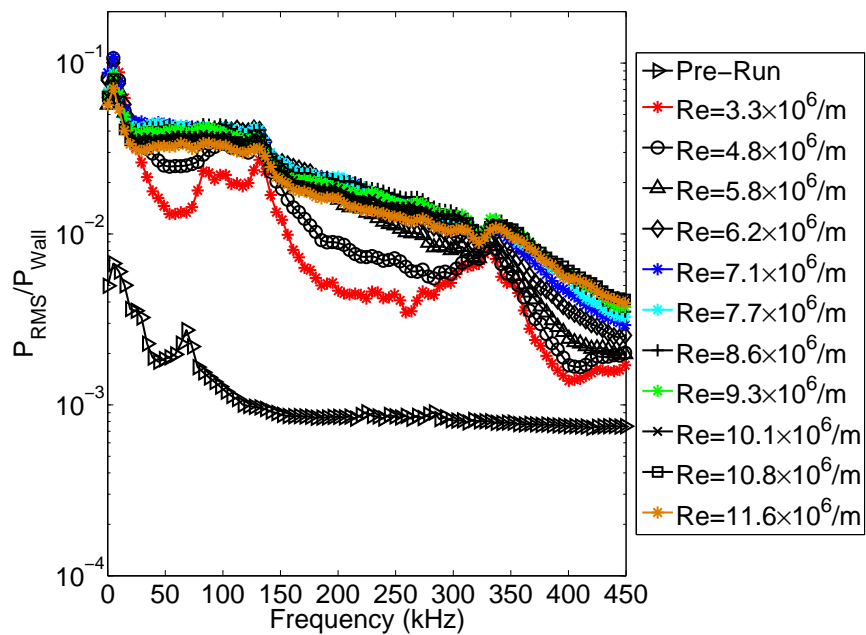
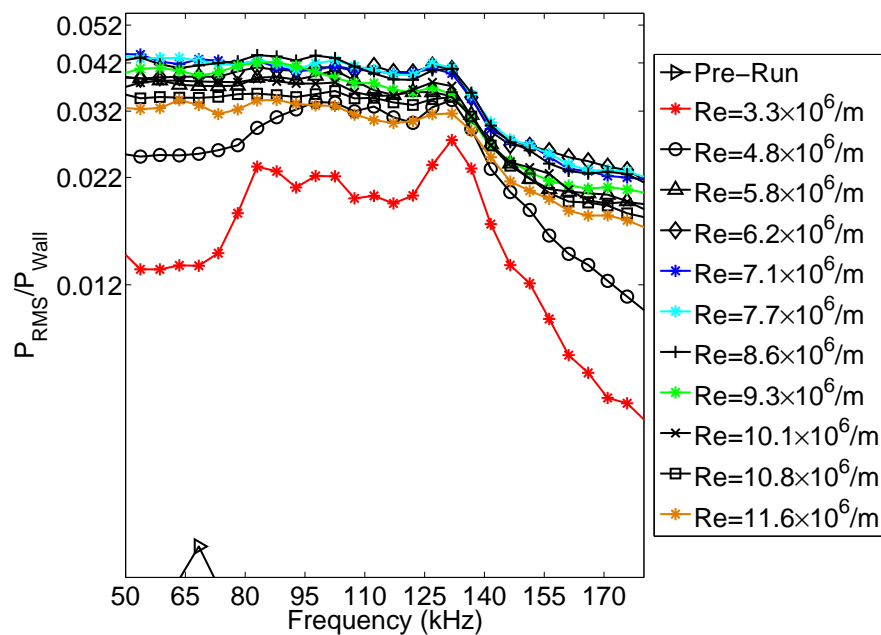
(b) Detail view of PCB spectra near 100 kHz

Figure 5.8: PCB spectra for  $x=25.7$  cm

(a) Spectra,  $x=28.8$  cm

(b) Detail view of PCB spectra near 100 kHz

Figure 5.9: PCB spectra for  $x=28.8$  cm

(a) Spectra,  $x=31.9$  cm

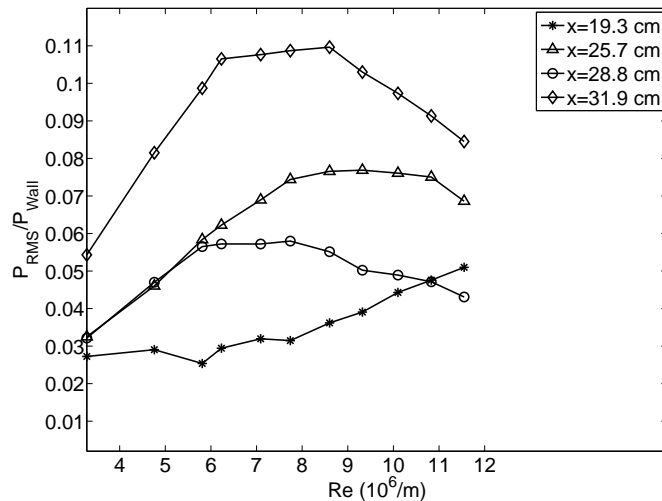
(b) Detail view of PCB spectra near 100 kHz

Figure 5.10: PCB spectra for  $x=31.9$  cm

Table 5.2: Reynolds number for estimated transition onset for PCB and TSP data

	$Re_t$ at onset ( $\times 10^{-6}$ )	
$x$ (cm)	PCB	TSP
19.3	5.8-6.2	$\approx 7.1$
25.7	3.3-4.8	3.2-7.1
28.8	3.3-4.8	3.2-7.1
31.9	3.3-4.8	3.2-7.1

quency bands. This integration quantifies the disturbance amplitudes of the RMS pressure fluctuations owing to disturbances in the band of interest. The PSD were integrated from 75 to 125 kHz and are shown in Figure 5.11. Here, the amplitude of the disturbance envelope is plotted as a function of Reynolds number for each sensor. The amplitudes reported here do not correspond to the amplitude of the most amplified frequency. The spectra are too uneven and the resolution too poor to allow this sort of precision. Rather, it is the integrated amplitude of the band of amplified frequencies.

Figure 5.11: RMS disturbance amplitudes between 75 and 125 kHz for constant  $x$

The most upstream sensor, located at  $x=19.3$  cm (7.6 in.), shows fluctuation amplitudes simply increasing with Reynolds number. The other sensors show a different qualitative behavior. Here, the disturbance amplitudes grow with Reynolds number, plateau, and then decrease. The sensor at  $x=31.9$  cm (12.6 in.) plateaus beginning at  $Re=6.2\times 10^6/m$  ( $1.9\times 10^6/ft$ ). For  $x=25.7$  cm (10.1 in.), the amplitude does not plateau until  $Re=8.6\times 10^6/m$  ( $2.6\times 10^6/ft$ ).

Increasing the Reynolds number at a constant location is akin to observing fluid behaviors further into the transition process. This trend is in line with what was observed in the TSP data. Transition at  $x=31.9$  cm (12.6 in.) onset occurs for a lower Reynolds number than at  $x=25.7$  cm (10.1 in.). The rise in disturbance amplitude with increasing Reynolds number can be attributed to the destabilization of the boundary layer at higher Reynolds number. This, in turn, gives rise to larger-amplitude instability waves than for lower Reynolds numbers. When the Reynolds number increase is substantial enough to cause wave amplitudes to be of sufficient magnitude, breakdown and transition are expected. When turbulent structures within the boundary layer have sufficiently developed, further wave growth is not expected. However, the waves themselves may persist for a distance before being washed out in the turbulence. As the boundary layer breaks down, spectral energy should be shifted away from the wave frequency as the spectra develop broadband behavior typical of fully turbulent boundary layers. This could explain the plateaus in disturbance amplitude.

As shown in Table 5.2, the TSP shows transition onset occurring between  $Re=7.1$  and  $7.8\times 10^6/m$  ( $2.2$  and  $2.4\times 10^6/ft$ ) at  $x=19.3$  cm (7.6 in.). For  $x=25.7$ , 28.8, and 31.9 cm (10.1, 11.3, and 12.6 in.), the TSP shows that transition onset occurs between  $3.2$  and  $7.1\times 10^6/m$  ( $1.0$  and  $2.2\times 10^6/ft$ ). Unfortunately, the Reynolds number for onset cannot be further resolved from the TSP data. Given the range of Reynolds numbers for transition onset at  $x=25.7$ , 28.8, and 31.9 cm (10.1, 11.3, and 12.6 in.), it appears that onset occurs for  $0.03 < P_{RMS}/P_{Wall} < 0.10$ . This range is too large to

be helpful. However, for  $x=19.3$  cm (7.6 in.), onset is taken to be between 7.1 and  $7.8 \times 10^6/\text{m}$  ( $2.2$  and  $2.4 \times 10^6/\text{ft}$ ). This corresponds to  $P_{RMS}/P_{Wall} \approx 0.03$ .

It should be noted that disturbance amplitudes are somewhat less for the sensor at  $x=28.8$  cm (11.3 in.). Experience has shown that not all individual PCB sensors can be used to accurately measure high-frequency disturbances. It appears that this is the case for this sensor. The spectra calculated for this sensor as well as the disturbance amplitudes are typically the lowest of all the sensors. This does not make sense from a fluid dynamics standpoint. It is more likely that this sensor simply does not function properly in measuring amplitudes. Nevertheless, data from this sensor have been included since the qualitative trend of the spectra is somewhat in line with the other PCB sensors and the TSP results.

The disturbances near 320 kHz are surprising. Figure 5.12 shows the RMS pressure amplitudes for the disturbances near 320 kHz. They behave somewhat like the disturbances around 100 kHz. The RMS amplitudes grow with downstream distance for constant Reynolds number. There is, however, no plateau of amplitudes for varying Reynolds number at constant location. Rather, the amplitudes increase to a maximum value and then decrease.

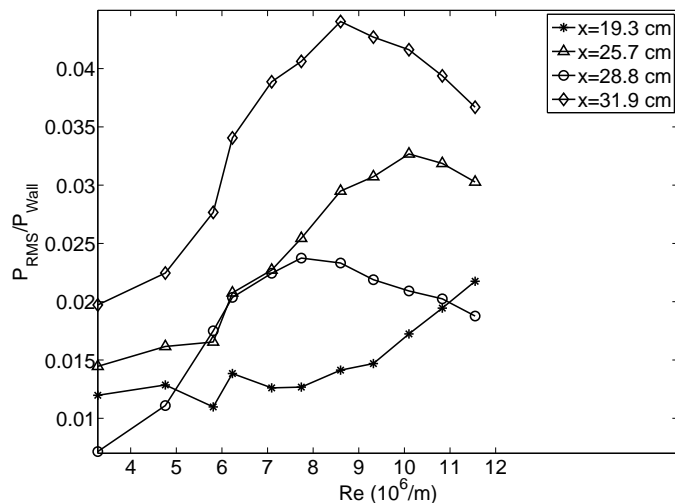


Figure 5.12: RMS disturbance amplitudes between 270 and 370 kHz for constant  $x$



It seems that the disturbances near 320 kHz should not be negated, as they may affect the transition process. At  $x=19.3$  cm (7.6 in.), transition onset was taken to be between  $Re=7.1$  and  $7.8 \times 10^6/m$  ( $2.2$  and  $2.4 \times 10^6/ft$ ). Here, the RMS amplitude of the disturbances near 100 kHz was about 3%. The RMS amplitude of the disturbances near 320 kHz is about 1.25%, over 1/3 of the primary disturbance amplitude.

Disturbances at 320 kHz were not predicted by the computations, and are observed to have significantly lower RMS amplitude than the 100 kHz waves, about half the amplitude of the lower-frequency disturbances. It could be that the disturbances at that frequency are due to some unknown instability. Its effect on the transition process and any nonlinear interaction with the disturbances at 100 kHz is unknown.

It would be interesting to determine the effect of freestream noise on disturbance amplitudes. Unfortunately, with the exception of the highest freestream Reynolds numbers for quiet flow, the nozzle wall boundary layer separated. The separation was observed for the small steel insert in the sting support section with all gap spacings. Disturbance amplitudes could thus only be compared at one freestream condition. Figure 5.13 shows the results. Here, the low freestream noise levels were for  $Re=10.5 \times 10^6/m$  ( $3.2 \times 10^6/ft$ ), while conventional noise levels were for  $Re=11.5 \times 10^6/m$  ( $3.5 \times 10^6/ft$ ).

With low freestream noise levels and for both frequency bands, a clear increase in disturbance amplitude with  $x$  is observed, with the exception of the possibly faulty sensor at  $x=28.8$  cm (11.3 in.). Thus, for low noise levels, the magnitudes of the disturbance envelopes grew with  $x$ , which would be expected if the disturbances were due to instabilities in the boundary layer. With conventional freestream noise, the disturbance amplitudes also grew with  $x$ , but with larger changes in the slope of the noise from point to point, almost leveling off between  $x=22.5$  and 28.8 cm (8.9 and 11.3 in.). This is not altogether surprising, however, in light of the observed transition onset discussed above. For  $Re=11.5 \times 10^6/m$  ( $3.5 \times 10^6/ft$ ), transition onset had occurred at all sensor locations.

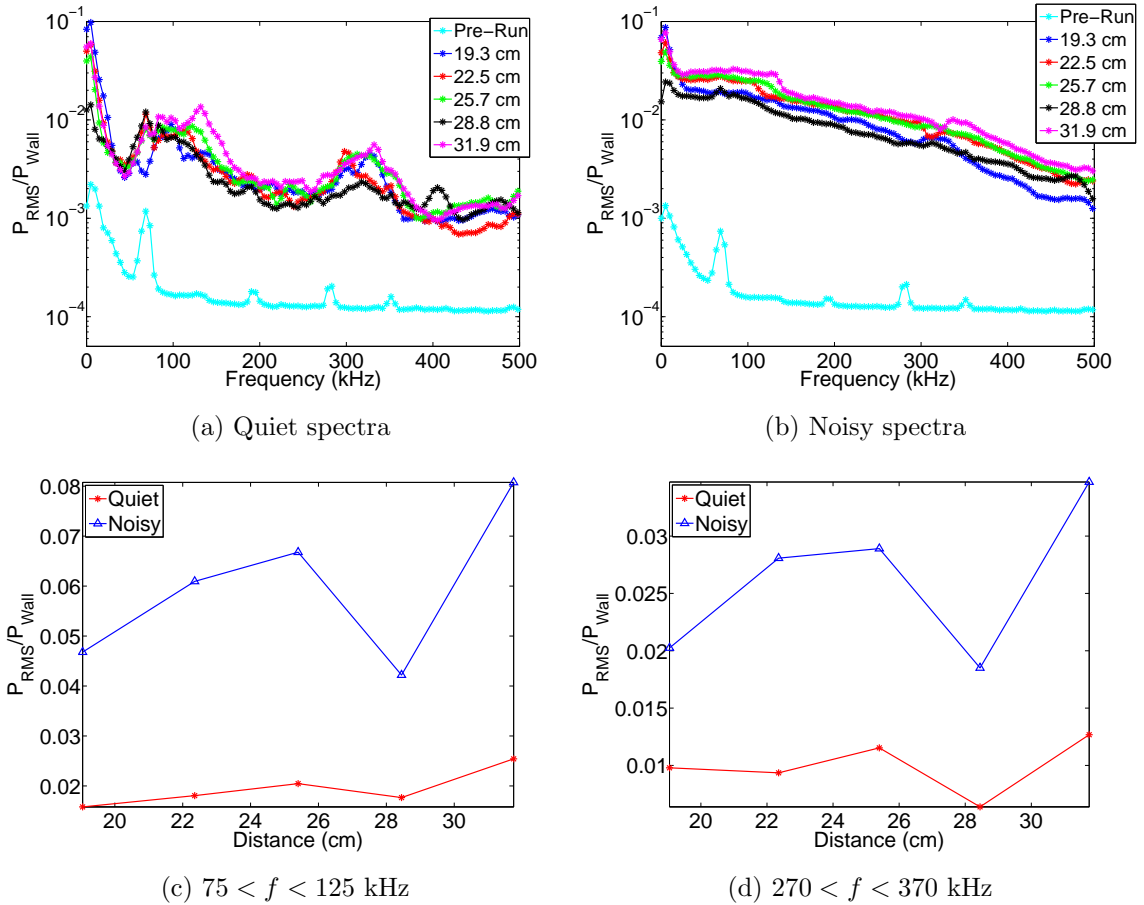


Figure 5.13: Disturbance amplitudes and spectra for quiet,  $Re=10.5 \times 10^6/m$ , and noisy,  $Re=11.5 \times 10^6/m$ , flow

These data suggest that the disturbances near 100 kHz are due to an instability in the boundary layer. As previously discussed, at  $x=19.3$  cm (7.6 in.), transition onset was taken to be between  $Re=7.1$  and  $7.8 \times 10^6/m$  ( $2.2$  and  $2.4 \times 10^6/ft$ ) with a wave amplitude of about 3%. With low freestream noise levels, the disturbance RMS amplitude does not even reach 3%. Thus, transition onset is not expected at any location on the model with low noise levels. Transition onset was not observed in the TSP, as detailed in Figure 5.2b.

Computations predicted that, for  $Re=6.6 \times 10^6/m$  ( $2.0 \times 10^6/ft$ ), the most amplified second-mode frequency would be 100 kHz. It seems likely, then, that the 100 kHz

instability waves are due to the second mode instability. The data suggest that transition on the leeward surface of the X-51A is affected by the spatial amplification and breakdown of second mode waves.

Although the 100 kHz disturbances are likely due to the second mode instability, this conclusion still remains speculative. If these disturbances really were second mode waves, it would be expected that their amplitudes would grow exponentially with downstream distance. This trend is not clear in the data, however. This could be due to as yet unresolved PCB calibrations. The PCB sensors also suffer from limited spatial resolution. The sensor diameter is 0.32 cm (0.13 in.). As such, the sensors average a relatively large area. For instability waves at 100 kHz convecting downstream at the approximate freestream velocity of 875 m/s (2.87 kf/s), the wavelength is about 0.9 cm (0.3 in.). Thus, the sensor diameter is approximately  $\lambda/3$ , where  $\lambda$  is the disturbance wavelength. Thus, disturbances near 100 kHz are probably near the resolution of the sensor, which may impact the effectiveness of the sensor to measure second mode disturbances. However, Casper [25] reports that the PCB sensor diameter was approximately  $\lambda/2$  for the second-mode waves that she successfully measured with the PCB sensors.

Also, as the Reynolds number changes, so too does the boundary layer thickness. Since second-mode waves are highly tuned to the boundary layer thickness, the frequency of the waves would also be expected to change with freestream Reynolds number. This trend was not observed. It is also troubling that the spectra of the hot-wire signal (Figure 5.4) did not show disturbances at 100 kHz nor at 320 kHz. The discrepancy between the hot wire and PCB data could be due to the hot wires not being positioned correctly in the boundary layer. If the hot wire were too close to the boundary layer edge, it is less likely the second-mode waves would be measured. Additionally, these amplitudes are normalized with the computed surface pressures. The accuracy of the computations has not yet been verified. There remains much work to be done to fully utilize PCB sensors to measure second-mode waves.

## 5.5 Glow Perturber

As has been demonstrated, it is important to better understand the influence of freestream noise on stability and transition of model boundary layers in wind tunnels. Stability measurements should be made under both conventional and quiet noise levels. Comparison of measurements under these conditions should give insight into how increased freestream noise levels affect stability. Past experience has shown that the hot wires used in the BAM6QT to measure instabilities with conventional freestream noise levels have not yet measured the much lower-amplitude waves present under low noise levels [21].

In order to measure instability waves under both quiet and conventional freestream noise levels, a method of introducing controlled disturbances into the boundary layer is desired. A glow discharge perturber is able to meet this criterion. After disturbances of a known frequency are created in the boundary layer, it was hoped that the amplification and/or damping of instability waves could be measured, even under quiet conditions.

A glow perturber is essentially two electrodes separated by a dielectric material. The width of the dielectric material between the two electrodes and the static pressure between the electrodes are the critical variables that determine the necessary electric potential to break down the air. Paschen's Law describes the breakdown voltage as a function of the parameter  $Pd$  where  $P$  is the static pressure and  $d$  is the electrode spacing for various gases [77]. An increasing electric potential is applied to the two electrodes. When the voltage reaches a high enough value, based on the value of  $Pd$ , the air in the gap will break down in a glow discharge. This breakdown transfers energy to the flow, heating a small volume of fluid to high temperature, which causes perturbations in the flow. When the applied electrode voltage is forced at an arbitrary frequency, flow fluctuations can be introduced into the boundary layer of a model at a desired frequency.

### 5.5.1 Glow Perturber Design

A glow discharge perturber of the type used by Ladoon [28] was designed for the leeward side of the X-51A. The X-51A model was made with a circular, removable insert to accommodate the installation of a surface glow-discharge perturber. The insert can be seen in Figure 2.4d. The center of the insert is located on the centerline at  $x=8.8$  cm (3.45 in.) downstream of the model's leading edge.

In order to minimize the necessary applied voltage for breakdown of the air, the value of  $Pd$  for the X-51A glow perturber was chosen to be the minimum for air. Table 4.1 of Ref. [77] lists this as 0.754 Pa·m with a corresponding breakdown voltage of 327 V. Unpublished CFD calculations estimated the surface pressure at the glow perturber for a stagnation pressure of 965 kPa (140 psia) to be 1.726 kPa (0.25 psia) [78]. This gave an ideal electrode separation distance of 0.044 cm (0.017 in.). This distance was chosen as the dielectric thickness. The electrode dimensions were arbitrary and based on what seemed small enough not to leave a large footprint on the model surface yet large enough so that fabrication was relatively easy.

The glow perturber consists of an inner electrode, made from copper alloy 145 Tellurium. This alloy is approximately 99.5% copper and 0.5% Tellurium, according to the supplier-provided material property sheet. It has a 1.02 mm (0.040 in.) diameter. The inner electrode is surrounded by a Macor ceramic sheath, 0.43 mm (0.017 in.) thick. This dielectric layer is then surrounded by the outer electrode, fabricated from brass alloy 360. It has an inner diameter of 1.91 mm (0.075 in.) and an outer diameter of 6.99 mm (0.275 in.). All three parts are epoxied together using Cotronics Duralco 4700 high-temperature epoxy. The drawing for the glow perturber is shown in Figure B.1.

The glow unit was epoxied into the steel model insert. The surface was then hand-finished by a skilled machinist to match the surface contour of the X-51A as closely as possible. Figure 5.14 is a photograph of the glow perturber. In Figure 5.14, the center circle is the inner, copper electrode. The white ring around it is the ceramic

dielectric. The larger ring outside that is the brass electrode. These materials are fitted into the steel model insert, which is also visible in Figure 5.14.



Figure 5.14: Glow perturber as installed

Once the glow perturber was fabricated, it was installed in the model. One 20-gauge, braided, high-voltage wire is soldered to the inner electrode. This wire then passes through the model, angle-of-attack adapter, and hollow sting. The outer electrode is grounded by a path comprised of the model itself, the angle-of-attack adapter, sting, and another 20-gauge, braided, high-voltage wire leading from the sting to the ground of the glow electronics. From the back of the sting to the glow electronics, these two wires are twisted together in order to reduce electromagnetic (EM) noise.

The electronics that power the glow perturber were slightly modified from those developed by Ladoon, described in detail in Ref. 79. When the glow perturber is active, the large amount of EM noise picked up by a hot wire and other instruments precludes running the glow continuously. Thus, several electronics components are used to operate the glow perturber in a pulsed fashion, generating the desired fluctuating electric potential applied to the glow electrodes. The end result is bursts of

a set number of cycles of a sine wave. Useful hot-wire measurements can then be collected between the glow pulses.

When operating the glow perturber in a pulsed manner such as this, there are several important time scales to be considered. Figure 5.15 demonstrates the timing needed to successfully operate the glow perturber. When the oscilloscopes trigger, a transistor-transistor logic (TTL) signal is generated. This voltage is not high enough to trigger the next electronic box in the system, so it is first amplified by triggering an HP 8011A pulse generator. The pulse generator makes one 8 V pulse. This pulse is used to trigger a Quantum Composers 9310 pulse generator. This pulse generator is used to select a delay time before triggering the glow perturber. This delay is denoted as  $t_d$  in Figure 5.15. The delay is necessary because the CTA circuitry always oscillates briefly during tunnel startup. During normal tunnel operations, the oscillation lasts for a very short time. When the glow begins operating during startup while the hot wire is oscillating due to startup, it was found that the hot wire continued to oscillate even after startup was complete. This is most likely due to the amount of EM radiation picked up by the hot wire while the glow is operating. Introducing a delay into the signal gives the anemometer the chance to stop oscillating before the glow perturber is activated. The output from the pulse generator then triggers an HP 33120A function generator. This function generator selects the frequency at which pulses of wave packets will be produced. The time between pulses is denoted as  $t_p$  with the corresponding frequency  $1/t_p = \omega_p$ . This signal then triggers an Agilent 33120A function generator. This function generator sets the frequency and number of wave cycles that will be produced each pulse. The length of time the wave packets are produced is symbolized by  $t_b$  and the wave period is  $t_w$  with the corresponding wave frequency of  $1/t_w = \omega_w$ .

The signal output by the Agilent 3312A is amplified by a circuit built by Ladoon [79]. A schematic of the amplifying glow electronics is shown in Figure 5.16. The AC signal from the Agilent 33220A is first amplified with a gain of 10 by a custom-built power amplifier based on an Apex PA19 power-operational amplifier. The amplifier

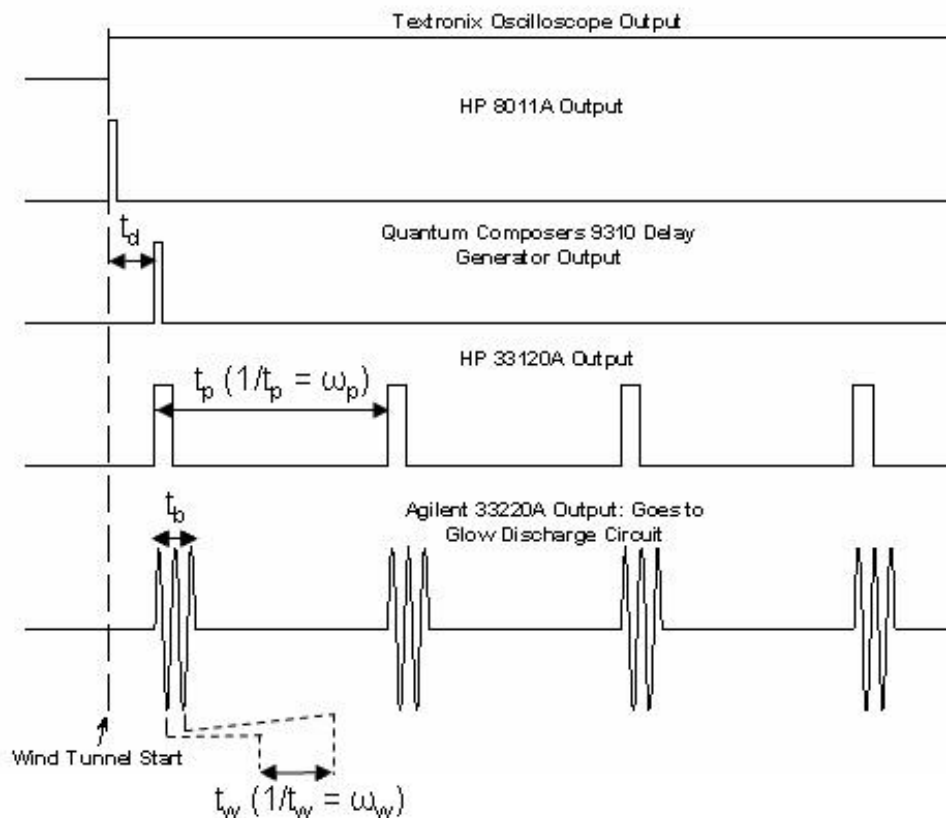


Figure 5.15: Glow perturber signal

output is fed into a custom-built step-up signal transformer with a turns ratio of 60 a frequency bandwidth of 20 to 500 kHz, and a power rating of 1000 W. The transformer increases the electrode voltage until breakdown of the air in the electrode gap occurs. The secondary side of the circuit, downstream of the transformer, includes a 20 k $\Omega$  ballast resistor which limits current and prevents the discharge from becoming an arc. The ballast resistor can be changed to modify the current of the glow and thus the power and amplitude of the artificial disturbance. A rectifying diode, as shown in Figure 5.16, is also placed in parallel with the electrodes. Depending on its orientation, either the positive or negative half of the amplified sine wave can be selected to cause the glow discharge. It was found that when the inner electrode was the cathode, a much smaller glow was created than when the inner electrode was the



anode. This better approximates a point disturbance, which is preferred for these experiments.

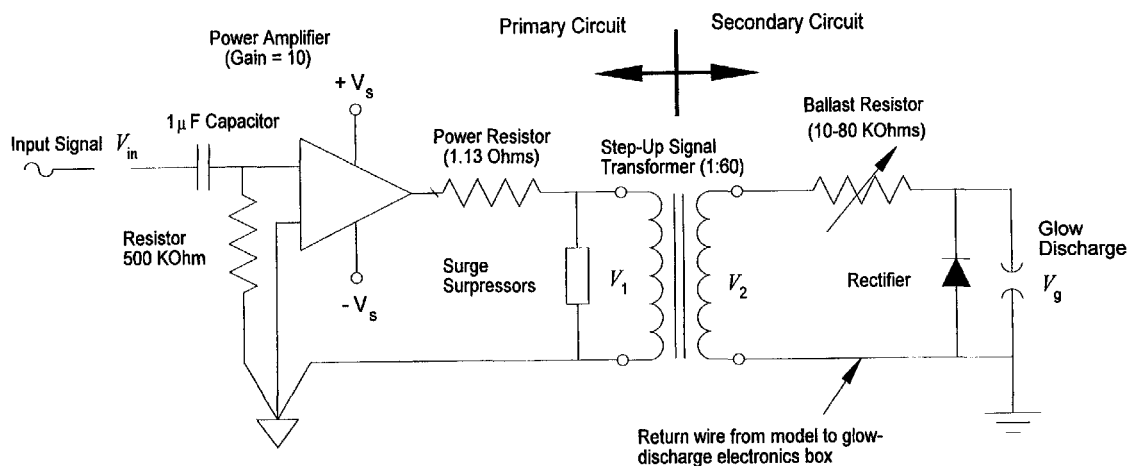


Figure 5.16: Glow-discharge circuit (taken from Ref. [79])

### 5.5.2 Hot Wire Measurements with the Glow Perturber

Although natural disturbances were seen under noisy conditions for frequencies near 200 kHz with the hot wires, the glow perturber was only operated at a frequency of 30 kHz. At the time of the hot-wire measurements, preliminary computations showed that the most unstable mode was the first mode at about 30 kHz. Four cycles of this 30 kHz wave were produced every 0.5 ms ( $\omega_p=2$  kHz). At present, the glow electronics are not capable of sustaining a visible glow discharge at 200 kHz. Testing the glow electronics took place under static conditions at a pressure of about 690 Pa (0.1 psia). Due to the short run time of the Mach-6 tunnel, the range of the glow perturber could not be tested while the tunnel was operating. It is likely that either the ballast resistor, transformer, or both, will have to be changed to allow glow operations at 200 kHz. The 30 kHz frequency was chosen with the hope that it would excite first-mode wave growth. The glow was only run under noisy tunnel

conditions with an initial stagnation pressure of 620.5 kPa (90 psia). Again, for these measurements, if the tunnel was run with low freestream noise levels at this pressure, the nozzle-wall boundary layer separated in an unsteady and unpredictable fashion, yielding little or no meaningful data.

The hot wire was first positioned at  $x=16.8$  cm (6.6 in.), 8.0 cm (3.2 in.) downstream of the glow perturber. Although this does not give a large distance for the disturbances to grow, it was thought that they could at least be measured there. The wire was positioned at  $y=4.1, 3.8, 3.6, 2.5, 1.5$  mm (0.16, 0.15, 0.14, 0.10, and 0.06 in.). These gave  $y/\delta$  values of 1.0, 0.94, 0.88, 0.63, and 0.39, respectively.

In order to determine reasonable settings for the glow electronics, a few simple estimates were made. The flow at the edge of the boundary layer has a velocity on the order of 875 m/s. Assuming this is the approximate convection speed of the disturbances, this means that a disturbance created at the glow location,  $x=8.8$  mm (3.45 in.), reaches the hot wire approximately 0.1 ms later. The glow electronics were configured so that the glow would be on for 0.13 ms then off for 0.37 ms. This meant that the wave train was expected to reach the hot wire at about the time the glow was turned off. The wave train would entirely move past the hot wire 0.13 ms after that. This leaves 0.24 ms of margin before the glow comes on again, in case the waves actually reached the hot wire later than expected.

The signal output by the glow electronics was amplified by a power amplifier and step-up transformer. The amplified wave train was applied across the glow-perturber electrodes. The amplitude of the signal input into the amplifying circuit was 7.5 V peak-to-peak. Figure 5.17 shows a portion of the voltage-time history of the potential applied across the electrodes and also of the CTA bridge for a typical tunnel run using the glow perturber. The four cycles of 30 kHz sine wave can clearly be seen in the electrode voltage. There is often also significant electrical pickup observed in the hot-wire trace when the glow is running, as seen in the hot-wire voltage trace in Figure 5.17.

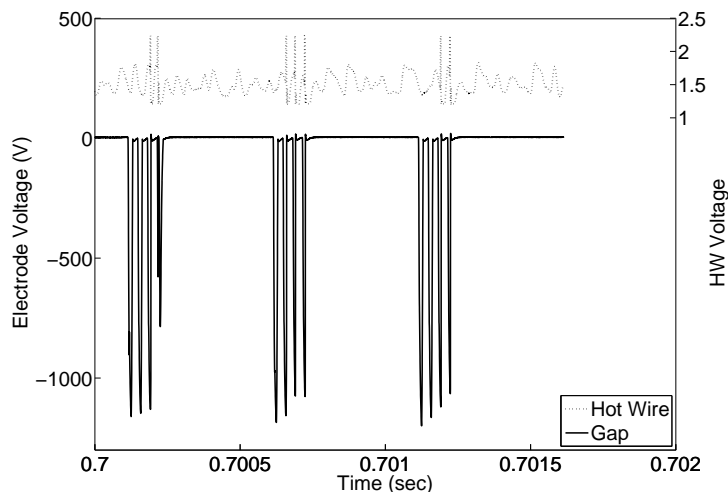


Figure 5.17: Sample voltage traces of electrode gap and CTA bridge voltage

Pulsing the glow in this way allows many wave bursts to be ensemble averaged. This averaging should reduce noise and allow the disturbances to be more readily detected in the hot-wire traces. Each ensemble-averaged trace is the average of the CTA signal from 2000 glow events. This corresponds to one second of run time. It would be better to only ensemble average between the 200 ms expansion-wave reflections in the driver tube. However, so much extra noise is introduced into the hot-wire signal when running with conventional noise levels that more averaging is needed to clearly see the artificial disturbances. This noise can be seen as much of the seemingly random voltage fluctuations between glow pulses in Figure 5.17.

Ensemble-averaged traces and power spectra for  $x=16.8$  cm (6.6 in.) and  $y/\delta=1.0, 0.94, 0.88, 0.63,$  and  $0.39$  are shown in Figure 5.18. For each plot, the range of voltages displayed is the same. The actual values differ, however, so that the details at each  $y/\delta$  can be seen. The relative position of  $t=0$  was set by examining the electrode-gap voltage trace and determining when the last wave packet of each glow-discharge burst had ended. Thus, in the ensemble-average traces, the portions of the signal for  $t < 0$  are while the glow discharge is being made. Portions of the signal for  $t > 0$  are

the periods of useful data collection, uncontaminated by high electromagnetic (EM) radiation. The EM pickup seems to vary with  $y/\delta$ . The reason for this is unknown. It seems unlikely that any fluid phenomenon would cause the hot wire to so drastically vary in its EM pickup. Perhaps this is due to random changes in the glow perturber itself from run to run.

As is seen in the plots, there are no clear wave packets seen at  $y/\delta=1.0$ . There are, however, high-frequency, low-amplitude oscillations. For  $y/\delta=0.94$ , however, wave packets are clearly seen starting at about  $t=-0.02$  ms. This timing, relative to the end of the wave-packet generation, fits very well with the estimated time of arrival of the wave packets, given the tunnel freestream conditions. Waves are even more distinguishable for  $y/\delta=0.88$  and  $0.63$ , but are not clearly evident for  $y/\delta=0.39$ .

Figure 5.18f also shows the artificial 30 kHz disturbances. Here, the window length of the root mean square spectrum (RMSS) is equal to the length of the signal being analyzed. This was taken to be the length of time it took to produce the four cycles of 30 kHz sine wave, 0.13 ms. The portion of the signal that was analyzed is taken from the ensemble-averaged voltage trace for  $0.00 < t < 0.13$  ms. This window is the approximate time it should take for the wave train to completely move past the hot wire. Given the short window length, the best frequency resolution that could be obtained was about 5 kHz. There are clear peaks at 30 kHz for  $y/\delta=0.94$ ,  $0.88$ , and  $0.63$ . There is no evident peak at 30 kHz for  $y/\delta=1.00$  or  $0.39$ , which also seems obvious from the ensemble-averaged traces. The many other, smaller-amplitude peaks in Figure 5.18f are mostly integer multiples of 30 kHz and are possibly harmonics or artifacts of the windowing. For  $y/\delta=1.00$ , there is also a noticeably larger peak at about 230 kHz. This peak is due to the small-amplitude fluctuations visible in Figure 5.18a. This may be indicative of second-mode waves. However, the frequency is about 30 kHz higher than the peaks seen in Figure 5.4. It seems clear, then, that the 30 kHz disturbances introduced into the boundary layer of the X-51A are of measurable amplitude within the range of about  $y/\delta=0.63-0.94$ .

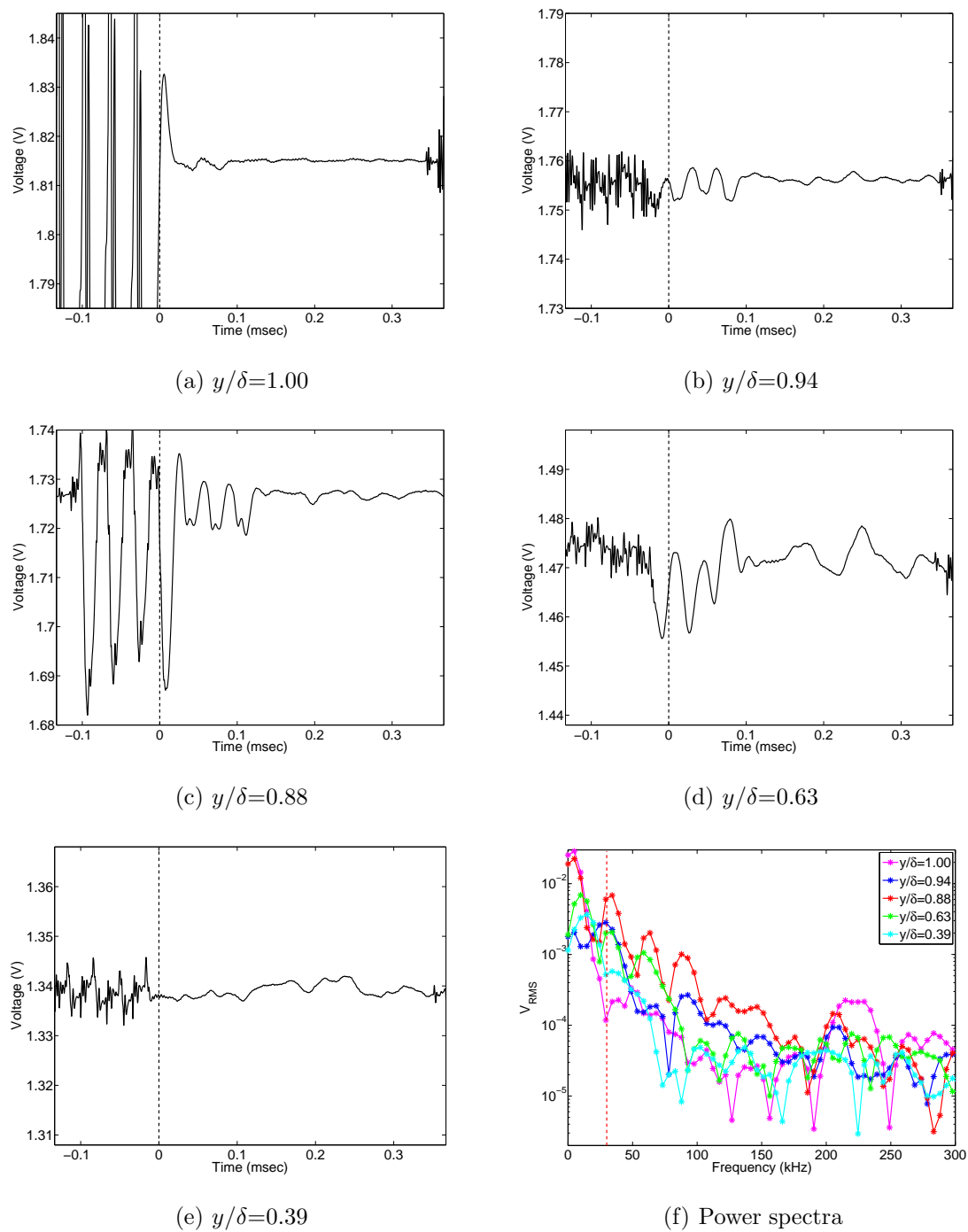


Figure 5.18: Ensemble-averaged CTA bridge voltage traces and power spectra with glow perturber running at 30 kHz, noisy flow,  $x=16.8$  cm (6.6 in.)

The hot wire was moved downstream to  $x=21.6$  cm (8.5 in.) and similar measurements were made, this time at  $y/\delta=1.00, 0.93, 0.87,$  and  $0.64,$  based on  $\delta=0.17$  in. Figure 5.19 shows ensemble-averaged voltages and spectra. For  $y/\delta=1.00$  and  $0.93,$  the same hot wire was used as was used in the data of Figures 5.18a-5.18e. After these tunnel runs, however, the hot wire broke. Thus, for  $y/\delta=0.87$  and  $0.64,$  a different probe was used.

Wave packets are clearly seen for  $y/\delta=1.00, 0.93,$  and  $0.64.$  For  $y/\delta=1.00$  and  $0.64,$  four cycles of 30 kHz disturbances are easily discernible. The four cycles are not quite as clear for  $y/\delta=0.93.$  For  $y/\delta=0.87,$  it is not clear what is happening. A 30 kHz disturbance is easy to see. However, it appears that at least 5 cycles may be seen. The spectra in Figure 5.19e show peaks near 30 kHz for all  $y/\delta$  values. Also, these seem to generally have higher magnitudes. This gives some indication that the disturbances may be growing with downstream distance.

For  $y/\delta=1.00, 0.93,$  and  $0.64,$  the wave packets appear in the signal about 0.05 ms after they did at  $x=16.8$  cm (6.6 in.) This time lag is demonstrated in Figure 5.20. Here, the ensemble-averaged traces for  $y/\delta=0.63$  are shown for  $x=16.8$  and  $21.6$  cm (6.6 and 8.5 in.). The portions of the signals highlighted in red correspond to when the wave packets are moving past the hot wire and are 0.13 ms long, the length of time for 4 cycles of a 30 kHz wave to be produced. Based on a convection speed of about 875 m/s, it should take the generated wave packets about 0.055 ms longer to reach the hot wire at  $x=21.6$  cm (8.5 in.) as compared to  $x=16.8$  cm (6.6 in.). This close agreement with a first-order approximation demonstrates that the disturbances measured here are actually from the glow perturber. Figure 5.19e took the delayed arrival of the wave packets into account. The window over which the FFT was computed was from  $t=0.055-0.185$  ms.

Additional runs were made with the glow perturber operating at different frequencies from 40-130 kHz. Similar measurements with different glow frequencies were also attempted with low freestream noise levels, but yielded no data due to separation of

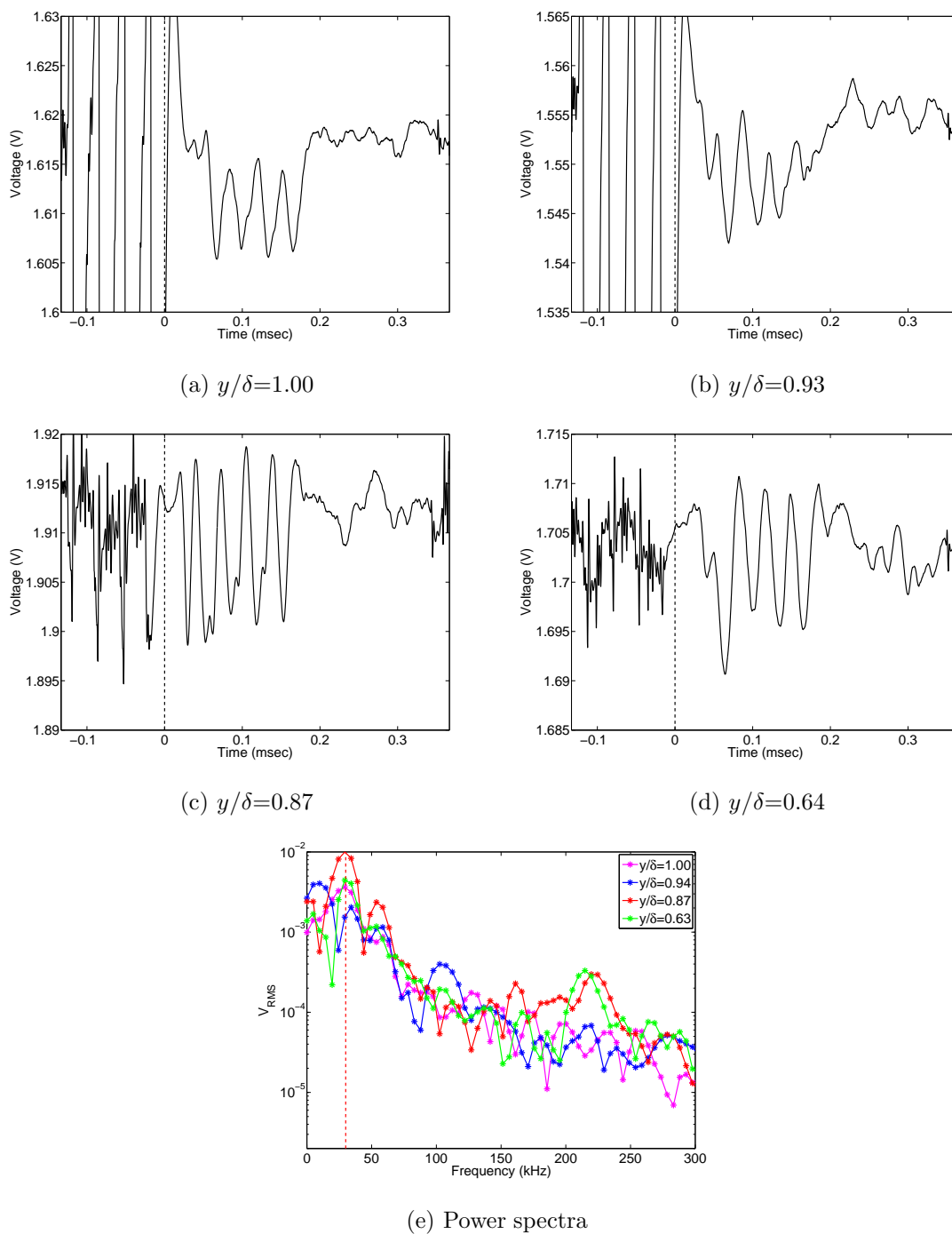


Figure 5.19: Ensemble-averaged CTA bridge voltage traces and power spectra with glow perturber running at 30 kHz, noisy flow,  $x=21.6$  cm (8.5 in.)

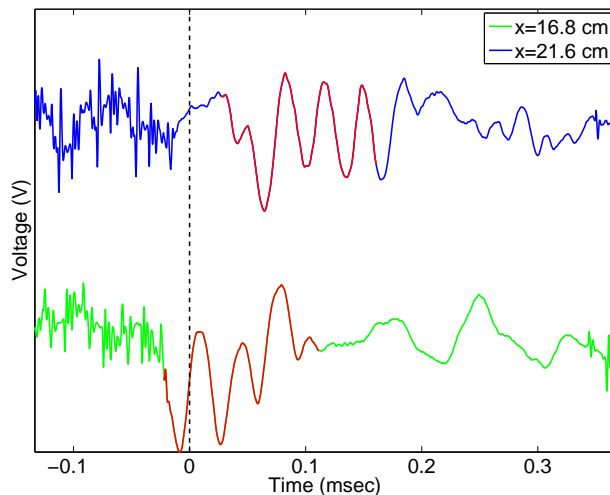


Figure 5.20: Ensemble-averaged voltage traces for  $x=16.8$  and  $21.6$  cm (6.6 and 8.5 in.)

the nozzle-wall boundary layer. Disturbances created by the glow perturber were not observed in any of these experiments.

### 5.5.3 PCB Pressure Sensor Measurements with Glow Perturber

In order to remove some of the problems and limitations of hot wires, PCB sensors were also used in conjunction with the glow perturber at 621 kPa (90 psia). In this case, the glow perturber produced 10 sine wave cycles with  $\omega_w=100$  kHz with  $t_p=0.05$  ms between bursts. The glow was run at  $\omega_w=100$  kHz because at the time of the PCB measurements, the second mode was predicted to be the most unstable mode with a frequency of about 100 kHz. It was hoped that the additional perturbations introduced by the glow would further destabilize the boundary layer, causing larger waves to be measured and possibly inducing early transition.

Spectra of the PCB signals from the sensors at  $x=19.1$ , 25.4, 28.4, and 31.8 cm (7.5, 10.0, 11.2, and 12.5 in.) for runs with and without the glow perturber operating were computed. Here, the spectra were computed in a different manner than before.



The length of each pulse of waves is only 1 ms long. Instead of computing one FFT of an ensemble-averaged signal, an FFT was taken of the signal after each glow burst. These FFTs were then averaged to give power. However, the FFTs were not computed from the entire signal between glow bursts. Because of the glow perturber settings, there is 0.5 ms between the start of each burst. The wave packets are only produced for 0.1 ms. Thus, the wave packets will move past a given sensor in only 0.1 ms. If the FFT were computed for the entire 0.4 ms of usable signal after the glow perturber was done operating, the presence of artificial disturbances would not be as evident because there would be no waves present for 75% of the signal. Thus, a rough estimate of the time-of-arrival,  $t_a$ , of the waves to each sensor was made. The waves were assumed to travel at near the freestream velocity, about 850 m/s. Table 5.3 shows  $t_a$  for each sensor. This arrival time, different for each sensor, became the starting time for the FFT computation at that sensor. For each sensor, the FFTs were calculated for the signal 0.1 ms long starting at  $t_a$ .

Table 5.3: Estimated time of arrival at each PCB pressure sensor for disturbances created at the glow perturber

Sensor Location (cm)	Distance from Glow (cm)	$t_a$ (ms)
19.3	10.5	0.12
25.7	16.9	0.20
28.8	20.0	0.24
31.9	23.1	0.27

It is possible that the disturbances moved slower or faster than the estimated velocity. If this were the case, this method of calculating the spectra would fail to detect the disturbances. Thus, spectra were also computed for the signal 0.1 ms long starting at  $t_a-0.10$  ms,  $t_a-0.05$  ms,  $t_a+0.05$  ms, and  $t_a+0.10$  ms. However, at  $x=28.8$  and 31.9 cm (11.3 and 12.6 in.), the spectra were not computed for  $t_a+0.10$  ms. Since  $t_a$  at these locations was larger than at the upstream locations, the additional 0.10 ms

meant that the signal for which the spectra were computed would have included some of the time that the glow perturber was on, rendering these data useless. All these spectra were also compared to spectra computed from a run with the same initial conditions but without the glow running. The PCB signals from the run without the glow were processed in exactly the same manner as the signals from the run with the active glow so that a comparison could be made. Figures 5.21-5.22 show the results. As is immediately evident, there is very little difference in the spectral content of the signals, regardless of the starting point of the FFT calculations or whether or not the glow perturber was being used. Artificial disturbances at 100 kHz produced by the glow perturber cannot be detected downstream by the PCB sensors. This is evidenced by the negligible difference in the spectra with the glow on and off.

Since 30 kHz disturbances caused by the glow perturber were detected with the hot wire, the glow perturber was also run at 30 kHz with the PCB sensors installed. As with the higher-frequency disturbances, the 30 kHz disturbances caused by the glow perturber were not observed. An explanation of why the 30 kHz waves were measured by the hot wire but not the PCB sensors is given in Section 5.5.4.

#### **5.5.4 Explanation of Glow Measurements from CFD**

Both the measured natural disturbances near 100 kHz and the lack of any effect of the glow perturber can be explained by computations made for the Purdue model at Mach-6 tunnel conditions. The computations were done by Graham Candler (University of Minnesota), Matt MacLean (CUBRC), Heath Johnson (University of Minnesota), and Chris Alba (AFRL) using the STABL software suite. The mean flow was computed using a Navier-Stokes solver. Stability computations came from solutions to the parabolized stability equations. Information about STABL is detailed in Ref. [8]. The simulated stagnation pressure was 602.5 kPa (90 psia). The Mach number was 6.0, the freestream stagnation temperature was 451 K, and the angle of attack was 4°.

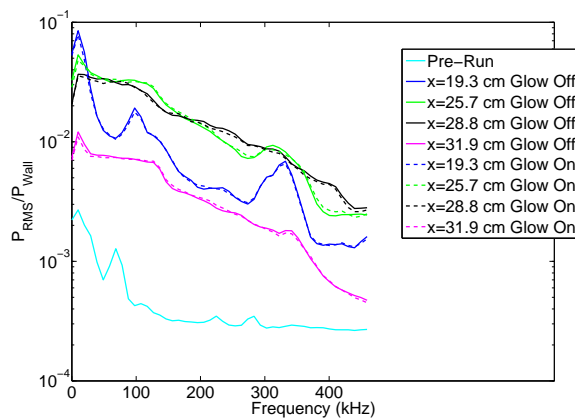
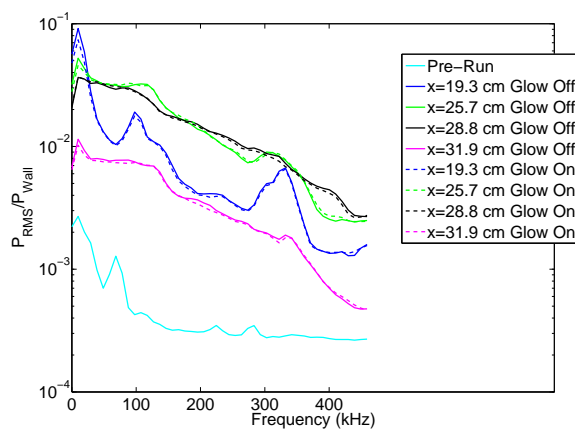
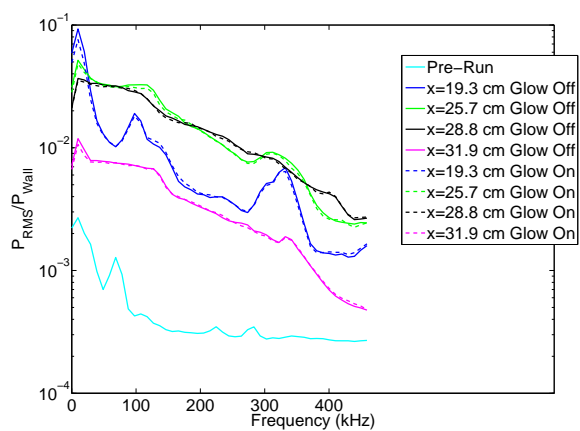
(a)  $t_a$ (b)  $t_a - 0.10$  ms(c)  $t_a - 0.05$  ms

Figure 5.21: Averaged FFTs of PCB signals with and without glow perturber for various signal windows

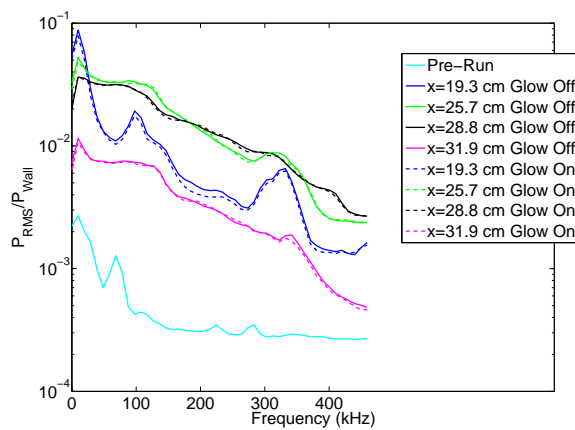
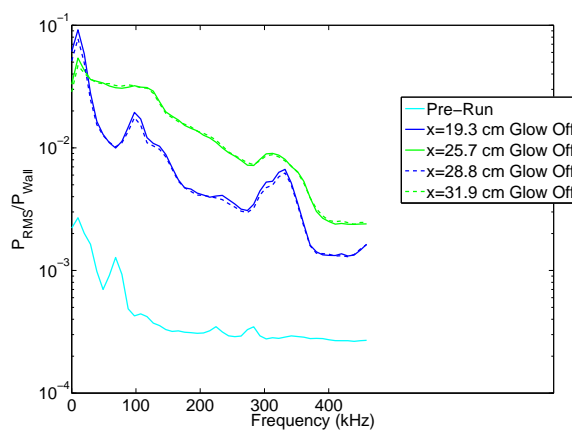
(a)  $t_a + 0.05$  ms(b)  $t_a + 0.10$  ms

Figure 5.22: Averaged FFTs of PCB signals with and without glow perturber for various signal windows

Figure 5.23, generated by Chris Alba, shows  $N$  factor and the most amplified second-mode frequencies. The locations of the glow perturber and the five PCB sensors are marked by vertical lines. At the PCB sensors, the most amplified second-mode frequency is about 100 kHz. This explains the peak in the PCB spectra around 100 kHz, and further substantiates the theory that those disturbances were due to the second mode instability.  $N$  factors from the point where the disturbances first start to grow are noted by the black squares. Also shown as red squares are  $N$  factors reflecting wave growth from the glow perturber location. Here, the  $N$  factor for each streamwise station is for the most unstable frequency. Thus, the  $N$  factor curves really show wave growth for an envelope of frequencies. The  $N$  factor is predicted to reach a value of about 4.4 at the most downstream sensor at  $x = 31.8$  cm (12.5 in.). This is likely not high enough to cause transition under low noise levels. However, with high, conventional noise levels, it seems possible that transition could occur. With conventional freestream noise levels, and at tunnel conditions matching the computations, TSP showed transition onset at about  $x = 18$  cm (7.1 in.). This is about 1 cm (0.4 in.) upstream of the most upstream sensor. Figure 5.23 shows that the most unstable frequency is near 100 kHz from about  $x = 13$  cm (5.1 in.) to the end of the model. Thus, waves of that frequency are expected to begin growing somewhat upstream of the most upstream PCB sensor. The growth and breakdown of second mode instability waves of about 100 kHz may explain the behavior observed in both the TSP and PCB measurements.

Additionally, Figure 5.24 shows the stability diagram for the X-51A lee side in the Purdue Mach-6 tunnel. Again, the PCB locations are marked by vertical lines. The glow perturber is located at the upstream extent of the diagram. The shape of the neutral curve explains why disturbances created at the glow perturber were not present nor detected by the PCB sensors. At the glow perturber, only waves with frequencies between 145 and 180 kHz amplify. Disturbances at 100 kHz do not undergo amplification until about  $x = 18.0$  cm (7.1 in.), 9.2 cm (3.6 in.) downstream of the glow perturber. Thus, any 100 kHz disturbances introduced by the glow into

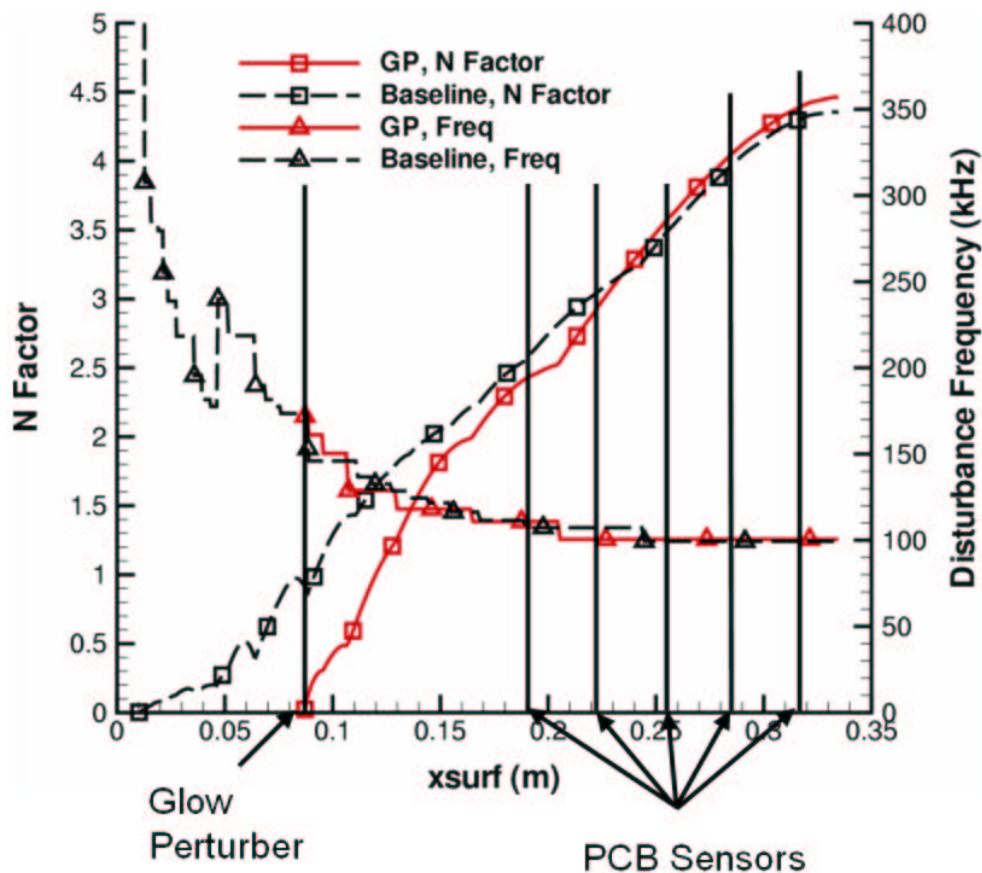


Figure 5.23: Computations for N-factors and most unstable frequencies (from [75])

the flow are damped immediately. It seems likely that these disturbances would damp out entirely by the time they reached the region of amplification and the PCB sensors, 10.3 cm (4.1 in.) downstream. This explains why the effect of the glow perturber was never detected by the PCB sensors.

Figure 5.25 shows what would have happened had the glow been used to make disturbances between 140 and 180 kHz. Here, the waves would have initially amplified quickly. However, due to the steepness of the neutral curve, these waves would have stopped amplifying and instead undergone exponential decay no farther downstream than  $x=13.2$  cm (5.2 in.), only 4.4 cm (1.7 in.) downstream of the glow perturber. This is still 5.9 cm (2.3 in.) upstream of the most upstream PCB sensor. It seems

likely that waves of that higher frequency would have also damped out by the time they would have moved past the PCB sensors. Thus, due to the position of the glow perturber relative to the PCB sensors and the steepness of the neutral curve, it appears that at these conditions, no disturbances at second-mode frequencies created by the glow perturber could be detected by the PCBs. This explains why there are only negligible differences in the spectra with and without the glow operating.

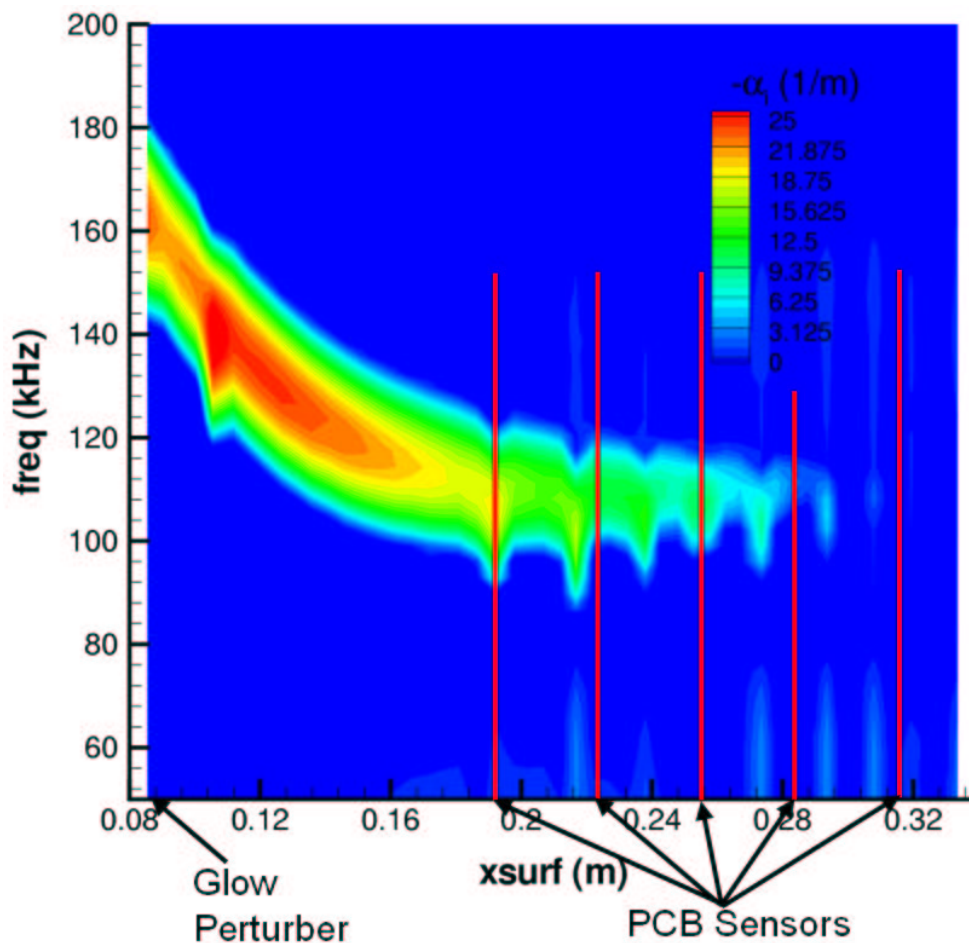


Figure 5.24: Computed stability diagram for X-51A (from [75])

The computations also provide an explanation of why the 30 kHz disturbances produced by the glow perturber were detected downstream on the model with the hot wire, but not with the PCB sensors. Figure 5.26 shows the amplification rate as

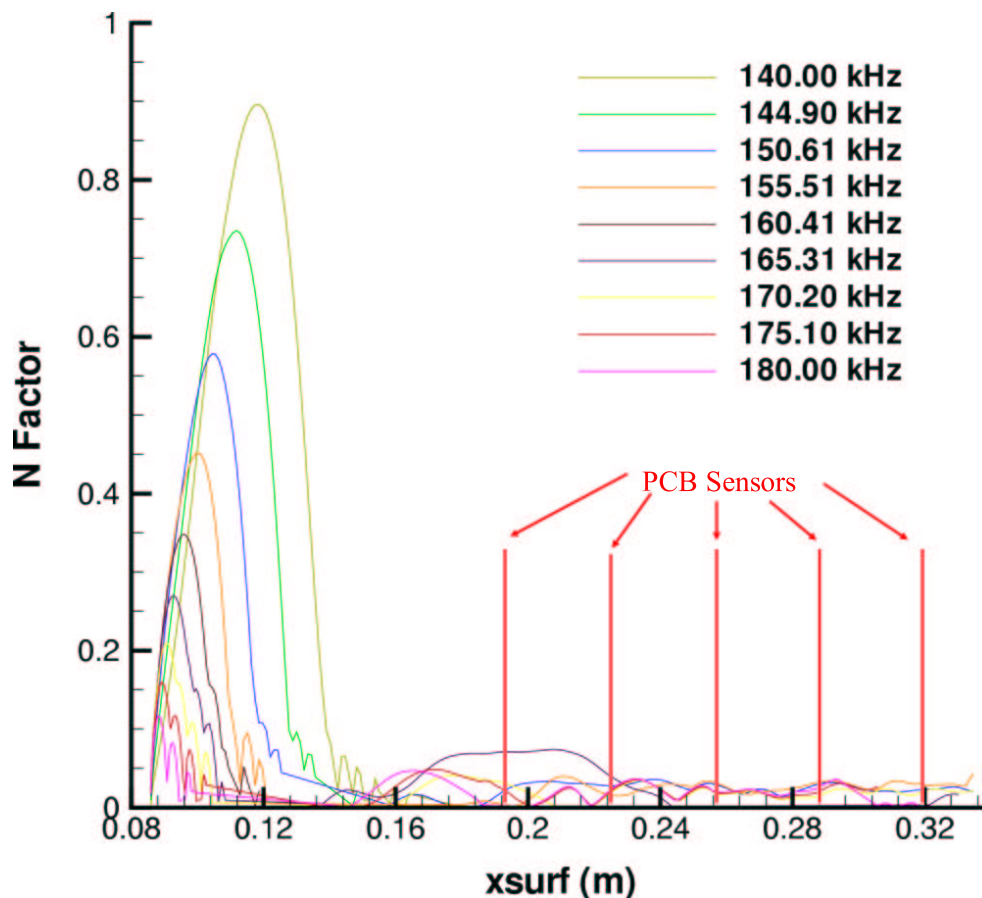


Figure 5.25: N factors vs.  $x$  for frequencies between 140 and 180 kHz (from [75])

a function of arclength for an unstable first-mode instability wave with a frequency of 30 kHz and a wave angle of  $550 \text{ m}^{-1}$ . Although the solution suffers from some numerical problems, evidenced by the jaggedness, the general trend is clear. The first mode is unstable at  $x=3 \text{ cm}$  (1.2 in.) for a frequency of 30 kHz, and remains unstable to about  $x=28 \text{ cm}$  (11.0 in.). Thus, a 30 kHz disturbance created by the glow perturber at  $x=8.8 \text{ cm}$  (3.46 in.) would reasonably be expected to be unstable and grow from the glow perturber to the two locations that the waves were detected by the hot wire,  $x=16.8$  and  $21.6 \text{ cm}$  (6.6 and 8.5 in.). They should also have been present for at least the three upstream PCB sensors located at  $x=19.3$ ,  $22.5$ , and  $25.7 \text{ cm}$  (7.6, 8.9, and 10.1 in.). However, as discussed in Section 1.2, Ref. 26 reports



that pressure fluctuations for a first-mode instability wave are very small. Thus, it is not at all surprising that a 30 kHz first-mode wave introduced at the glow perturber was present and measured with the hot wires, but not detected by the PCB sensors.

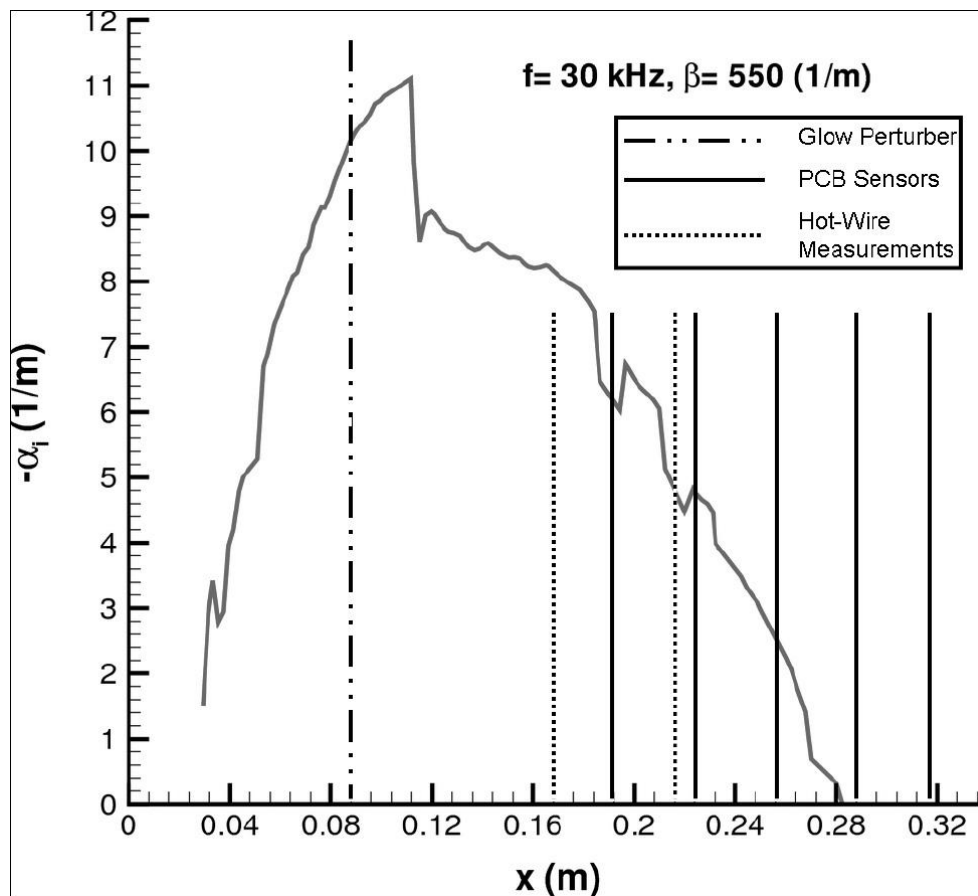


Figure 5.26: Amplification rate for 30 kHz first-mode instability (from [75])

Apart from the disturbance frequencies agreeing, it would be instructive to compare another experimental quantity to the computations to verify that the flow physics have been properly modeled. To this end, a hot wire was calibrated for mass flux according to the method reported in Section 3.2. It was traversed through the boundary layer at a streamwise station of  $x = 27.1 \text{ cm}$  (10.7 in.). In this case, the wire started moving 500 ms after the oscilloscopes triggered. The wire moved from a height  $y = 4.8 \text{ mm}$  (0.19 in.) to  $y = 0.8 \text{ mm}$  (0.03 in.) in  $0.20 \text{ mm}$  (0.008 in.) increments. The

wire was held at each vertical station for 100 ms. The mean bridge voltage was computed each time the wire was held stationary. The calibration was then applied to the raw voltage to convert it to mass flux. Finally, computed mass flux is plotted against the known wire position.

Figure 5.27 shows both the experimentally measured and the computed boundary layer profiles. The general shape of both is the same. However, the actual values of mass flux are considerably offset from each other. The computed boundary layer also appears to be less thick than what is seen in the experiments. The most likely explanation for this is that the boundary layer was turbulent at  $x=27.1$  cm (10.7 in.). This was the conclusion from both TSP and PCB data. Unfortunately, due to an oversight, this discrepancy was not realized until well after the tunnel entry was complete.

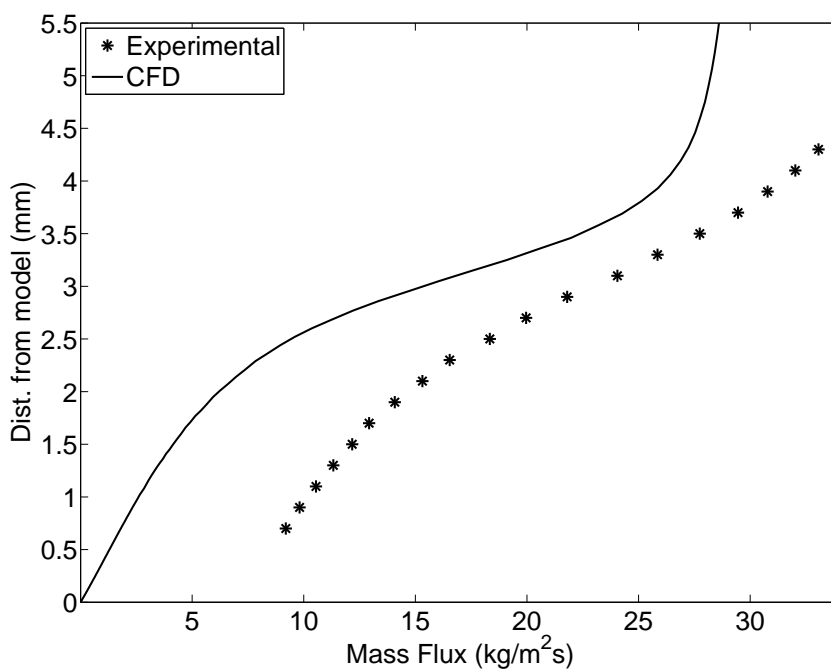


Figure 5.27: Experimental and computed boundary-layer profile

## 5.6 Leading-Edge Roughness Effects

It is well-known that small variations in the leading edge shape of a hypersonic vehicle can have a large impact on the flow downstream. In an effort to better understand the effect of tunnel noise coupled with leading edge roughness, a series of experiments was conducted by varying the thicknesses and locations of small roughness elements placed on the leading edge of the model under both noisy and quiet conditions. It is thought that any variations in the leading edge of the X-51A could cause a perturbation in the leading edge shock. This would introduce streamwise vorticity into the flow, destabilizing the boundary layer and possibly leading to early transition. Given the complex, 3-dimensional geometry of the leading edge of the X-51A, it was unknown whether a particular size of leading edge roughness would equally affect the flow on and off the centerline. All experiments with leading-edge roughness had an initial stagnation pressure of 620.5 kPa (90 psia).

Roughness elements were added to the leading edge by wrapping a piece of  $k=0.05$  mm (0.002 in.) thick tape around the leading edge. The tape pieces were generally about 1.0 mm (0.04 in.) wide and 3.3 mm (0.13 in.) long on the leeward side of the model. The model's leading edge has a radius of approximately 0.25 mm (0.01 in.), as measured with a micrometer. Figures 5.28a-5.28c show surface temperatures for  $k=0.00$ , 0.05, 0.10 mm (0.000, 0.002, and 0.004 in.) on the centerline leading edge under noisy conditions. Figure 5.28d shows the streamwise temperature along the model centerline. It is clear from the figures that the addition of one roughness element,  $k=0.05$  mm(0.002 in.), on the model centerline had almost no effect on the flow. When the roughness height was doubled to  $k=0.10$  mm (0.004 in.), however, the difference is clearly discernible. A high-temperature streak that broadens downstream is seen along the centerline. It is thought that the streak is a region of turbulent flow behind the leading-edge roughness. As is expected of a turbulent region, its spanwise extent broadens downstream. Also, since the streamwise centerline temperature

decreases downstream, it seems likely that along the centerline there is a thickening turbulent boundary layer.

It is somewhat surprising that a roughness element with a thickness about 20% of the leading edge radius has almost no effect on the state of the boundary layer. Perhaps this is due to the higher model thickness along the centerline (seen in Figure 2.4d).

### 5.6.1 Effect of Tunnel Noise on Leading-Edge Roughness

Additional experiments examined the effect of freestream noise on transition induced by leading-edge roughness at varying spanwise locations. It was also hoped that the locations and spreading of any vortices shed by the roughness elements could help determine the extent of outward-directed crossflow. Experiments were conducted with roughness elements on the leading edge, from the centerline at  $z'=0.0$  cm (0.0 in.) through  $z'=20.3$  mm (0.8 in.) in 2.5 mm (0.1 in.) increments. Here,  $z'$  is the approximate arclength along the curved leading edge. Positive  $z'$  values are on the starboard half of the model. Two roughness locations were always used simultaneously. For instance, in a single run, one roughness element was placed at  $z'=-7.6$  mm (-0.3 in.) and another was placed at  $z'=10.2$  mm (0.4 in.). Due to model symmetry, it was assumed that this was a reasonable practice. In all cases that will be shown, the roughness element located farthest away from the centerline was on the half of the model denoted by positive spanwise distances, the starboard side. Figures 5.29 and 5.30 shows surface temperatures for each roughness condition under both noisy and quiet conditions. Figure 5.31 shows spanwise temperatures at a streamwise location of 15.0 cm (5.9 in.) for both conventional and low noise levels.

The effects of both the leading-edge roughnesses and freestream noise are immediately evident. For the quiet noise-level cases, there are no evident streamwise streaks when a  $k=0.10$  mm (0.004 in.) roughness was located at  $z'=0.0$  mm (0.0 in.) When the roughnesses were located at  $z'=2.5$  and 5.1 mm (-0.1 and 0.2 in.), only very faint

streaks can be seen. They are seen as two small peaks in Figure 5.31a. The upstream outboard temperatures are also slightly elevated from the no roughness case. For  $z'=-7.6$  and  $10.2$  mm (-0.3 and 0.4 in.) and  $z'=12.7$  and  $15.2$  mm (-0.5 and 0.6 in.), at least two streamwise streaks are evident. These are assumed to be streamwise vortices shed by the leading-edge roughness elements. They also bend away from the centerline. This demonstrates the presence of significant outward-directed crossflow. Such crossflow would tend to transport low-momentum fluid away from the centerline. This has the effect of thinning and stabilizing the boundary layer there.

For  $z'=-17.8$  and  $20.3$  mm (-0.7 and 0.8 in.), one streak is evident at about  $z=-27.9$  mm (-1.1 in.), but it quickly washes off the nylon insert. It is caused by the roughness at  $z'=-25.4$  mm (-0.7 in.). No streak is seen associated with the roughness at  $z'=20.3$  mm (0.8 in.). Thus, a total leading-edge arclength of 35.6-40.6 mm (1.4-1.6 in.) captures all the fluid flowing over the 61.0 mm (2.4 in.)-wide nylon insert. With so much outward-directed crossflow, it seems reasonable to suspect that the crossflow instability may be present and may further destabilize the boundary layer. This could explain the elevated temperatures observed there under both noisy and quiet conditions with no leading-edge roughness.

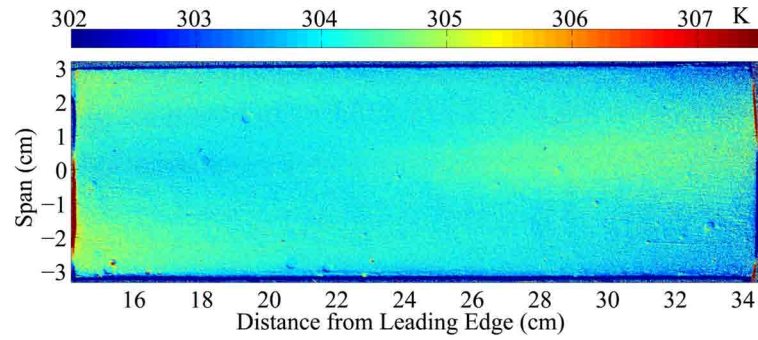
It does not appear that any of the streamwise vortices break down into turbulence under quiet conditions. Instead, the high-temperature streaks due to the vortices either fade downstream or are washed off of the nylon surface. The streaks do not show any spreading, which would be expected if they caused transition of the boundary layer.

Under conventional freestream noise levels, the leading-edge roughness had a much greater effect. For instance, for  $z'=2.5$  and  $5.1$  mm (-0.1 and 0.2 in.), two vortex streaks are evident at the upstream end of the nylon. The vortex corresponding to the roughness at  $z'=-2.5$  mm (-0.1 in.) begins to spread in the spanwise direction at about  $x=20$  cm (7.9 in.). The streak associated with the roughness at  $z'=5.1$  mm (0.2 in.) begins spreading in the spanwise direction by about  $x=17$  cm (6.7 in.). As evidenced by the spanwise spreading and increased temperatures, both vortices appear to break

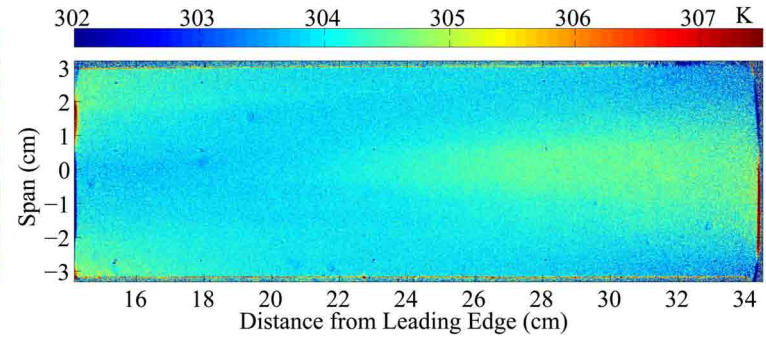
down into turbulent flow and merge with the natural centerline transitional region that is observed even in the absence of leading-edge roughness. As in the low noise case, as the leading-edge roughnesses are moved outboard, the vortices observed on the nylon move outboard as well. Tunnel noise does not seem to have an effect on the location of the vortices as they appear in the same location on the nylon under both quiet and noisy conditions. They also wash outward in the same manner. These trends are seen in both the surface temperature distributions and also the spanwise temperature plots. The vortices are seen as peaks in the spanwise temperature. The spanwise temperature peaks caused by the vortices are generally somewhat larger under conventional noise levels than under quiet conditions, particularly closer to the centerline. References 36 and 37 also demonstrated this effect of tunnel noise on roughness induced transition.

The fact that the vortices do not break down to turbulence under low-noise conditions, but do break down under conventional noise levels is significant. This suggests that higher initial-amplitude disturbances in the boundary layer couple with disturbances from the leading-edge roughness to destabilize the boundary layer and promote earlier transition than is seen under the low-noise levels of flight.

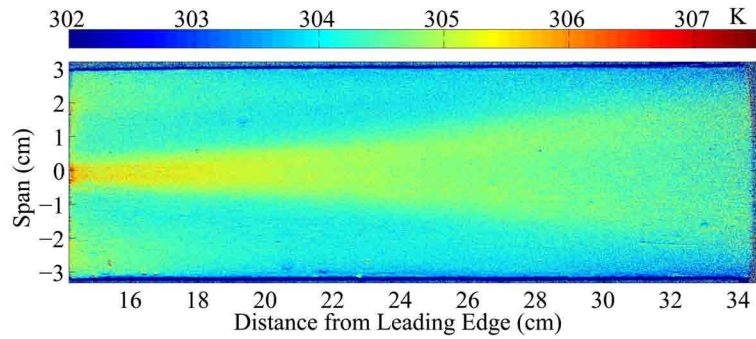
At 620.5 kPa (90 psia) ( $Re \approx 6.6 \times 10^6/m, 2 \times 10^6/ft$ ) under quiet freestream noise levels, it appears that leading edge roughness with a thickness on the order of 40% of the leading edge radius does not induce transition on the model's leeward surface. With conventional noise levels, a roughness with this height is sufficient to trip the boundary layer, while a roughness 20% of the leading edge radius is not. Off-center roughnesses on the order of 20% of the leading edge radius all appeared to induce transition on the model under conventional noise levels, but only generated streamwise vortices in quiet flow. It appears that, under both low and conventional freestream noise levels, the boundary layer is much less sensitive to leading-edge roughness on the centerline than locations as little as 2.5 mm (0.1 in.) off of the centerline. This is likely due to the stabilizing effect of the crossflow transport of low-momentum fluid away from the centerline as well as the thicker leading edge on the centerline.



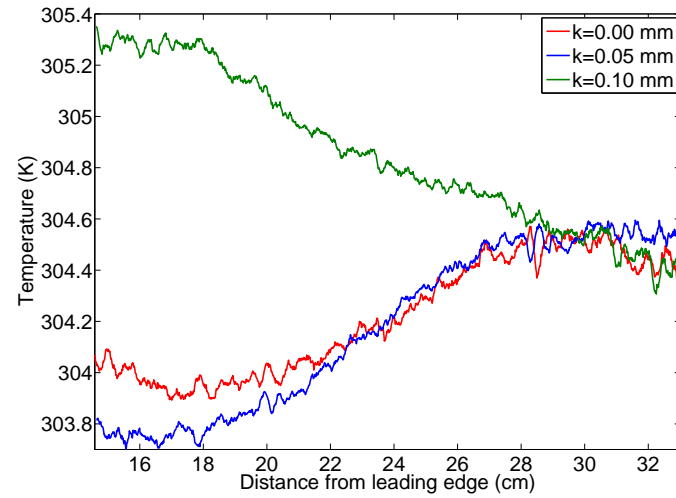
(a)  $k=0.00$  mm



(b)  $k=0.05$  mm



(c)  $k=0.10$  mm



(d) Centerline temperatures

Figure 5.28: Surface temperature distribution and streamwise centerline temperatures under noisy conditions for  $k=0.00$ ,  $0.05$ , and  $0.10$  mm ( $0.000$ ,  $0.002$ , and  $0.004$  in.)

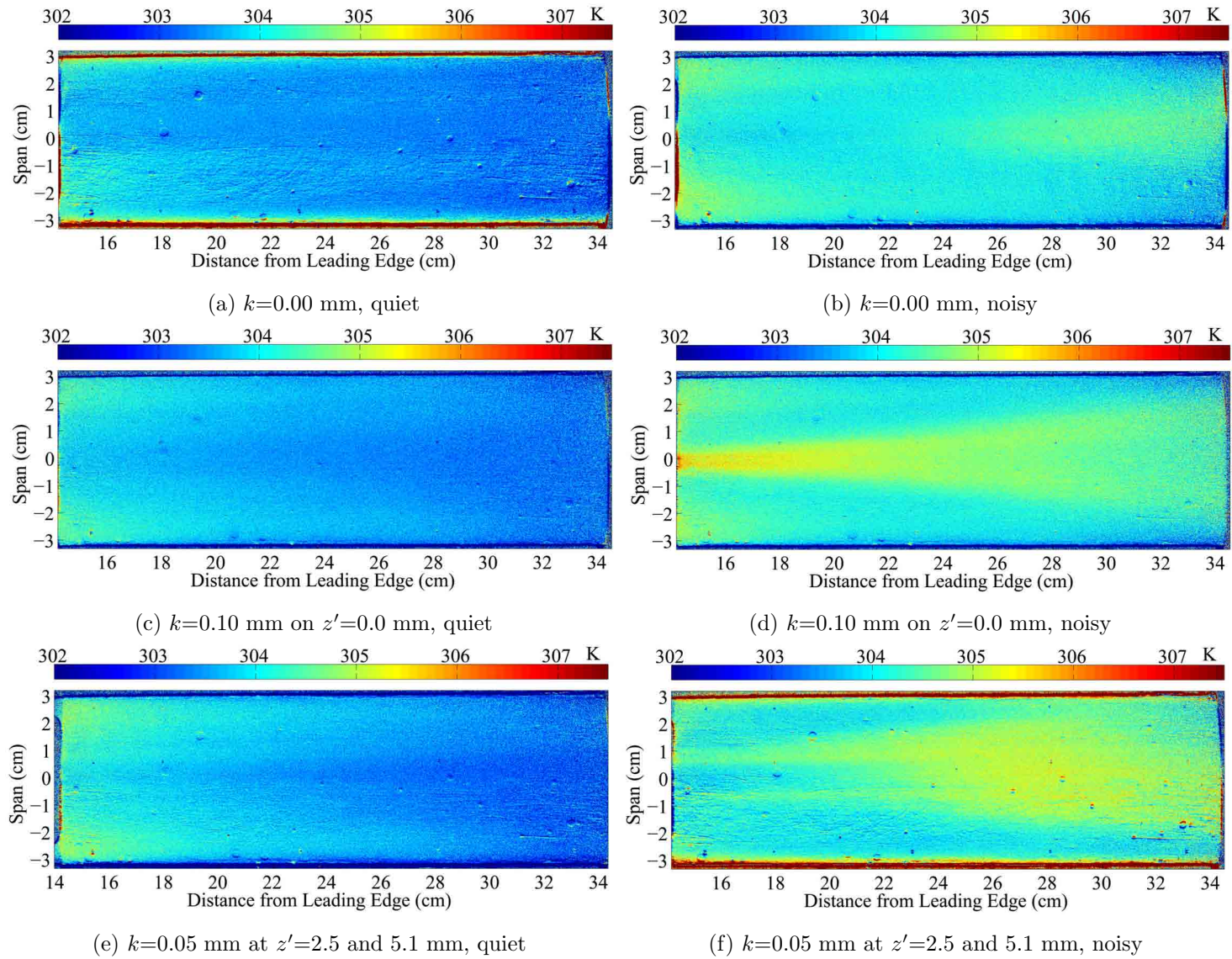


Figure 5.29: Part 1: Surface temperature (K) distribution under quiet and noisy conditions with leading-edge roughness



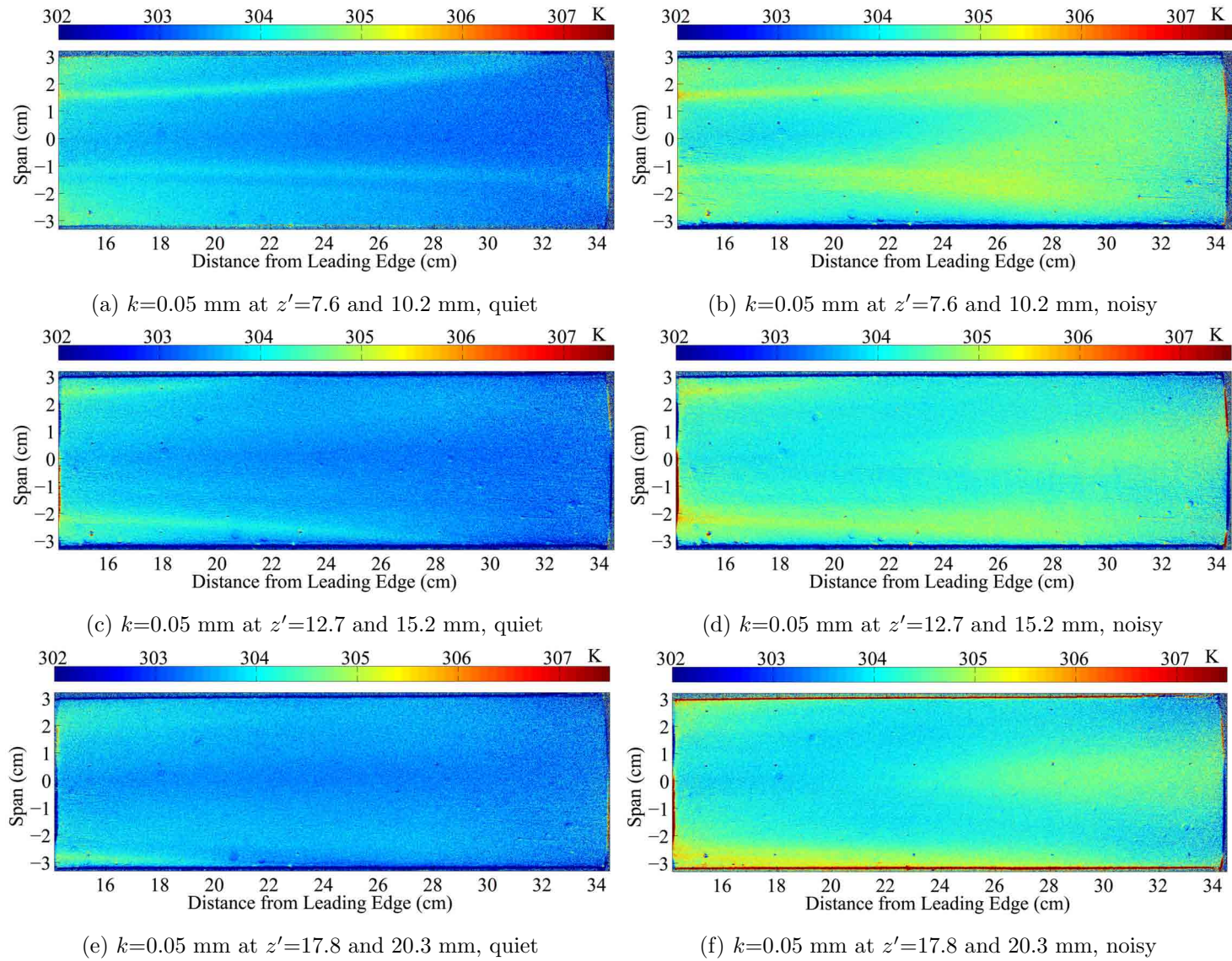


Figure 5.30: Part 2: Surface temperature (K) distribution under quiet and noisy conditions with leading-edge roughness

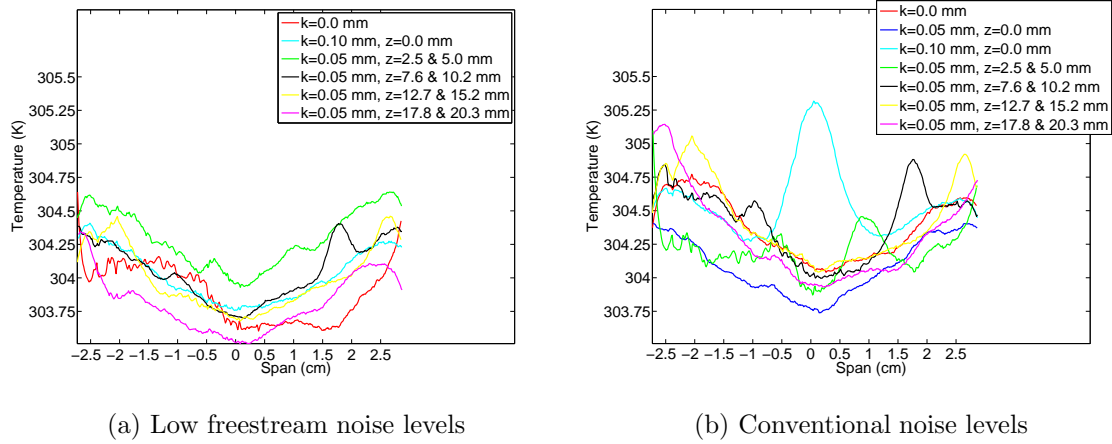


Figure 5.31: Spanwise temperature distributions at  $x=15.0$  cm, quiet and noisy flow for leading edge roughness

## 6. CONCLUSIONS AND FUTURE WORK

### 6.1 Conclusions

It is well known that tunnel noise can have a profound effect on transition. A few previous experiments have shown an effect of tunnel noise on roughness-induced transition. The effect of tunnel noise on natural and roughness-dominated transition was clearly seen on the 20%-scale X-51A forebody model in the BAM6QT. On the smooth model, reducing freestream noise from conventional to quiet levels increased the transition Reynolds number based on freestream conditions and length from the nose by a factor of at least 2.2. With the  $k_{max}=0.76$ -mm (0.030 in.) ramp roughness strip the transition Reynolds number increased by a factor of 2.4. The  $k_{max}=0.38$ -mm (0.015 in.) ramp roughness were not as effective in tripping the boundary layer as the larger  $k_{max}=0.76$ -mm (0.030 in.) ramps. Additionally, for the highest Reynolds number tested,  $Re_t$  was increased by a factor of 3.1 when freestream noise levels dropped from conventional to low levels. Reducing freestream noise increased the transition Reynolds number by a factor of 1.7 for the  $k=1.52$  mm (0.060 in.) diamond trips. To the author's knowledge, the present work reports the first hypersonic measurements of roughness-induced transition under low noise levels that are comparable to flight, using reasonably-sized trips, at high freestream Reynolds number.

Hot wires, TSP, and PCB pressure sensors were used to characterize transition trends and the instability mechanisms present on the leeward side of the X-51A forebody. With low noise levels, no transition was observed with discrete roughness elements of height  $k=0.10$  mm (0.004 in.) wrapped around the leading edge on the centerline and  $k=0.05$  mm (0.002 in.) elements wrapped around the leading edge off center. With conventional noise, vortices shed from the roughnesses broke down to turbulence.

Using the PCB pressure sensors, disturbances near 100 kHz were found to grow both with downstream distance and also increasing Reynolds number for conventional noise levels. Under quiet conditions, they grew with downstream distance. After the 100 kHz disturbances reached amplitudes of about 3% of the surface pressure, transition onset was confirmed both by a rise in surface temperature, and also a broadening of the spectra. The frequency of the disturbances matched well with those predicted by STABL. Thus, it seems likely that the disturbances are due to the second mode instability. The data suggest that transition on the lee side is at least impacted by the growth and breakdown of second-mode waves. The presence of other instability mechanisms is suspected. Their classification and interactions with each other and the second mode instability was beyond the scope of the current work. Conventional freestream noise levels were observed to promote early transition when compared to low noise levels. Lee side transition was not observed at even the highest unit Reynolds number providing quiet flow.

STABL computations also explain the lack of any significant effect of the glow perturber. The neutral curve near the glow perturber is such that any disturbances created there would damp out by the time they reached the PCB sensors. Thus, no disturbance created by the glow perturber should have been observed at the PCB sensors. The lack of observable waves in the experimental data supports the computations.

Freestream noise was found to promote early transition for roughness-induced transition on the windward surface, leading-edge-roughness-induced transition on the leeward surface, and smooth-wall natural transition on the leeward surface.

## 6.2 Suggestions for Future Work

The boundary layers for the X-51A are three dimensional and complicated. There are many possible instability mechanisms that contribute to the transition process. Further work should be undertaken to examine the physical mechanisms responsible

for the X-51A and other similar hypersonic vehicles. As the underlying flow physics become better understood, the prediction methods will grow more robust and reliable, and significantly improve the design of hypersonic vehicles.

Using hot wires and possibly the PCB sensors on the windward surface of the model to study natural transition there could be very useful. It was observed that transition occurred there in the absence of any trips with conventional noise levels. With low freestream noise levels, transition was not observed. If the dominant natural instability mechanism there could be determined, perhaps it could be further excited without the need for drag-increasing trips.

It would be a clear advantage to develop the PCB sensors and techniques. Calibrating the sensors would allow more accurate wave amplitudes to be found. Accurate  $N$  factors could then be measured and compared to computations. It would also be a good idea to use one PCB sensor and install it at different streamwise stations, making measurements at the same tunnel conditions. This would remove the effect of sensor-to-sensor variations, and help to more accurately determine disturbance amplitudes.

Calibrated profiles of laminar boundary layers should be measured with hot wires at several streamwise stations and compared to computations to further ensure the trustworthiness of the computations. Hot wire measurements should also be made closer to the wall to see if the 100 kHz oscillations can be measured by more than just the PCB sensors.

If the hot wires can detect naturally occurring second-mode disturbances in the boundary layer, they should also be able to determine the mode shape and phase velocity by measuring at multiple distances from the wall for constant streamwise station. This could more conclusively classify the 100 kHz disturbances as the second-mode instability.

Further effort should also be made to understand the cause of the 320 kHz disturbances detected by the PCB sensors. If those disturbances are due to some unidentified instability, the computations did not model it. This avenue should be pursued. If

the glow perturber could be modified to operate at 320 kHz, the effect of disturbances at 320 kHz on the transition process and any interaction with the 100 kHz second mode disturbance could be observed.

Additionally, for the X-51A, the glow perturber should be moved downstream to  $x=24$  cm (9.4 in.). This is the approximate streamwise location where the second mode instability at 100 kHz first becomes unstable. Moving the glow perturber to this location should allow the glow-caused disturbances to be detected and grow under low freestream noise conditions. These measurements can then be compared to computations. If good agreement is found, the X-51A data could serve as a good set of validation experiments for a complex, three-dimensional geometry modeled by STABL and other stability solvers. If the codes can accurately capture the complex flow physics involved here, it validates that the physical modeling is correct.

Lastly, it would be good to examine the extent and effect of the outward-directed crossflow observed and computed on the lee side of the X-51A. Although the second mode appears to be the dominant instability here, it seems likely that crossflow has some effect on the stability of the boundary layer. This almost certainly also has implications for the boundary layer on the lateral sides of the vehicle. This portion of the boundary layer was not examined at all in the present investigation.

## LIST OF REFERENCES

## LIST OF REFERENCES

- [1] Kenneth F. Stetson and Roger L. Kimmel. On hypersonic boundary-layer stability. Paper 92-0737, AIAA, January 2004.
- [2] Leslie M. Mack. Linear stability and the problem of supersonic boundary-layer transition. *AIAA Journal*, 13(3):278–289, 1975.
- [3] Kenneth F. Stetson and Roger L. Kimmel. Example of second-mode instability dominance at a Mach number of 5.2. *AIAA Journal*, 30(12):2974–2976, 1992.
- [4] Thorwald Herbert. Secondary instability of boundary layers. *Annual Review of Fluid Mechanics*, 20:487–526, 1988.
- [5] Kenneth F. Stetson. On nonlinear aspects of hypersonic boundary-layer stability. *AIAA Journal*, 26(7):883–885, 1988.
- [6] Alexander N. Shipliyuk, Dimitry A. Bountin, and Anatoly A. Maslov. Nonlinear interactions of second mode instability with natural and artificial disturbances. Paper 2003-0787, AIAA, January 2003.
- [7] Eli Reshotko. Is  $Re_\theta/M_e$  a meaningful transition criterion? *AIAA Journal*, 45(7):1441–1443, 2007.
- [8] Heath B. Johnson and Graham V. Candler. Hypersonic boundary layer stability analysis using PSE-Chem. Paper 2005-5023, AIAA, June 2005.
- [9] N.A. Jaffe, T.T. Okamura, and A.M.O. Smith. Determination of spatial amplification factors and their application to predicting transition. *AIAA Journal*, 8(2):301–308, 1970.
- [10] F.-J. Chen, M.R. Malik, and I.E. Beckwith. Boundary-layer transition on a cone and flat plate at Mach 3.5. *AIAA Journal*, 27(6):687–693, 1989.
- [11] M.R. Malik. Hypersonic flight transition data analysis using parabolized stability equations with chemistry effects. *Journal of Spacecraft and Rockets*, 40(3):332–344, May-June 2003.
- [12] T.J. Horvath, S.A. Berry, B.R. Hollis, C.-L. Chang, and B.A. Singer. Boundary layer transition on slender cones in conventional and low disturbance Mach 6 wind tunnels. AIAA Paper 2002-2743, January 2002.
- [13] H.B. Johnson, T.G. Seipp, and G.V. Candler. Numerical study of hypersonic reacting boundary layer transition on cones. *Physics of Fluids*, 10(10):2676–2685, October 1998.
- [14] M.R. Malik, R.E. Spall, and C.-L. Chang. Effect of nose bluntness on boundary layer stability and transition. AIAA Paper 90-0112, January 1990.



- [15] J. Stilla. Engineering transition prediction for a hypersonic axisymmetric boundary layer. *Journal of Aircraft*, 31(6):1358–1364, 1994.
- [16] John Laufer and Thomas Vrebalovich. Stability and transition of a supersonic laminar boundary layer on an insulated flat plate. *Journal of Fluid Mechanics*, 9(2):257–299, 1960.
- [17] Anthony Demetriades. An experiment on the stability of hypersonic boundary layers. *Journal of Fluid Mechanics*, 7(3):385–396, 1960.
- [18] Anthony Demetriades. Hypersonic viscous flow over a slender cone. Paper 74-535, AIAA, June 1974.
- [19] J.M. Kendall. Wind tunnel experiments relating to supersonic and hypersonic boundary-layer transition. *AIAA Journal*, 13(3):290–299, 1975.
- [20] Shann J. Rufer. *Hot-wire measurements of instability waves on sharp and blunt cones at Mach-6*. Ph.D. dissertation, Purdue University (West Lafayette), December 2005.
- [21] Shann J. Rufer and Steven P. Schneider. Hot-wire measurements of instability waves on cones at Mach 6. Paper 2006-3054, AIAA, June 2006.
- [22] Keisuke Fujii. Experiment of the two-dimensional roughness effect of hypersonic boundary-layer transition. *Journal of Spacecraft and Rockets*, 43(4):731–738, 2006.
- [23] Malte Estorf, Rolf Radespiel, Steven P. Schneider, Heath B. Johnson, and Stefan Hein. Surface-pressure measurements of second-mode instability in quiet hypersonic flow. Paper 2008-1153, AIAA, January 2008.
- [24] Tanno Hideyuki, Komuro Tomoyuki, Sato Kazuo, Itoh Katsuhiro, Takahashi Masahiro, and Fujii Keisuke. Measurement of hypersonic boundary layer transition on cone models in the free-piston shock tunnel HIEST. AIAA Paper 2009-781, January 2009.
- [25] Katya M. Casper, Steven J. Beresh, John F. Henfling, Russell W. Spillers, Brian Pruett, and Steven P. Schneider. Hypersonic wind-tunnel measurements of boundary-layer pressure fluctuations. Paper 2009-4054, AIAA, June 2009.
- [26] Helmut Knauss, Tim Roediger, and Julio Srulijes. Novel sensor for fast heat-flux measurements. *Journal of Spacecraft and Rockets*, 46(2):255–265, March-April 2009.
- [27] Yu. P. Raizer. *Gas Discharge Physics*. Springer, New York, NY, 1997.
- [28] Dale W. Ladoon and Steven P. Schneider. Instability and transition experiments at Mach 4 using an electrical-discharge perturber. Paper FEDSM97-3112, ASME Fluids Engineering Division Summer Meeting, June 1997.
- [29] Dale W. Ladoon and Steven P. Schneider. Measurements of controlled wave packets at Mach 4 on a cone at angle of attack. Paper 98-0436, AIAA, January 1998.

- [30] Anatoly A. Maslov, Alexander N. Shplyuk, Dimitry A. Bountin, and Andrey A. Sidorenko. Mach 6 boundary-layer stability experiments on sharp and blunted cones. *Journal of Spacecraft and Rockets*, 43(1):71–76, 2006.
- [31] A.J. Laderman. Review of wind-tunnel freestream pressure fluctuations. *AIAA Journal*, 15(4):605–608, April 1977.
- [32] Steven P. Schneider. Effects of high-speed tunnel noise on laminar-turbulent transition. *Journal of Spacecraft and Rockets*, 38(3):323–333, May-June 2001.
- [33] Helen L. Reed, Roger Kimmel, Steven Schneider, and Daniel Arnal. Drag prediction and transition in hypersonic flow. Paper 97-1818, AIAA, June 1997.
- [34] S.R. Pate and C.J. Schueler. Radiated aerodynamic noise effects on boundary-layer transition in supersonic and hypersonic wind tunnels. *AIAA Journal*, 7(3):450–457, 1969.
- [35] Takeshi Ito, Laura A. Randall, and Steven P. Schneider. Effect of noise on roughness-induced boundary-layer transition for scramjet inlet. *Journal of Spacecraft and Rockets*, 38(5):692–698, 2001.
- [36] Matthew P. Borg and Steven P. Schneider. Effect of freestream noise on roughness-induced transition for the X-51A forebody. *Journal of Spacecraft and Rockets*, 45(6):1106–1116, November-December 2008.
- [37] Katya M. Casper, Brad M. Wheaton, Heath B. Johnson, and Steven P. Schneider. Effect of freestream noise on roughness-induced transition at Mach 6. Paper 2008-4291, AIAA, June 2008.
- [38] John Laufer. Aerodynamic noise in supersonic wind tunnels. *Journal of the Aerospace Sciences*, 28(9):685–692, 1961.
- [39] Steven P. Schneider. Fabrication and testing of the Purdue Mach-6 quiet-flow Ludwig tube. Paper 2000-0295, AIAA, January 2000.
- [40] Steven P. Schneider. Design and fabrication of a 9.5-inch Mach-6 quiet-flow Ludwig Tube. Paper 98-2511, AIAA, June 1998.
- [41] Craig R. Skoch. Final assembly and initial testing of the Purdue Mach-6 quiet-flow Ludwig tube. M.S. thesis, Purdue University (West Lafayette), December 2001. School of Aeronautics and Astronautics.
- [42] Michael J. Hannon Jr. Evaluation of diffuser modifications for the Boeing/AFOSR Mach-6 quiet tunnel. M.S. thesis, Purdue University (West Lafayette), December 2007. School of Aeronautics and Astronautics.
- [43] Thomas J. Juliano, Rodrigo Segura, Matthew P. Borg, Katya M. Casper, Jr. Michael J. Hannon, Brad M. Wheaton, and Steven P. Schneider. Starting issues and forward-facing cavity resonance in a hypersonic quiet tunnel. Paper 2008-3735, AIAA, June 2005.
- [44] Steven P. Schneider. Development of hypersonic quiet tunnels. *Journal of Spacecraft and Rockets*, 45(4):641–664, 2008.

- [45] Joseph M. Hank, James S. Murphy, and Richard C. Mutzman. The X-51A scramjet engine flight demonstration program. AIAA Paper 2008–2540, April 2008.
- [46] T. Liu and J.P. Sullivan. *Pressure and temperature sensitive paints*. Springer, New York, NY, 2005.
- [47] L.N. Cattafesta III, T. Liu, and J.P. Sullivan. Uncertainty estimates for temperature-sensitive paint measurements with charge-coupled device cameras. *AIAA Journal*, 36(11):2102–2108, 1998.
- [48] Tianshu Lui, B.T. Campbell, S.P. Burns, and J.P. Sullivan. Temperature- and pressure-sensitive luminescent paints in aerodynamics. *Applied Mechanics Reviews*, 50(4):227–246, April 1997.
- [49] Uwe Fey, Yasuhiro Egami, and Rolf H. Engler. High Reynolds number transition detection by means of temperature sensitive paint. AIAA Paper 2006-514, January 2006.
- [50] Marvine Hamner, Christopher A. Kelble, Lewis R. Owens, and Jr. Thomas G. Popernack. Application of temperature sensitive paint technology to boundary layer analysis. AIAA Paper 97-5536, October 2008.
- [51] Shin Matsumura, Steven P. Schneider, and Scott A. Berry. Streamwise vortex instability and transition on the Hyper-2000 scramjet forebody. *Journal of Spacecraft and Rockets*, 42(1):78–89, 2001.
- [52] Erick O. Swanson. *Boundary-layer transition on cones at angle of attack in a Mach-6 quiet tunnel*. Ph.D dissertation, Purdue University (West Lafayette), August 2008. School of Aeronautics and Astronautics.
- [53] A. Neal Watkins, Gregory M. Buck, Bradley D. Leighty, William E. Lipford, and Donald M. Oglesby. Using pressure- and temperature-sensitive paint on the afterbody of a capsule vehicle. *AIAA Journal*, 47(4):821–829, April 2009.
- [54] Inna Kurits and Mark J. Lewis. Global temperature-sensitive paint system for heat transfer measurements in long-duration hypersonic flows. *Journal of Thermophysics and Heat Transfer*, 23(2):256–266, April-June 2009.
- [55] B.T. Campbell, T. Liu, and J.P. Sullivan. Temperature sensitive fluorescent paint systems. Paper 94-2483, AIAA, June 1994.
- [56] Shin Matsumura, Steven P. Schneider, and Scott A. Berry. Flow visualization measurement techniques for high-speed transition research in the Boeing/AFOSR Mach-6 tunnel. AIAA Paper 2003–4583, July 2003.
- [57] P.C. Stainback and K.A. Nagabushana. Review of hot-wire anemometry techniques and the range of their applicability for various flows. *American Society of Mechanical Engineers, Fluids Engineering Division FED, Thermal Anemometry 1993*, v 167:93–133, 1993. Information for this document was taken from an extended version of this paper of the same title in an electronic version of the *Journal of Fluids Engineering*.
- [58] E.F. Spina and C.B. McGinley. Constant-temperature anemometry in hypersonic flow: critical issues and sample results. *Experiments in Fluids*, 17:365–374, 1994.

- [59] L.M. Fingerson and Peter Freymuth. *Fluid Mechanics Measurements*, chapter 3, Thermal Anemometers. Taylor & Francis, 1996.
- [60] A.J. Smits, K. Hayakawa, and K.C. Muck. Constant temperature hot-wire anemometer practice in supersonic flows. *Experiments in Fluids*, pages 83–92, 1983.
- [61] Steven P. Schneider, Steven H. Collicott, J. D. Schmisser, Dale Ladoon, Laura A. Randall, Scott E. Munro, and T. R. Salyer. Laminar-turbulent transition research in the Purdue Mach-4 Quiet-Flow Ludwig Tube. Paper 96-2191, AIAA, June 1996.
- [62] Kei Lau. Private Communication, July 2009.
- [63] Scott A. Berry, Aaron H. Auslender, Arthur D. Dilley, and John F. Calleja. Hypersonic boundary-layer trip development for Hyper-X. *Journal of Spacecraft and Rockets*, 38(6):853–864, 2001.
- [64] Steven P. Schneider, Shin Matsumura, Shann Rufer, Craig Skoch, and Erick Swanson. Hypersonic stability and transition experiments on blunt cones and a generic scramjet forebody. Paper 2003-1130, AIAA, January 2003.
- [65] J.D. Schmisser, J.O. Young, and Steven P. Schneider. Measurements of boundary-layer transition on the flat sidewall of a rectangular Mach 4 quiet-flow nozzle. AIAA Paper 96-0852, January 1996.
- [66] G. Simeonides and W. Hasse. Experimental and computational investigations of hypersonic flow about compression ramps. *Journal of Fluid Mechanics*, 283:17–42, 1995.
- [67] Roger L. Kimmel, James R. Hayes, Jim W. Crafton, Sergey D. Fonov, James Menart, and Joseph Shang. Surface discharges for high-speed boundary layer control. Paper 2006-710, AIAA, January 2006.
- [68] Karen T. Berger, Frank A. Greene, Roger Kimmel, Christopher Alba, and Heath Johnson. Aerothermodynamic testing and boundary-layer trip sizing of the HI-FiRE flight 1 vehicle. *Journal of Spacecraft and Rockets*, 45(6):1117–1124, 2008.
- [69] Karen T. Berger. Aerothermodynamic testing of the crew exploration vehicle in the LaRC 20-inch Mach 6 and 31-inch Mach 10 tunnels. Paper 2008-1225, AIAA, January 2008.
- [70] Adam Amar, Thomas J. Horvath, Brian R. Hollis, Karen T. Berger, Scott A. Berry, and Nathan Calvert. Protuberance boundary layer transition for project orion crew entry vehicle. Paper 2008-1227, AIAA, January 2008.
- [71] Steven P. Schneider. Hypersonic laminar-turbulent transition on circular cones and scramjet forebodies. *Progress in Aerospace Sciences*, 40:1–50, 2004.
- [72] Shann Rufer and Steven P. Schneider. Hot-wire measurements of instability waves at Mach 6. AIAA Paper 2006-3054, June 2006.
- [73] Craig R. Skoch, Steven P. Schneider, and Matthew P. Borg. Disturbances from shock/boundary layer interactions affecting upstream hypersonic flow. Paper 2005-4897, AIAA, June 2005.

- [74] Steven P. Schneider. Effects of roughness on hypersonic boundary-layer transition. *Journal of Spacecraft and Rockets*, 45(2):193–209, March-April 2008.
- [75] Chris Alba. Private Communication, January-July 2009.
- [76] Craig R. Skoch. *Disturbances from Shock/Boundary-Layer Interactions Affecting Upstream Hypersonic Flow*. PhD thesis, Purdue University (West Lafayette), December 2005. School of Aeronautics and Astronautics.
- [77] Mazen Abdel-Salam, Hussein Anis, Ahdab El-Morshedy, and Roshdy Radwan. *High-Voltage Engineering: Theory and Practice*. Marcel Dekker, Inc., New York, NY, 2000.
- [78] Shin Matsumura, February 2008. Private communication.
- [79] Dale W. Ladoon. *Wave Packets Generated by a Surface Glow Discharge on a Cone at Mach 4*. Ph.D dissertation, Purdue University (West Lafayette), December 1998. School of Aeronautics and Astronautics.

## APPENDICES

## A. RUN CONDITIONS

The following table lists the figure number, stagnation conditions and freestream Reynolds numbers, and whether or not the tunnel was running noisy or quiet for that figure.

Table A.1: Freestream conditions for plots in Chapter 4

Figure	$T_0$ (K)	$(P_0)$ (kPa)	Re ( $\times 10^{-6}/\text{m}$ )	Noisy/Quiet
4.3a	418	586	6.6	Quiet
4.3b	424	621	7.4	Noisy
4.6a	418	586	6.6	Quiet
4.6b	424	627	7.5	Noisy
4.10	427	538	5.9	Quiet
4.13 ( $x=15.0$ cm)	433	557	5.9	Quiet
4.13 ( $x=25.4$ cm)	425	521	5.7	Quiet
4.13 ( $x=30.5$ cm)	428	534	5.8	Quiet
4.15b	428	648	7.6	Noisy
4.15c	425	632	7.0	Quiet
4.15d	427	762	9.0	Noisy
4.15e	424	742	8.2	Quiet
4.15f	427	859	10.1	Noisy
4.15g	424	844	9.3	Quiet
4.15h	427	963	11.3	Noisy
4.15i	424	932	10.3	Quiet
4.17a	422	607	6.7	Quiet
4.17b	424	614	7.4	Noisy
4.21	427	538	5.8	Quiet
4.23 ( $x=10.7$ cm)	427	534	5.8	Quiet
4.23 ( $x=14.0$ cm)	427	532	5.8	Quiet
4.23 ( $x=20.3$ cm)	427	531	5.8	Quiet
4.23 ( $x=30.5$ cm)	427	532	5.8	Quiet



Table A.2: Freestream conditions for plots in Chapter 5: Part I

Figure	$T_0$ (K)	$(P_0)$ (kPa)	Re ( $\times 10^{-6}/\text{m}$ )	Noisy/Quiet
5.1a	428	275	3.2	Noisy
5.1b	428	607	7.1	Noisy
5.1c	428	667	7.8	Noisy
5.1d	428	796	9.4	Noisy
5.1e	428	995	11.7	Noisy
5.4 ( $x=16.8$ cm)	427	586	2.1	Noisy
5.4 ( $x=21.6$ cm)	427	593	2.1	Noisy
5.4 ( $x=33.0$ cm)	427	586	2.1	Noisy
5.7a, 5.8a, 5.9a, 5.10a	427	278	3.3	Noisy
5.7a, 5.8a, 5.9a, 5.10a	427	406	4.8	Noisy
5.7a, 5.8a, 5.9a, 5.10a	426	493	5.8	Noisy
5.7a, 5.8a, 5.9a, 5.10a	426	529	6.2	Noisy
5.7a, 5.8a, 5.9a, 5.10a	426	599	7.1	Noisy
5.7a, 5.8a, 5.9a, 5.10a	426	656	7.7	Noisy
5.7a, 5.8a, 5.9a, 5.10a	426	727	8.6	Noisy
5.7a, 5.8a, 5.9a, 5.10a	426	790	9.3	Noisy
5.7a, 5.8a, 5.9a, 5.10a	426	854	10.1	Noisy
5.7a, 5.8a, 5.9a, 5.10a	426	916	10.8	Noisy
5.7a, 5.8a, 5.9a, 5.10a	426	978	11.6	Noisy

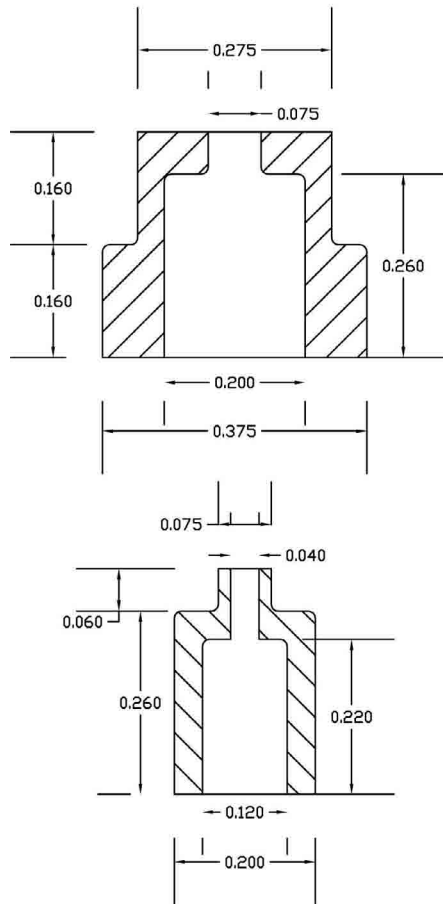
Table A.3: Freestream conditions for plots in Chapter 5: Part II

Figure	$T_0$ (K)	$(P_0)$ (kPa)	Re ( $\times 10^{-6}/\text{m}$ )	Noisy/Quiet
5.13a	422	942	10.5	Quiet
5.13b	426	972	11.5	Noisy
5.21 (No glow)	429	618	7.2	Noisy
5.21 (Glow)	429	613	7.2	Noisy
5.28a	428	607	7.1	Noisy
5.28b	428	600	7.0	Noisy
5.28c	428	599	7.0	Noisy
5.29a	425	588	6.5	Quiet
5.29b	428	607	7.1	Noisy
5.29c	425	588	6.5	Quiet
5.29d	428	599	7.0	Noisy
5.29e	425	589	6.5	Quiet
5.29f	428	598	7.0	Noisy
5.30a	425	598	6.6	Quiet
5.30b	428	618	7.2	Noisy
5.30c	425	600	6.6	Quiet
5.30d	428	611	7.2	Noisy
5.30e	425	602	6.6	Quiet
5.30f	428	616	7.2	Noisy

## **B. DRAWINGS**

Included here are the drawings submitted to the shop for fabrication of the glow perturber and also the modifications of the aluminum model.

Matt Borg  
 Mar. 2008  
 Glow Perturber



Notes:

- 1) First machine brass. Slip fit it in the model insert. Secure with high-temp epoxy. Make upper surface conformal with model insert upper surface. Remove all burrs.
- 2) Let me solder high-voltage wire into copper piece
- 3) Slip fit copper piece into Macor and secure with high-temp epoxy
- 4) Slip fit Macor piece into brass and secure with high-temp epoxy
- 5) Hand work the upper surface so that it is conformal with the model insert's upper surface
- 6) Make chamfered corners as tight-fitting as possible.

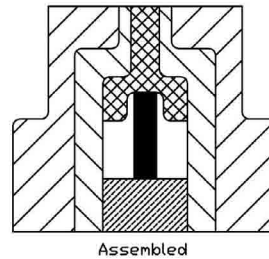
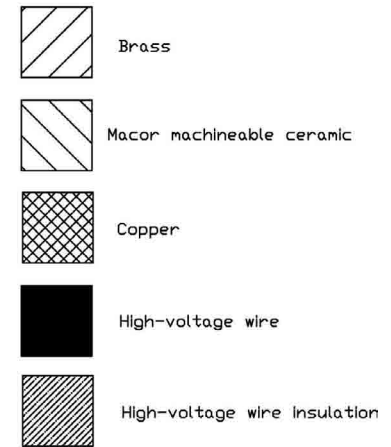
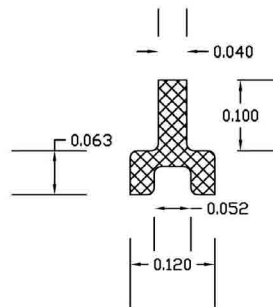


Figure B.1: Glow perturber design drawing

Matt Borg  
 12 January, 2009  
 Modifications to X-51A Aluminum Afterbody

- 1) Drill 0.3 diam. hole from back of model forward approx. parallel to upper surface (about 8.3 deg.)
- 2) Align 0.25 hole with centerline of sting support hole

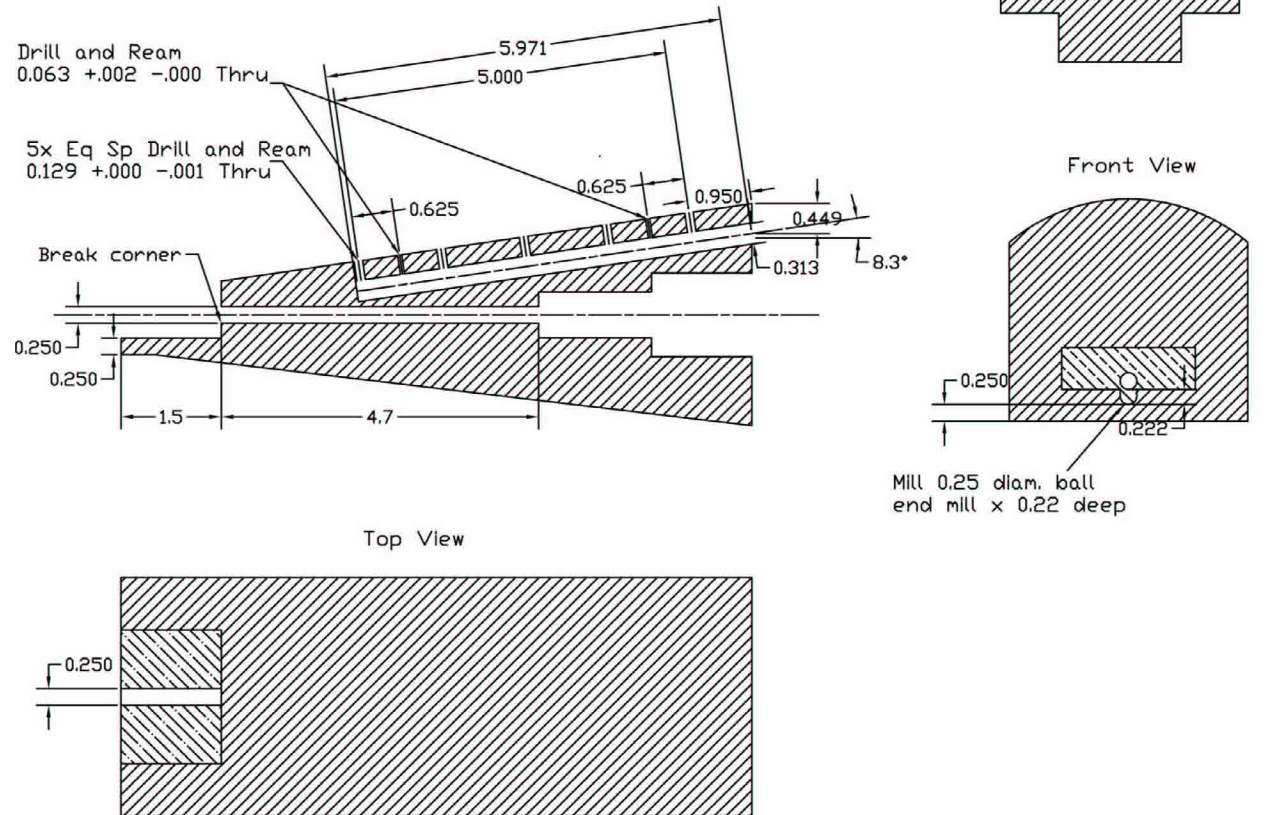


Figure B.2: Modifications to aluminum afterbody to allow installation of PCB sensors and glow perturber

VITA

## VITA

Matthew P. Borg was born in Fairmont, MN. He graduated from Fairmont Senior High School in 1999. He then attended Bethel University, graduating with a B.S. in physics and a minor in mathematics in 2003. The summer of 2002 was spent engaged in research at the Princeton Plasma Physics Laboratory as part of the National Science Foundation's Summer Undergraduate Fellowship program. Matt received his M.S. in Aeronautics and Astronautics from Purdue University in 2005 and his Ph.D. in 2009. He accepted a position with Booz Allen Hamilton as a contractor to the AFRL's Air Vehicle Directorate.